

Biocompatible Metal-Organic Frameworks for the Storage and Therapeutic Delivery of Hydrogen Sulfide

Faith E. Chen,^{a,‡} Ruth M. Mandel,^{a,‡} Joshua J. Woods,^a Jung-Hoon Lee,^b Jaehwan Kim,^a Jesse H. Hsu,^a José J. Fuentes-Rivera,^a Justin J. Wilson,^a Phillip J. Milner^{a,*}

^aDepartment of Chemistry and Chemical Biology, Cornell University, Ithaca, NY, 14850, United States

^bComputational Science Research Center, Korea Institute of Science and Technology (KIST), Seoul 02792, Republic of Korea

*pjm347@cornell.edu

‡These authors contributed equally.

Supporting Information

Table of Contents.	Page.
1. General procedures.	2
2. Small-scale preparations of MOFs under aqueous conditions with formic acid as modulator.	5
3. Preparation and characterization of $Zr_6O_4(OH)_4(\text{fumarate})_6$, Zr-fum-DMF.	8
4. Preparation and characterization of aqueous $Zr_6O_4(OH)_4(\text{fumarate})_6$, Zr-fum- H_2O .	12
5. Preparation and characterization of $Zr_6O_4(OH)_4(\text{mesaconate})_6$, Zr-mes-DMF.	16
6. Preparation and characterization of aqueous $Zr_6O_4(OH)_4(\text{mesaconate})_6$, Zr-mes- H_2O .	20
7. Preparation and characterization of $Zr_6O_4(OH)_4(\text{itaconate})_6$, Zr-ita-DMF.	24
8. Preparation and characterization of aqueous $Zr_6O_4(OH)_4(\text{itaconate})_6$, Zr-ita- H_2O .	27
9. Water adsorption isotherms of MOFs prepared under aqueous conditions.	33
10. H_2S adsorption isotherms of MOFs prepared under aqueous conditions.	37
11. Characterization of MOFs prepared under aqueous conditions exposed to H_2S solution.	46
12. H_2S cycling of MOFs prepared under aqueous conditions.	53
13. Delivery of H_2S under biologically relevant conditions.	59
14. Computational and structural details.	69
15. H_2S and aqueous stability studies with Zn-MOF-74.	74
16. DRIFTS measurements.	85
17. References.	87

1. General procedures.

All reagents were purchased from commercial vendors and used without additional purification. The metal salts zirconyl chloride octahydrate (98%, Alfa Aesar) and zirconium (IV) chloride (99.5%, Alfa Aesar) were kept in desiccators when not in use. Fumaric acid (99%), mesaconic acid (99%), 2,5-dihydroxyterephthalic acid (H₄dobdc, 95%), reagent-grade *N,N*-dimethylformamide (DMF), lead (II) chloride (anhydrous, 99.99%), potassium bromide (99%), sodium azide (99%), zinc nitrate hexahydrate (98%), and sodium sulfide nonahydrate (98%) were purchased from Sigma-Aldrich. Itaconic acid (99%, Alfa Aesar) was provided by the group of Prof. Brett Fors (Cornell University), for which we are grateful. Reagent-grade acetic acid was purchased from EMD Chemicals. Reagent-grade formic acid was purchased from Mallinckrodt Chemical. Absolute ethanol, acetonitrile, hexanes, methanol, dichloromethane (DCM), tetrahydrofuran (THF, 99%), tripotassium phosphate (99%), pH 3 buffer (potassium hydrogen phthalate), pH 7 buffer (monopotassium phosphate, sodium hydroxide, water), and pH 10 buffer (potassium hydroxide, potassium carbonate, potassium borate, water) solutions were purchased from Fisher Scientific or VWR. 5-(dimethylamino)naphthalene-1-sulfonyl chloride (dansyl chloride, 98%) was purchased from Cayman Chemical. Phosphate buffered saline (PBS) and fetal bovine serum (FBS) were purchased from Corning Life Sciences (Tewksbury, MA). A cylinder of hydrogen sulfide (H₂S, 99.5%) was purchased from Airgas. A solution of H₂S in THF (0.8 M) was purchased from Fluka Chemical. Deuterated dimethyl sulfoxide (DMSO-d₆, 99%) and deuterium oxide (D₂O, 99.9%) were purchased from Cambridge Isotope Laboratories.

Infrared spectra were collected on a Bruker Tensor II IR spectrometer with a diamond Attenuated Total Reflectance (ATR) attachment. Diffuse reflectance infrared Fourier transform spectroscopy (DRIFTS) spectra were collected on a Bruker Tensor II IR spectrometer with a Harrick Praying Mantis attachment in a low temperature reaction chamber. Fluorescence spectra were measured using a Cary Eclipse fluorescence spectrophotometer (Agilent, Santa Clara, CA). Surface area data were collected on a Micromeritics 3-flex gas sorption analyzer using ultrapure N₂ (99.999%) and a liquid N₂ bath. Brunauer-Emmett-Teller (BET) and Langmuir surface areas were determined by linear least squares regression analysis using the linearized forms of the BET and Langmuir equations, respectively. Water and H₂S adsorption isotherms were collected on a Micromeritics 3-flex gas sorption analyzer. MOFs were activated at 100 °C or 180 °C in the case of Zn-MOF-74 for 48 h prior to any gas sorption measurements. Powder X-ray diffraction (PXRD)

patterns were collected on a Rigaku Ultima IV diffractometer equipped with a CuK α source ($\lambda = 1.54 \text{ \AA}$) and were baseline corrected after data collection. $^1\text{H-NMR}$ data were collected on a Bruker INOVA 500 MHz spectrometer and are referenced to residual solvent. The use of this instrument is supported by the National Science Foundation (CHE-1531632). Decomposition profiles were collected on a Q500 V6.7 thermogravimetric analyzer using a temperature ramp of 5.00 $^\circ\text{C}/\text{min}$ from room temperature to 800.00 $^\circ\text{C}$. Scanning electron microscopy images were taken at 1.0 kV using a Zeiss Gemini 500 scanning electron microscope. The powder samples were immobilized on carbon tape mounted on an aluminum stub. The samples were blown using compressed air to remove excess material not stuck to the tape and then were coated with a carbon layer. X-ray photoelectron spectroscopy (XPS) spectra were collected using a Scienta Omicron ESCA-2SR with an operating pressure of 1×10^{-9} Torr. Monochromatic Al K α x-rays (1486.6 eV) were generated at 300 W (15 kV; 20 mA) with photoelectrons collected from a 2 mm diameter analysis spot. Photoelectrons were collected at a 0° emission angle with a source to analyzer angle of 54.7° . A hemispherical analyzer determined the electron kinetic energy, using a pass energy of 200 eV for wide/survey scans, and 50 eV for high resolution scans. A flood gun was used for charge neutralization on all samples. Survey scans, C1s, O1s, and S2p high resolution scans were collected for all samples. Zn2p and Zr3d high resolution scans were collected for Zn-MOF-74 and Zr-fum samples, respectively. Spectra were analyzed in CasaXPS; each scan was binding energy calibrated to the C1s primary peak position set to 284.8 eV.

H_2S adsorption data were fit using the Dual-Site Langmuir-Freundlich model (eq. S1), where $Q(P)$ is the predicted uptake Q at pressure P in mmol/g, $Q_{\text{sat}i}$ is the saturation pressure of binding site i in mmol/g, b_i is the Langmuir parameter of site i , v_i is the Freundlich parameter of site i , $-S_i$ is the entropy of binding site i in J/mol \cdot K, R is the ideal gas constant, E_i is the enthalpy of adsorption for binding site i in kJ/mol, and T is the temperature in K. The isotherms were fit with either v_1 and v_2 set as 1 (Dual-Site Langmuir model) or with v_1 and v_2 allowed to vary freely (Langmuir-Freundlich model). Fits were obtained using Solver in Microsoft Excel.

$$Q(P) = \frac{Q_{\text{sat}1}(b_1P)^{v_1}}{1+(b_1P)^{v_1}} + \frac{Q_{\text{sat}2}(b_2P)^{v_2}}{1+(b_2P)^{v_2}}; b_i = e^{\left(\frac{-S_i}{R}\right)\left(\frac{1000 \cdot E_i}{RT}\right)} \quad \text{eq. S1}$$

Heats of adsorption were calculated using the Clausius-Clapeyron equation (eq. S2), where P_Q are pressure values corresponding to the same loading Q , ΔH_{ads} is the differential enthalpy of adsorption in kJ/mol, R is the ideal gas constant, T is the temperature in K, and c is a constant. Fits over a range of Q values were obtained using Mathematica.

$$\ln(P_Q) = \left(\frac{\Delta H_{ads}}{R} \right) \left(\frac{1}{T} \right) + c$$

eq. S2

2. Small-scale preparations of MOFs under aqueous conditions with formic acid as modulator.

Zr-fum-H₂O. Fumaric acid (58.0 mg, 0.50 mmol, 1.00 eq) and ZrOCl₂·8H₂O (161 mg, 0.50 mmol, 1.00 eq) were added to a 15 mL screw cap reaction tube along with deionized water (2 mL). Next, either 0 eq, 10 eq (189 μ L, 5.00 mmol), 30 eq (566 μ L, 15.0 mmol), 50 eq (943 μ L, 25.0 mmol) or 80 eq (1.51 mL, 40.0 mmol) of formic acid were added. The tube was heated to 95 °C in an aluminum heating block without stirring for 24 h. After removing the tube from the heating block and allowing it to cool to room temperature, the remaining solvent was pipetted off of the settled precipitate and replaced with fresh ethanol (10 mL). The ethanol was replaced once every 24 h for three days. Powder X-ray diffraction patterns were collected after the last ethanol soak.

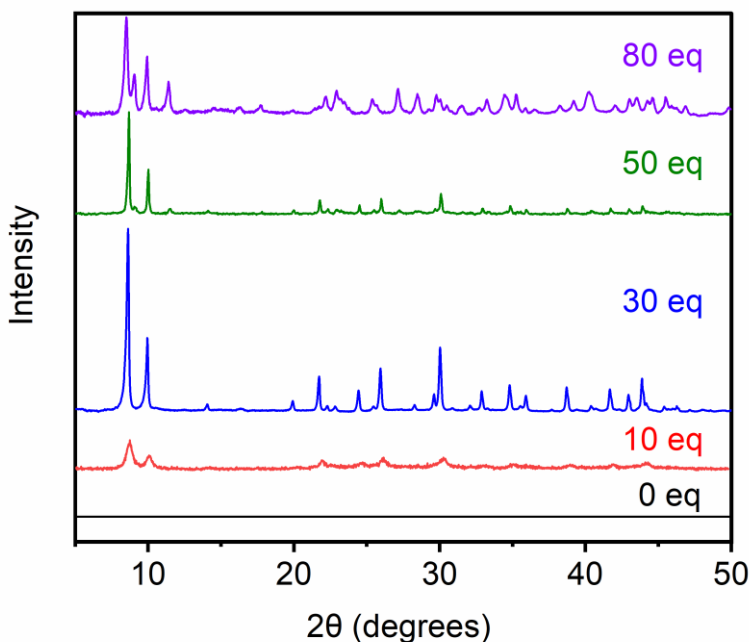


Figure S1. Powder X-ray diffraction patterns ($\lambda = 1.54 \text{ \AA}$) of ethanol-solvated Zr-fum-H₂O prepared with either 0, 10, 30, 50, or 80 equivalents of formic acid. Zr-fum-H₂O prepared with 30 equivalents was determined to be the most crystalline and phase pure. Therefore, this ratio was used in subsequent large-scale preparations.

Zr-mes-H₂O. Mesaconic acid (65.0 mg, 0.50 mmol, 1.00 eq) and ZrOCl₂·8H₂O (161 mg, 0.50 mmol, 1.00 eq) were added to a 15 mL screw cap reaction tube along with deionized water (2 mL). Next, either 0 eq, 30 eq (566 μL, 15.0 mmol), 50 eq (943 μL, 25.0 mmol) or 80 eq (1.51 mL, 40.0 mmol) of formic acid were added. The tube was heated to 95 °C in an aluminum heating block without stirring for 24 h. After removing the tube from the heating block, the remaining solvent was pipetted off of the settled precipitate and replaced with fresh ethanol (10 mL). The ethanol was replaced once every 24 h for three days. Powder X-ray diffraction patterns were collected after the last soak.

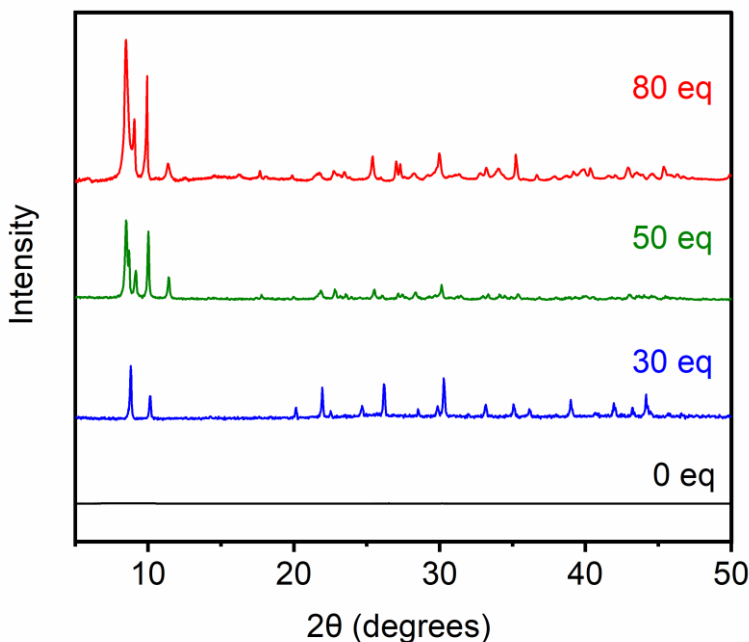


Figure S2. Powder X-ray diffraction patterns ($\lambda = 1.54 \text{ \AA}$) of ethanol-solvated Zr-mes-H₂O prepared with either 0, 30, 50, or 80 equivalents of formic acid. Zr-mes-H₂O prepared with 30 equivalents was determined to be the most crystalline and phase pure. Therefore, this ratio was used in subsequent large-scale preparations.

Zr-ita-H₂O. Itaconic acid (65.0 mg, 0.50 mmol, 1.00 eq) and ZrOCl₂·8H₂O (161 mg, 0.50 mmol, 1.00 eq) were added to a 15 mL screw cap reaction tube along with deionized water (2 mL). Next, either 0 eq, 1 eq (18.9 μL, 0.50 mmol), 3 eq (56.6 μL, 1.50 mmol), 5 eq (94.3 μL, 2.50 mmol), 7 eq (0.13 mL, 3.50 mmol), or 9 eq (0.17 mL, 4.50 mmol) of formic acid were added. 0 eq, 1 eq (28.6 μL, 0.50 mmol), 3 eq (85.9 μL, 1.50 mmol), 5 eq (0.14 mL, 2.50 mmol), 7 eq (0.20 mL, 3.50 mmol), and 9 eq (0.26 mL, 4.50 mmol) of acetic acid were also tried under the same reaction conditions. The tube was heated to 95 °C in an aluminum heating block without stirring for 24 h. After removing the tube from the heating block, the remaining solvent was pipetted off of the settled precipitate and replaced with fresh ethanol (10 mL). The ethanol was replaced once every 24 h for three days. Powder X-ray diffraction patterns were collected after the last soak. In both cases only 1 eq and 3 eq of acid modulator produced any solid after heating.

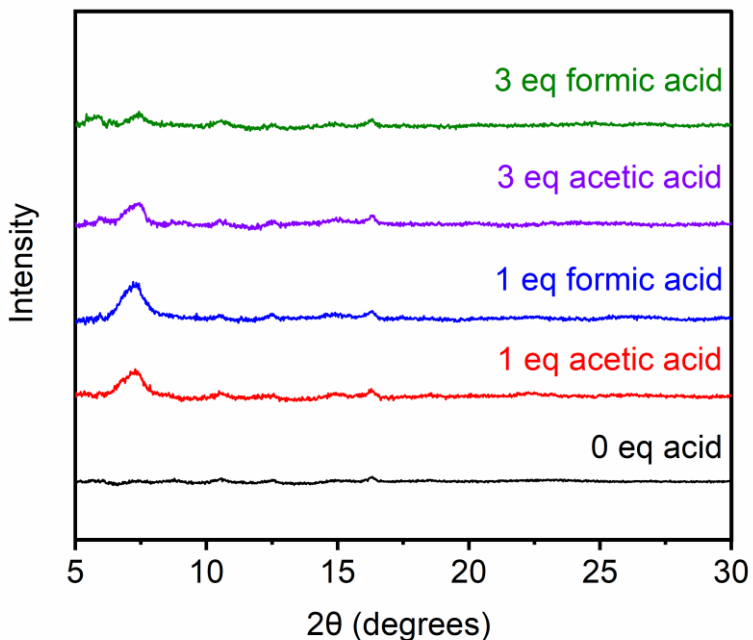


Figure S3. Powder X-ray diffraction patterns ($\lambda = 1.54 \text{ \AA}$) of ethanol-solvated Zr-ita-H₂O prepared with either 0, 1, or 3 equivalents of formic acid or acetic acid. Zr-ita-H₂O prepared with 1 equivalent of formic acid was determined to be the most crystalline and phase pure. Therefore, this ratio and acid modulator were used in subsequent large-scale preparations.

3. Preparation and characterization of $\text{Zr}_6\text{O}_4(\text{OH})_4(\text{fumarate})_6$, Zr-fum-DMF.

This procedure was adapted from the literature.¹ Fumaric acid (1.16 g, 10.0 mmol, 1.00 eq), $\text{ZrOCl}_2 \cdot 8\text{H}_2\text{O}$ (3.24 g, 10.0 mmol, 1.00 eq), and formic acid (14.0 mL, 371 mmol, 37.0 eq) were added to a screw cap, high pressure reaction vessel equipped with a stir bar. Next, DMF (40 mL) was added, and the reaction vessel was sealed. The mixture was stirred and heated at 120 °C for 24 h. The heterogeneous reaction mixture was allowed to cool to room temperature and filtered. The resulting precipitate was transferred into a screw cap jar filled with DMF (80 mL), and the mixture was allowed to stand for 24 h at room temperature. The DMF was then decanted and replaced with the same volume of fresh DMF. This procedure was repeated an additional two times for a total of three DMF soaks, at which point the DMF was replaced with ethanol (80 mL), and the process repeated another three times for a total of six washes. The solid was then activated under high vacuum (<100 mbar) at 100 °C overnight to yield $\text{Zr}_6\text{O}_4(\text{OH})_4(\text{fumarate})_6$ as a white solid.

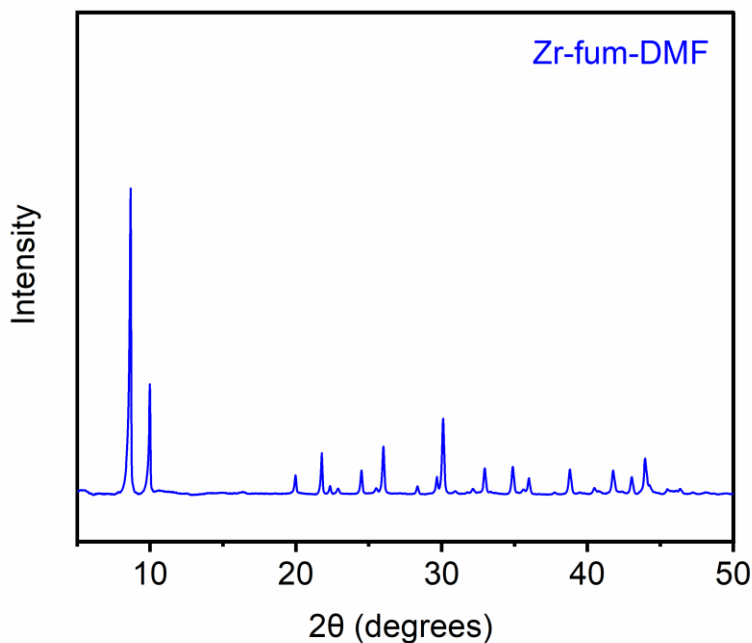


Figure S4. Powder X-ray diffraction pattern ($\lambda = 1.54 \text{ \AA}$) of ethanol-solvated Zr-fum-DMF.

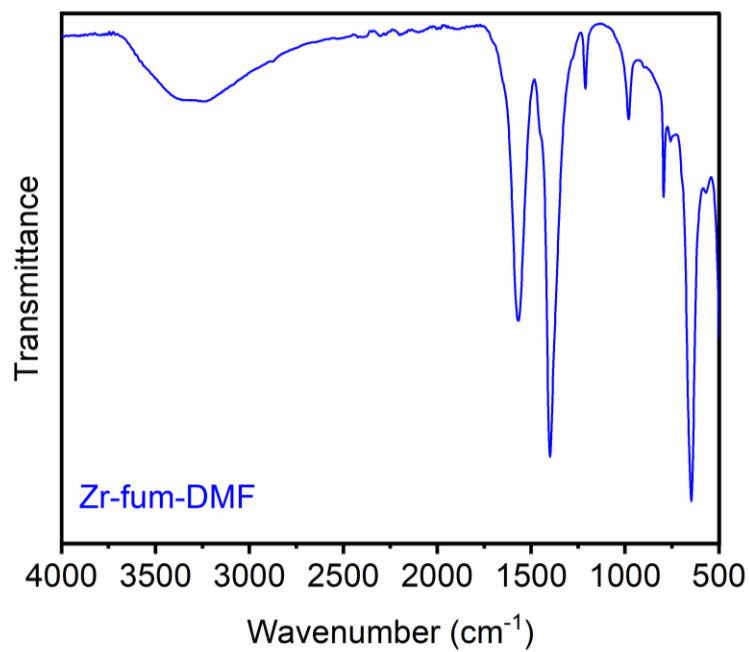


Figure S5. Infrared spectrum of ethanol-solvated Zr-fum-DMF. The absence of a stretch at 1650 cm^{-1} confirms that the ethanol soaking procedure is sufficient to remove DMF from the pores.

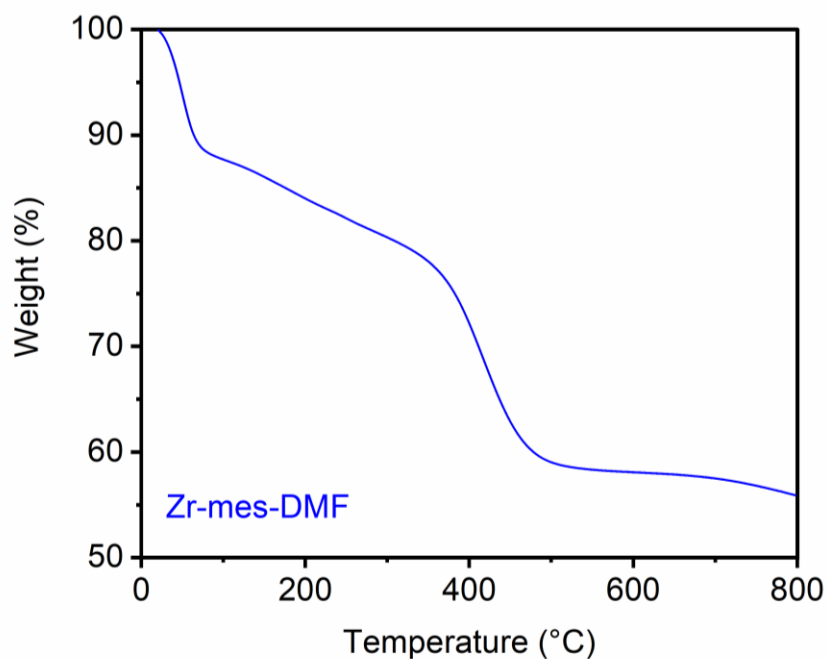


Figure S6. Decomposition profile (ramp rate = $5\text{ }^{\circ}\text{C}/\text{min}$) of ethanol-solvated Zr-fum-DMF.

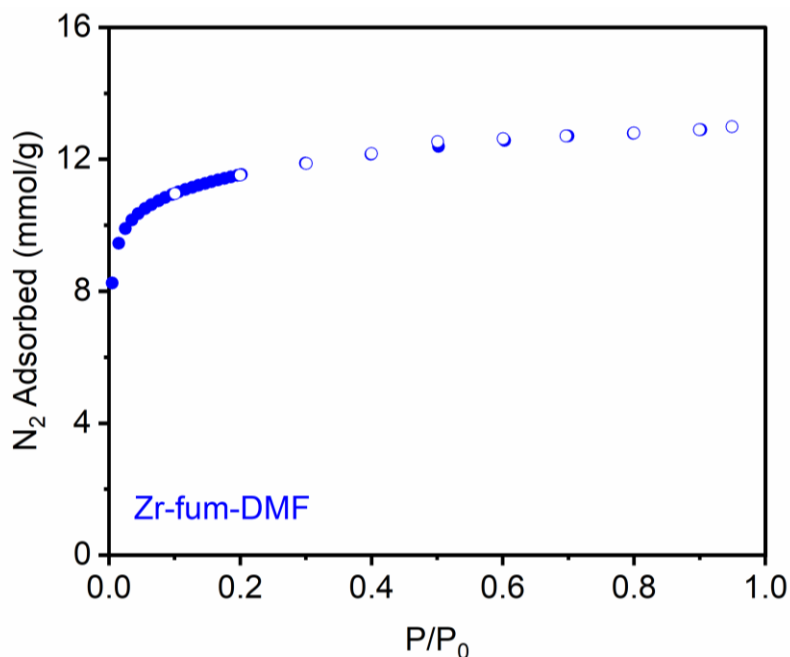


Figure S7. 77 K N_2 adsorption isotherm of activated Zr-fum-DMF. Desorption data are represented as open circles. Fitting the data yielded a Brunauer-Emmett-Teller (BET) surface area of $988 \pm 1 \text{ m}^2/\text{g}$ (previously reported BET surface area of $990 \text{ m}^2/\text{g}$)¹ and a Langmuir surface area of $1322 \pm 2 \text{ m}^2/\text{g}$ (previously reported Langmuir surface area of $1070 \text{ m}^2/\text{g}$)¹.

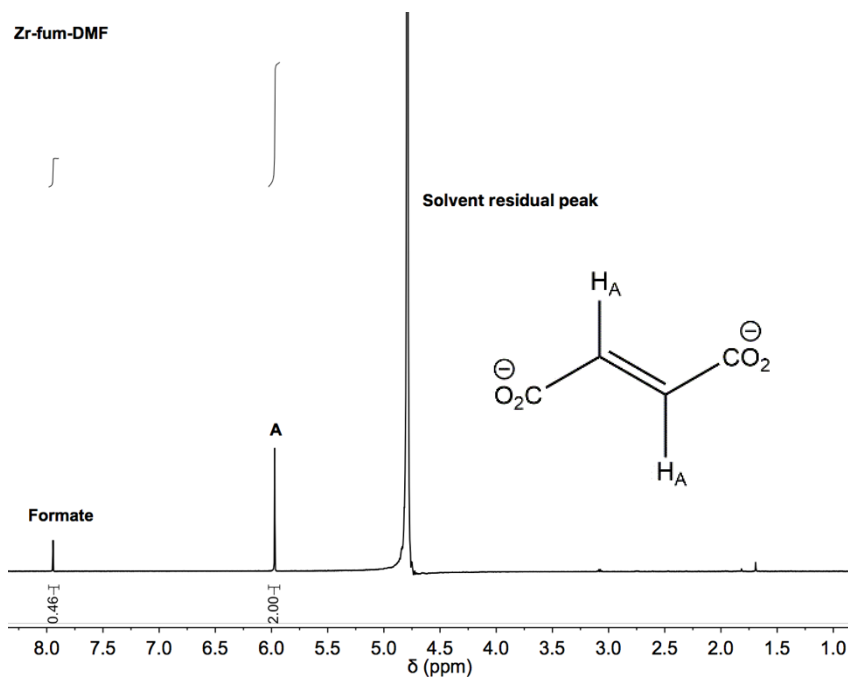


Figure S8. $^1\text{H-NMR}$ (500 MHz, D_2O) spectrum of ethanol-solvated Zr-fum-DMF digested with a saturated solution of K_3PO_4 in D_2O . Peak A corresponds to the fumarate linker. The peak corresponding to formate likely arises due to missing linker defects, in which one molecule of fumarate is replaced by two molecules of formate.

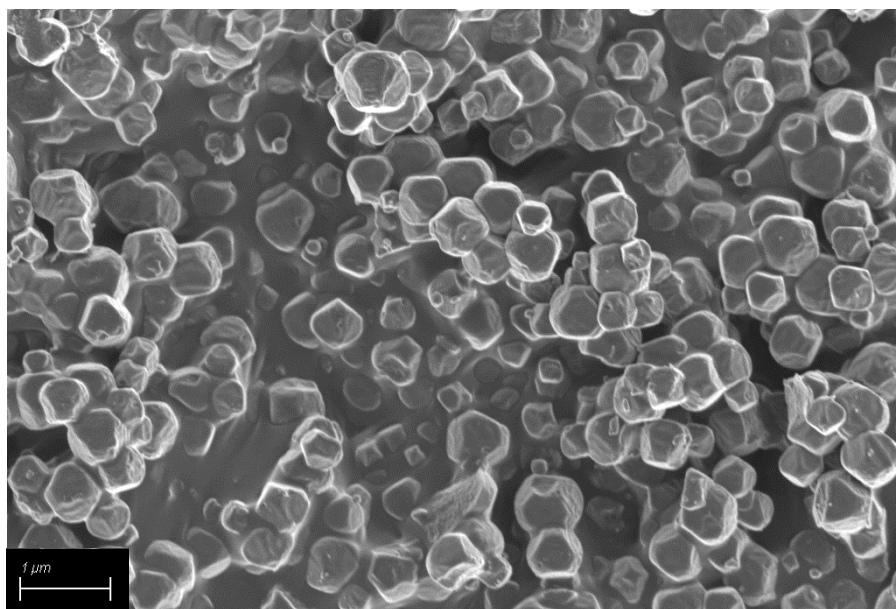


Figure S9. Scanning electron microscopy image (width = 10 μm) of Zr-fum-DMF.

4. Preparation and characterization of aqueous $\text{Zr}_6\text{O}_4(\text{OH})_4(\text{fumarate})_6$, $\text{Zr-fum-H}_2\text{O}$.

Fumaric acid (1.16 g, 10.0 mmol, 1.00 eq), $\text{ZrOCl}_2 \cdot 8\text{H}_2\text{O}$ (3.24 g, 10.0 mmol, 1.00 eq), and formic acid (11.3 mL, 300 mmol, 30.0 eq) were added to a screw cap, high pressure reaction vessel equipped with a stir bar. Next, deionized water (40 mL) was added, and the reaction vessel was sealed. The mixture was stirred and heated at 95 °C for 24 h. The heterogeneous reaction mixture was allowed to cool to room temperature. After cooling, the mixture was transferred into a centrifuge tube and centrifuged at 4000 rpm for 10 minutes two times. The solvent was decanted, and the resulting precipitate was transferred into a screw cap jar filled with ethanol (80 mL). The solid was allowed to stand for 24 h at room temperature. The mixture was centrifuged as detailed above. The ethanol was then decanted and replaced with the same volume of fresh ethanol. This procedure was repeated a total of three times. The solid was then activated under high vacuum (<100 mbar) at 100 °C overnight to yield $\text{Zr}_6\text{O}_4(\text{OH})_4(\text{fumarate})_6$ as a white solid.

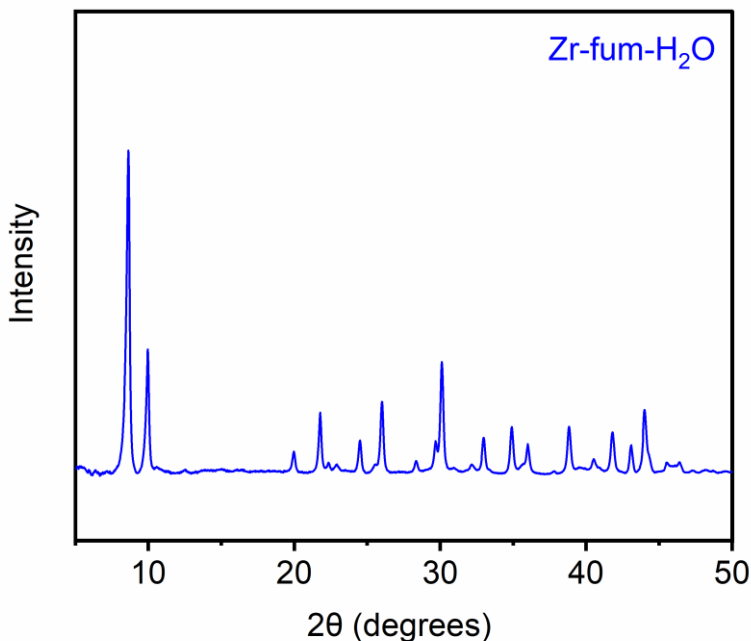


Figure S10. Powder X-ray diffraction pattern ($\lambda = 1.54 \text{ \AA}$) of ethanol-solvated $\text{Zr-fum-H}_2\text{O}$.

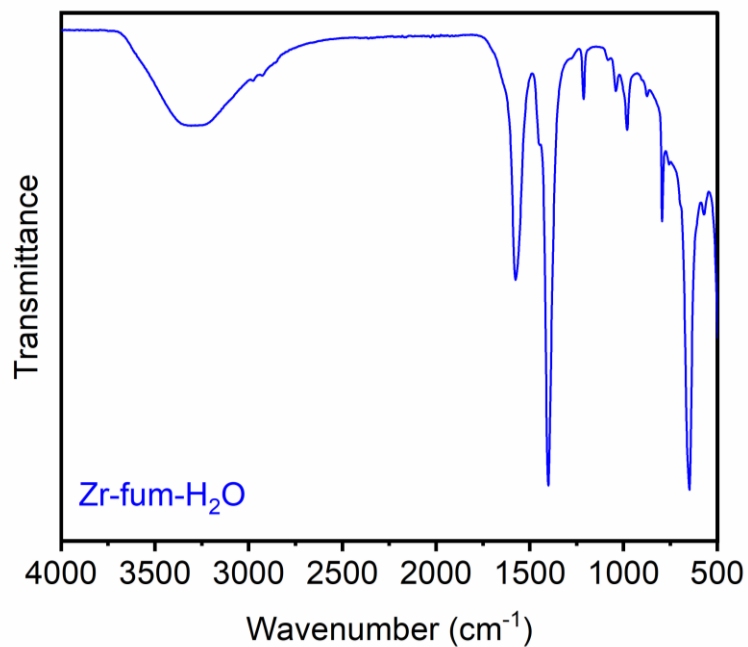


Figure S11. Infrared spectrum of ethanol-solvated Zr-fum-H₂O.

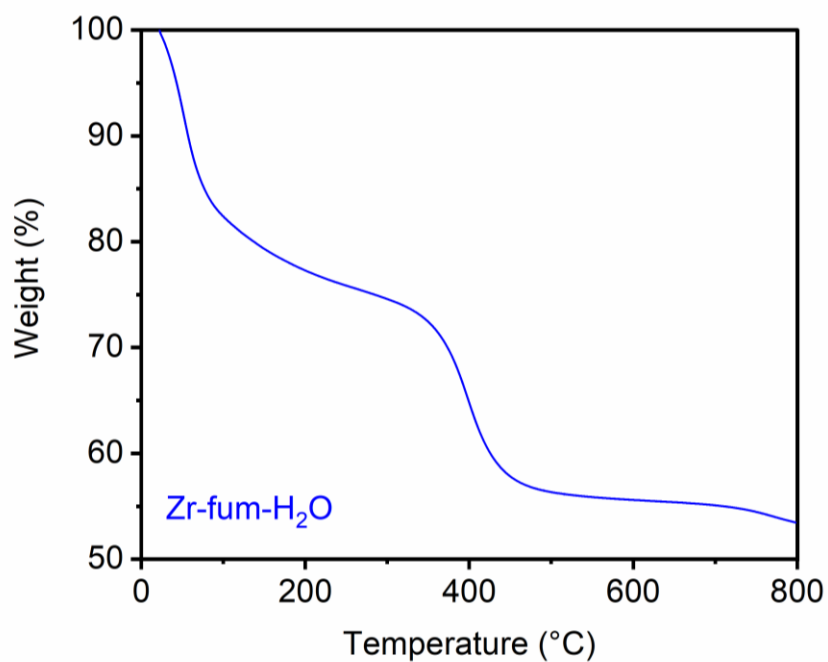


Figure S12. Decomposition profile (ramp rate = 5 °C/min) of ethanol-solvated Zr-fum-H₂O.

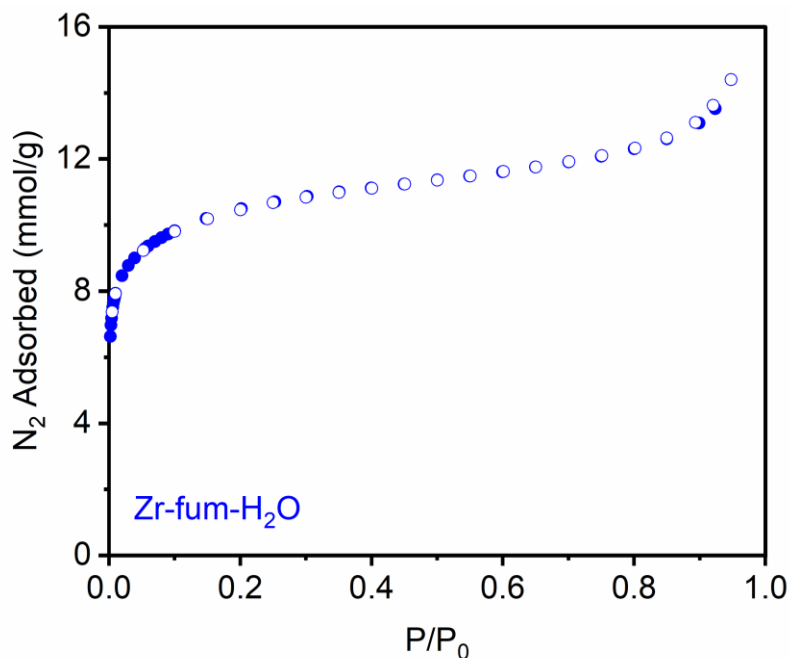


Figure S13. 77 K N_2 adsorption isotherm of activated Zr-fum- H_2O . Desorption data are represented as open circles. Fitting the data yielded a Brunauer-Emmett-Teller (BET) surface area of $873 \pm 2 \text{ m}^2/\text{g}$ (previously reported BET surface area of $990 \text{ m}^2/\text{g}$)¹ and a Langmuir surface area of $1196 \pm 9 \text{ m}^2/\text{g}$ (previously reported Langmuir surface area of $1070 \text{ m}^2/\text{g}$)¹.

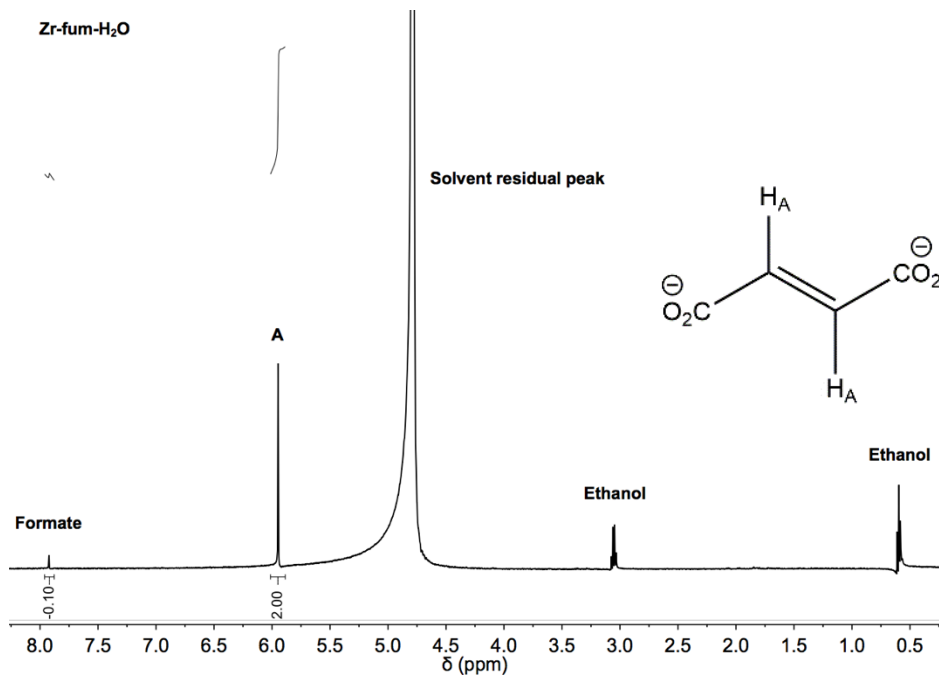


Figure S14. $^1\text{H-NMR}$ (500 MHz, D_2O) spectrum of ethanol-solvated Zr-fum- H_2O digested with a saturated solution of K_3PO_4 in D_2O . Peak **A** corresponds to the fumarate linker.

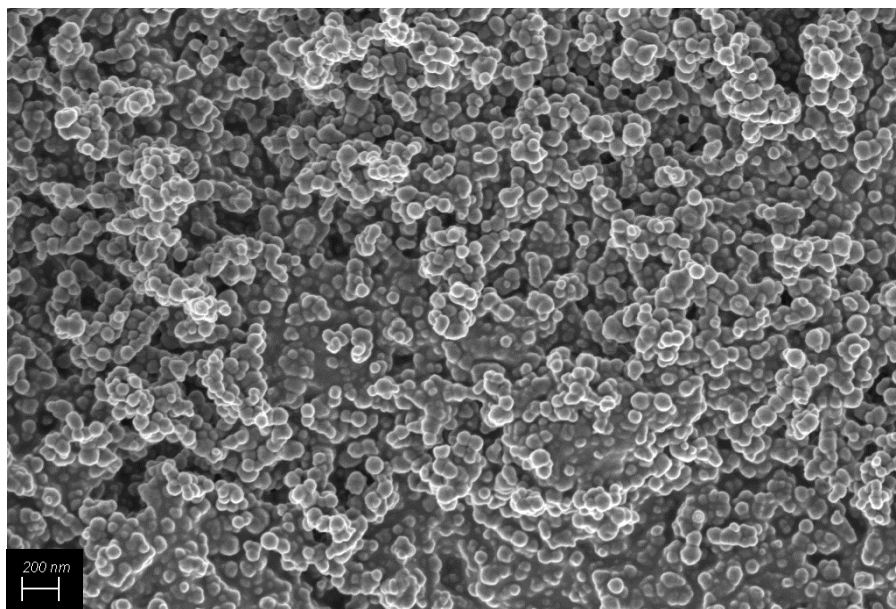


Figure S15. Scanning electron microscopy image (width = 5 μm) of Zr-fum- H_2O , confirming the nanocrystalline nature (<100 nm) of the crystallites.

5. Preparation and characterization of $\text{Zr}_6\text{O}_4(\text{OH})_4(\text{mesaconate})_6$, Zr-mes-DMF.

Mesaconic acid (1.30 g, 10.0 mmol, 1.00 eq), $\text{ZrOCl}_2 \cdot 8\text{H}_2\text{O}$ (3.24 g, 10.0 mmol, 1.00 eq), and formic acid (14.0 mL, 371 mmol, 37.0 eq) were added to a screw cap, high pressure reaction vessel equipped with a stir bar. Next, DMF (40 mL) was added, and the reaction vessel was sealed. The mixture was stirred and heated at 120 °C for 24 h. The heterogeneous reaction mixture was allowed to cool to room temperature and filtered. The resulting precipitate was transferred into a screw cap jar filled with DMF (80 mL), and the mixture was allowed to stand for 24 h at room temperature. The DMF was then decanted and replaced with the same volume of fresh DMF. This procedure was repeated an additional two times for a total of three DMF soaks, at which point the DMF was replaced with ethanol (80 mL) and the process repeated another three times for a total of six washes. The solid was then activated under high vacuum (<100 mbar) at 100 °C overnight to yield $\text{Zr}_6\text{O}_4(\text{OH})_4(\text{mesaconate})_6$ as a fine white powder.

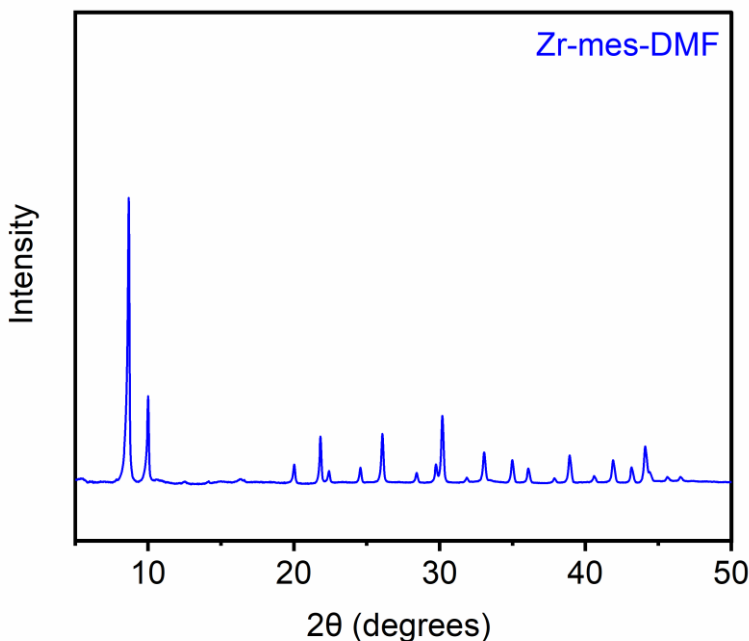


Figure S16. Powder X-ray diffraction pattern ($\lambda = 1.54 \text{ \AA}$) of ethanol-solvated Zr-mes-DMF.

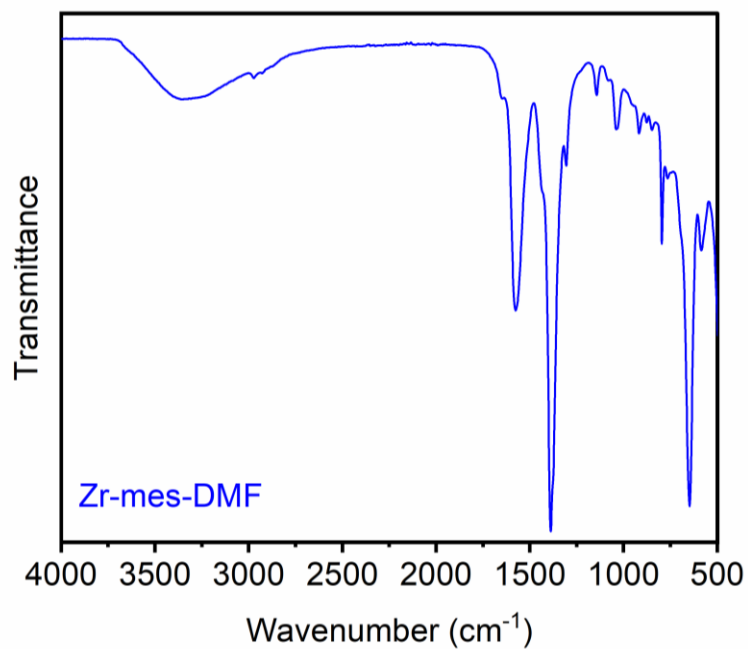


Figure S17. Infrared spectrum of ethanol-solvated Zr-mes-DMF. A residual amount of DMF is present even after soaking in ethanol, as evidenced by the small shoulder at 1650 cm^{-1} .

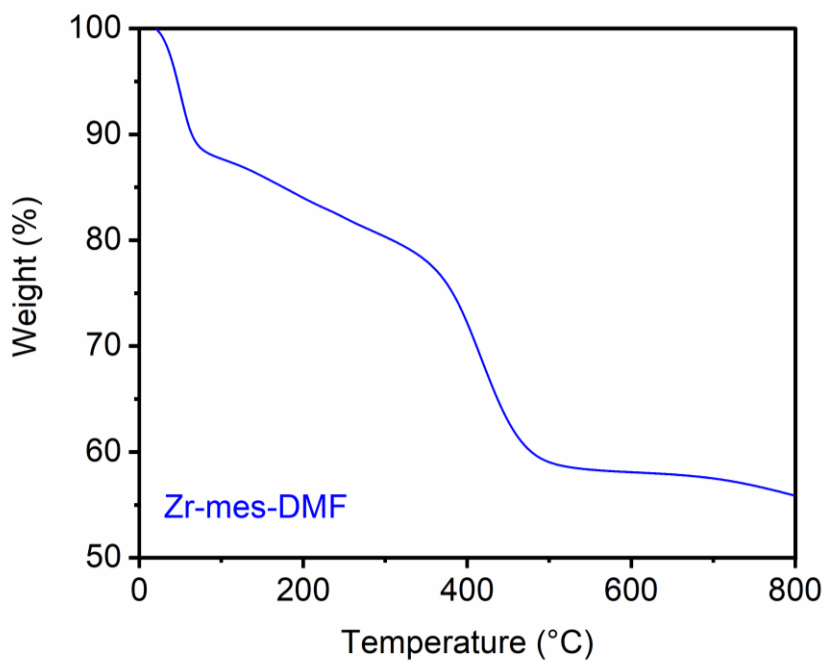


Figure S18. Decomposition profile (ramp rate = $5\text{ }^{\circ}\text{C}/\text{min}$) of ethanol-solvated Zr-mes-DMF.

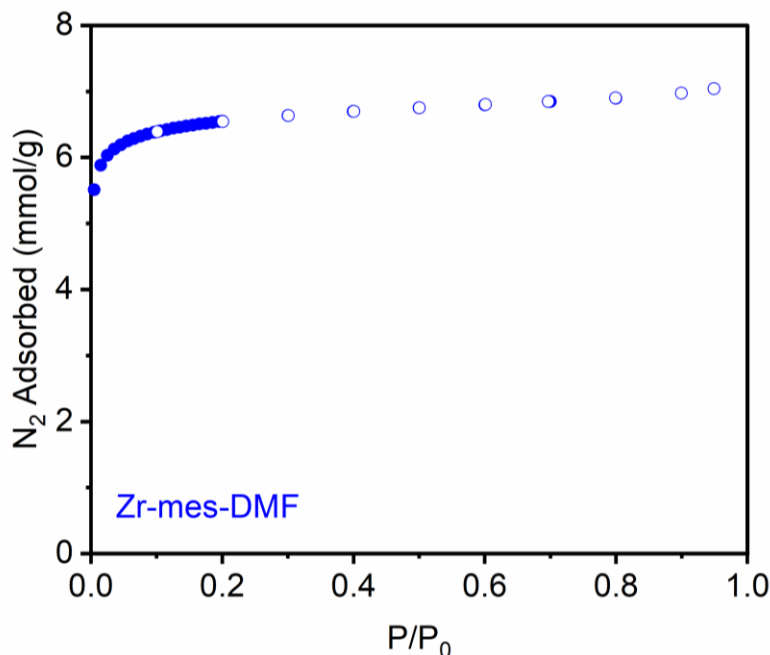


Figure S19. 77 K N₂ adsorption isotherm of activated Zr-mes-DMF. Desorption data are represented as open circles. Fitting the data yielded a Brunauer-Emmett-Teller (BET) surface area of $583 \pm 1 \text{ m}^2/\text{g}$ (previously reported BET surface area of $662 \text{ m}^2/\text{g}$)² and a Langmuir surface area of $663 \pm 2 \text{ m}^2/\text{g}$.

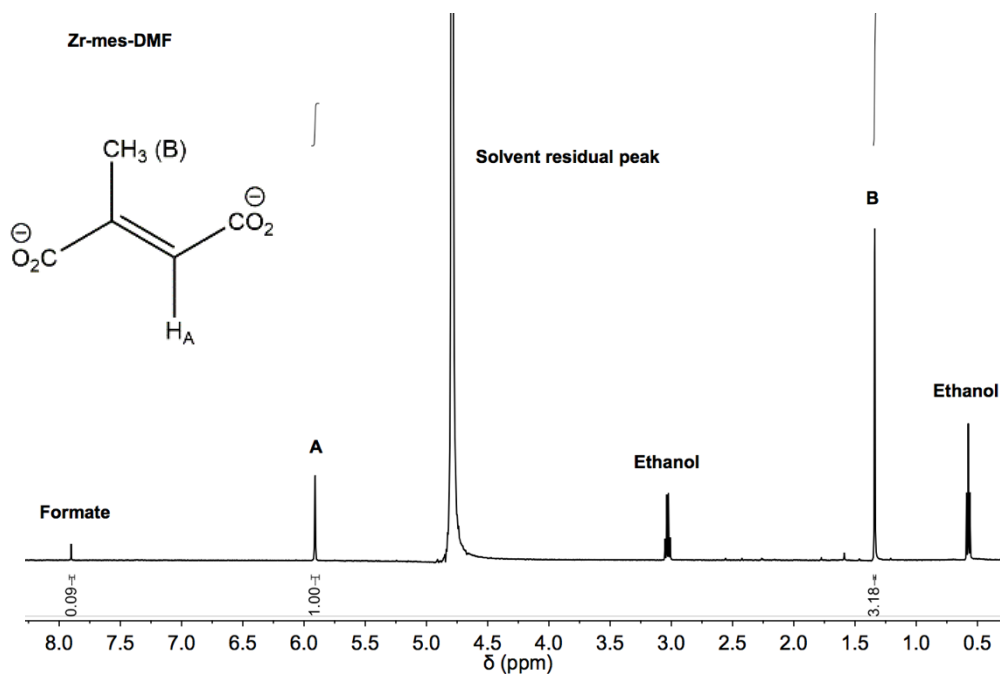


Figure S20. ¹H-NMR (500 MHz, D₂O) spectrum of ethanol-solvated Zr-mes-DMF digested with a saturated solution of K₃PO₄ in D₂O. Peaks **A** and **B** result from the mesaconate linker. The peak corresponding to formate likely arises due to missing linker defects, in which one molecule of mesaconate is replaced by two molecules of formate.

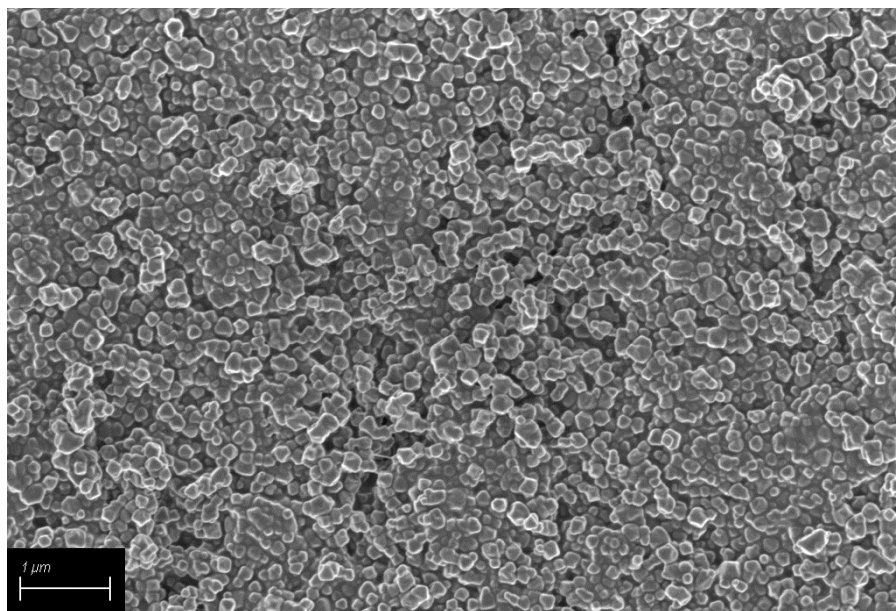


Figure S21. Scanning electron microscopy image (width = 10 μm) of Zr-mes-DMF.

6. Preparation and characterization of aqueous $\text{Zr}_6\text{O}_4(\text{OH})_4(\text{mesaconate})_6$, $\text{Zr-mes-H}_2\text{O}$.

Mesaconic acid (1.30 g, 10.0 mmol, 1.00 eq), $\text{ZrOCl}_2 \cdot 8\text{H}_2\text{O}$ (3.24 g, 10.0 mmol, 1.00 eq), and formic acid (11.3 mL, 300 mmol, 30.0 eq) were added to a screw cap, high pressure reaction vessel equipped with a stir bar. Next, deionized water (40 mL) was added, and the reaction vessel was sealed. The mixture was stirred and heated at 95 °C for 24 h. The heterogeneous reaction mixture was allowed to cool to room temperature and filtered. The precipitate was transferred into a screw cap jar filled with ethanol (80 mL), and the mixture was allowed to stand for 24 h at room temperature. The ethanol was then decanted and replaced with the same volume of fresh ethanol. This procedure was repeated a total of three times. The solid was then activated under high vacuum (<100 mbar) at 100 °C overnight to yield $\text{Zr}_6\text{O}_4(\text{OH})_4(\text{mesaconate})_6$ as a fine white powder.

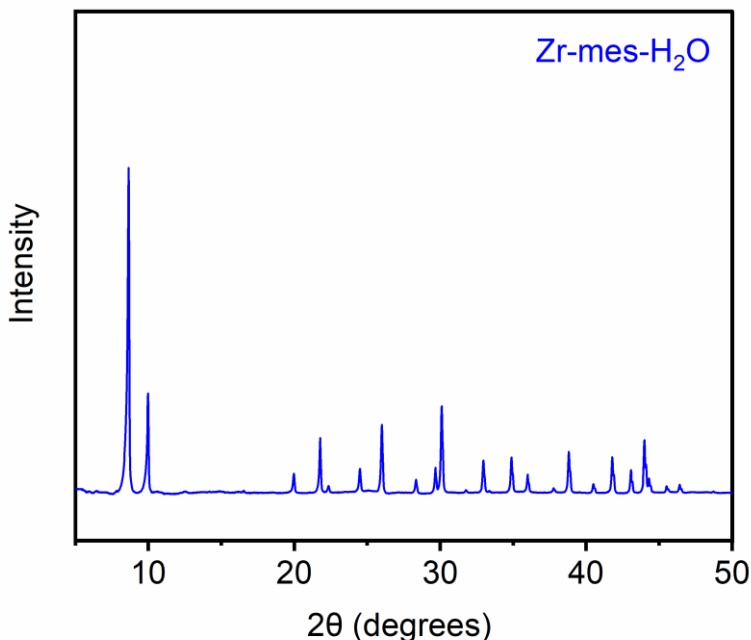


Figure S22. Powder X-ray diffraction pattern ($\lambda = 1.54 \text{ \AA}$) of ethanol-solvated $\text{Zr-mes-H}_2\text{O}$.

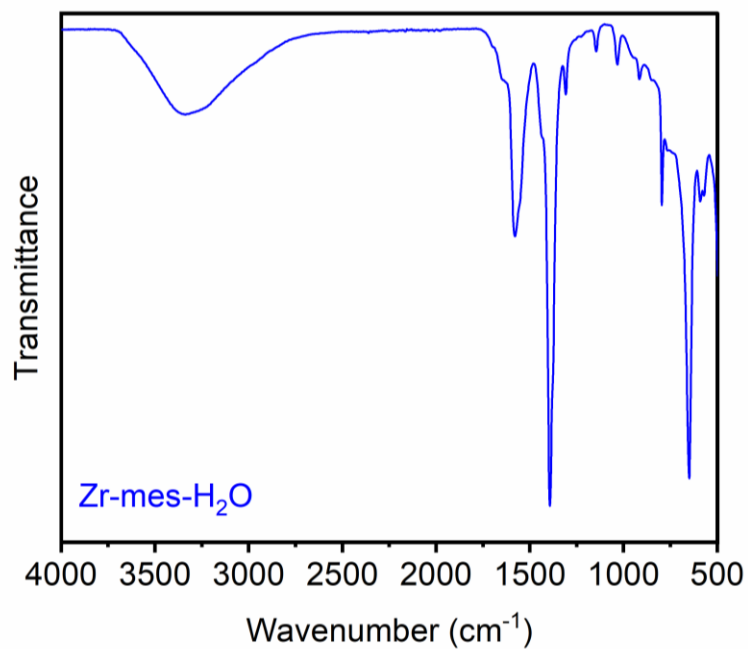


Figure S23. Infrared spectrum of ethanol-solvated Zr-mes-H₂O.

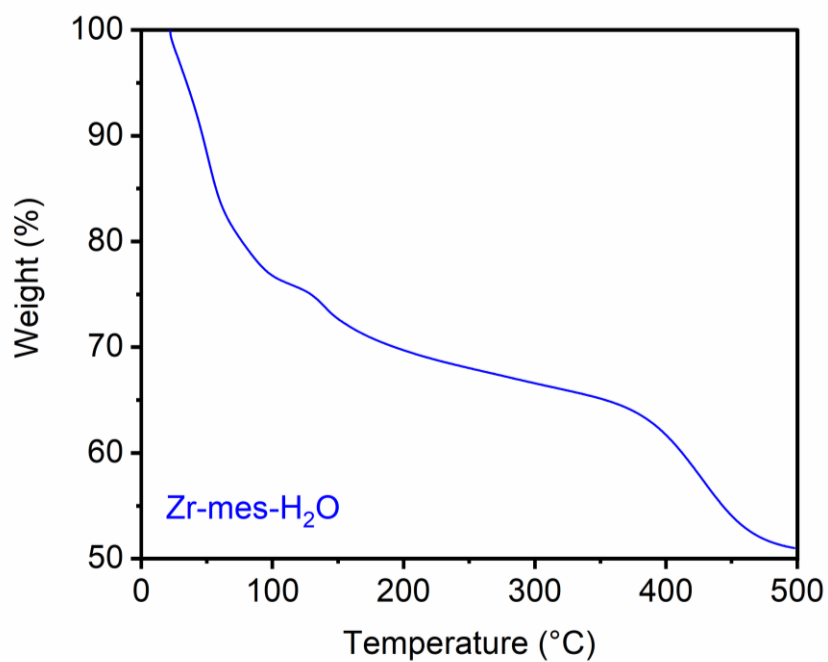


Figure S24. Decomposition profile (ramp rate = 5°C/min) of ethanol-solvated Zr-mes-H₂O.

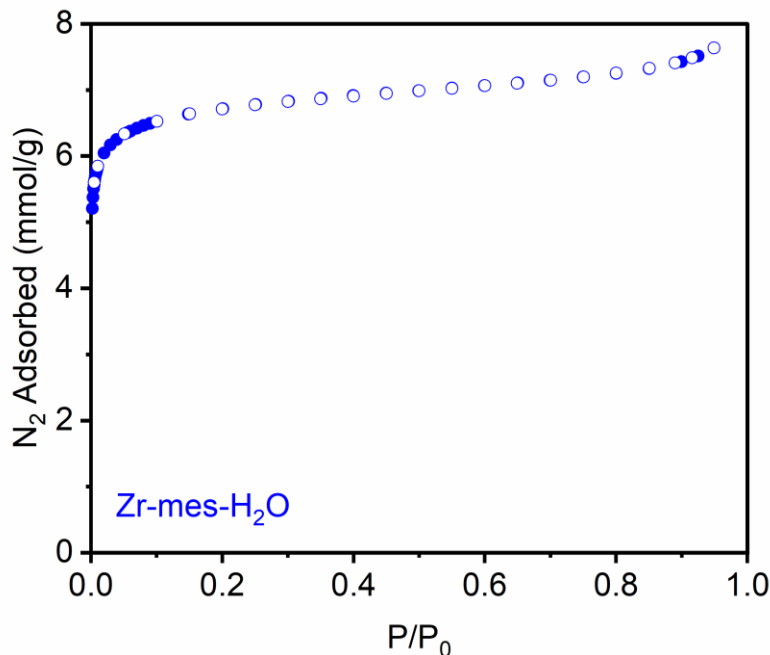


Figure S25. 77 K N_2 adsorption isotherm of activated Zr-mes- H_2O . Desorption data are represented as open circles. Fitting the data yielded a Brunauer-Emmett-Teller (BET) surface area of $688 \pm 1 \text{ m}^2/\text{g}$ (previously reported BET surface area of $725 \text{ m}^2/\text{g}$)³ and a Langmuir surface area of $830 \pm 4 \text{ m}^2/\text{g}$.

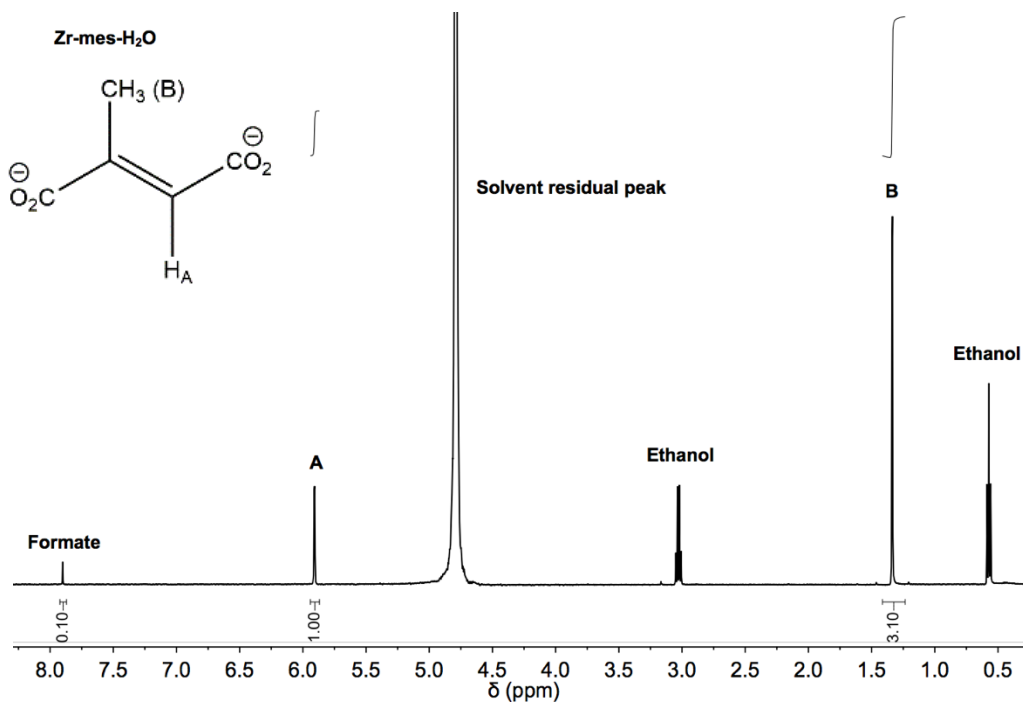


Figure S26. $^1\text{H-NMR}$ (500 MHz, D_2O) spectrum of ethanol-solvated Zr-mes- H_2O digested with a saturated solution of K_3PO_4 in D_2O . Peaks **A** and **B** correspond to the mesaconate linker. The peak corresponding to formate likely arises due to missing linker defects, in which one molecule of mesaconate is replaced by two molecules of formate.

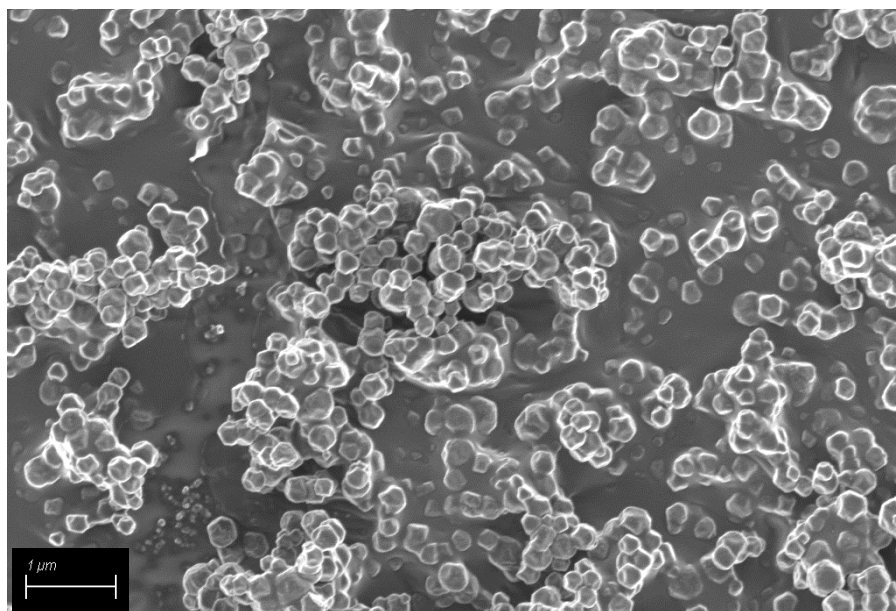


Figure S27. Scanning electron microscopy image (width = 10 μm) of Zr-mes-H₂O.

7. Preparation and characterization of $\text{Zr}_6\text{O}_4(\text{OH})_4(\text{itaconate})_6$, Zr-ita-DMF.

Various acid modulators including acetic acid, L-proline, HCl, pivalic acid, and formic acid were used in an attempt to produce crystalline Zr-ita-DMF. However, in all cases amorphous solids were produced (not shown). Thus, a large-scale batch was prepared with no acid modulator for further characterization. Itaconic acid (0.98 g, 7.50 mmol, 1.00 eq) and ZrCl_4 (1.75 g, 7.50 mmol, 1.00 eq) were added to a screw cap, high pressure reaction vessel equipped with a stir bar. Next, DMF (150 mL) and deionized water (0.40 mL, 22.5 mmol, 3.00 eq) were added, and the reaction vessel was sealed. The mixture was stirred and heated at 120 °C for 24 h. The heterogeneous reaction mixture was allowed to cool to room temperature and filtered. The precipitate was transferred into a screw cap jar filled with DMF (80 mL), and the mixture was allowed to stand for 24 h at room temperature. The DMF was then decanted and replaced with the same volume of fresh DMF. This procedure was repeated an additional two times for a total of three DMF soaks, at which point the DMF was replaced with THF (80 mL) and the process repeated another three times for a total of six washes. The solid was then activated under high vacuum (<100 mbar) at 100 °C overnight to yield $\text{Zr}_6\text{O}_4(\text{OH})_4(\text{itaconate})_6$ as a white solid.

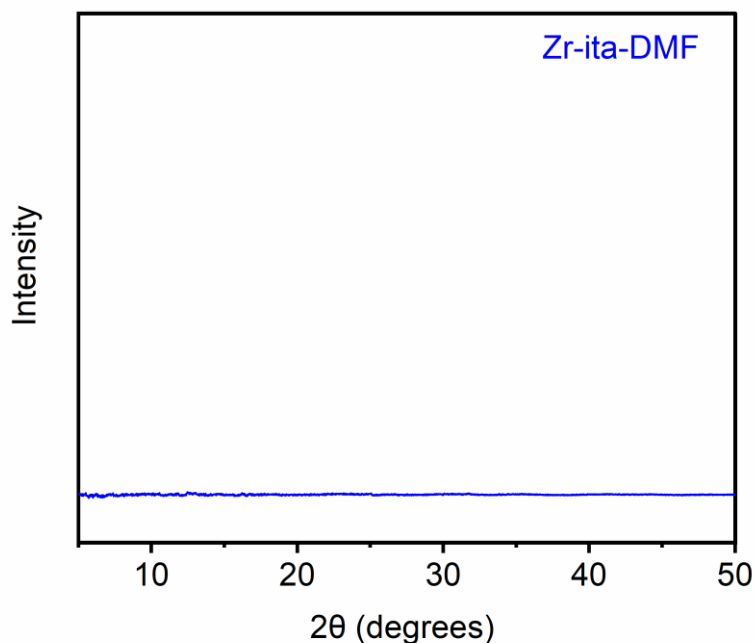


Figure S28. Powder X-ray diffraction pattern ($\lambda = 1.54 \text{ \AA}$) of THF-solvated Zr-ita-DMF, confirming that this material is amorphous.

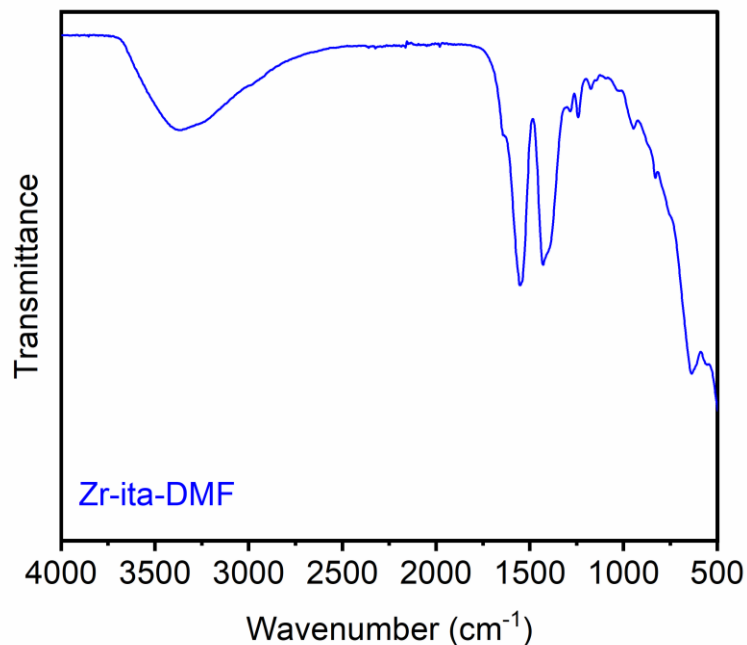


Figure S29. Infrared spectrum of THF-solvated Zr-ita-DMF. A residual amount of DMF is present even after soaking in THF, as evidenced by the small shoulder at 1650 cm⁻¹.

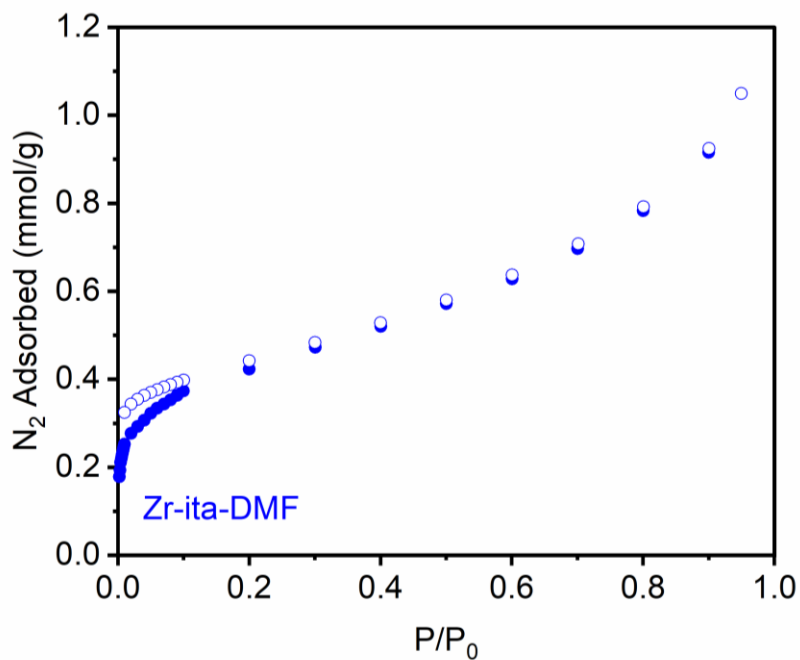


Figure S30. 77 K N₂ adsorption isotherm of activated Zr-ita-DMF. Desorption data are represented as open circles. Fitting the data yielded a Brunauer-Emmett-Teller (BET) surface area of 33 m²/g and a Langmuir surface area of 81 ± 6 m²/g, confirming that this material is effectively non-porous.

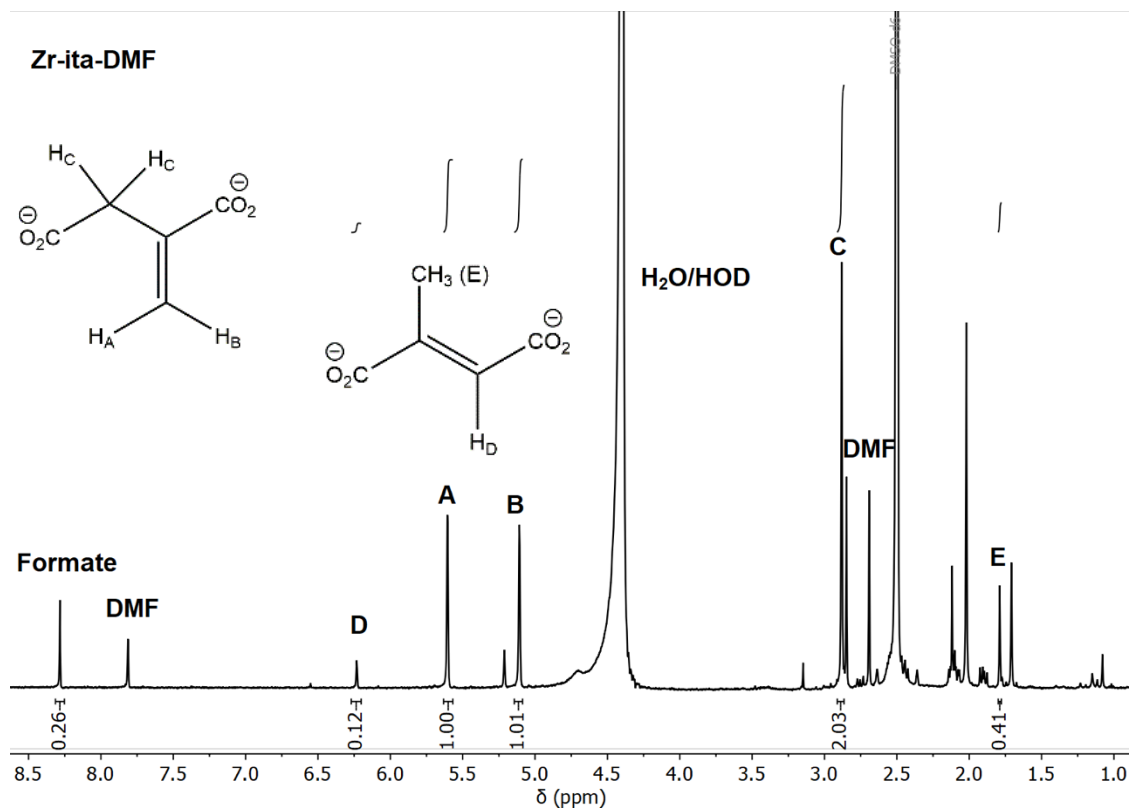


Figure S31. $^1\text{H-NMR}$ (500 MHz, DMSO-d_6) spectra of THF-solvated Zr-ita-DMF digested with a saturated solution of K_3PO_4 in D_2O . Peaks **A**, **B**, and **C** result from the itaconate linker. Isomerization of itaconate to mesaconate was confirmed by the appearance of peaks **D** and **E**, whose integration ratio is 1:3.33 as expected. The addition of water to DMF produces formate and dimethylamine, which likely mediates the isomerization. Consistent with the IR data above (Figure S29), DMF is evident even after extensive soaking in THF. Additional degradation products are also evident. The significant degradation of the linker during the synthesis likely explains the amorphous and non-porous nature of this material.

8. Preparation and characterization of aqueous $\text{Zr}_6\text{O}_4(\text{OH})_4(\text{itaconate})_6$, $\text{Zr-ita-H}_2\text{O}$.

Large-scale preparation. Itaconic acid (1.30 g, 10.0 mmol, 1.00 eq), $\text{ZrOCl}_2 \cdot 8\text{H}_2\text{O}$ (3.22 g, 10.0 mmol, 1.00 eq), and formic acid (0.38 mL, 10.0 mmol, 1.00 eq) were added to a screw cap, high pressure reaction vessel equipped with a stir bar. Next, deionized water (40 mL) was added, and the reaction vessel was sealed. The mixture was stirred and heated at 95 °C for 24 h. The heterogeneous reaction mixture was allowed to cool to room temperature and filtered. The precipitate was transferred into a screw cap jar filled with ethanol (80 mL), and the mixture was allowed to stand for 24 h at room temperature. The ethanol was then decanted and replaced with the same volume of fresh ethanol. This procedure was repeated a total of three times. The solid was then activated under high vacuum (<100 mbar) at 100 °C overnight to yield $\text{Zr}_6\text{O}_4(\text{OH})_4(\text{itaconate})_6$ as a white crystalline solid.

0.5 mol-scale preparation. Itaconic acid (65.1 g, 500. mmol, 1.00 eq), $\text{ZrOCl}_2 \cdot 8\text{H}_2\text{O}$ (162 g, 500. mmol, 1.00 eq), and formic acid (18.9 mL, 500. mmol, 1.00 eq) were added to a 5 L round-bottom flask along with deionized water (2 L) and a stir bar. The reaction mixture was stirred and heated at 105 °C (under reflux) for 24 h. The precipitate was collected by filtration and transferred to a Soxhlet extractor filled with ethanol (2 L). The solid was continually washed with ethanol for five days. The solid was then activated under high vacuum (<100 mbar) at 100 °C for three days to yield $\text{Zr}_6\text{O}_4(\text{OH})_4(\text{itaconate})_6$ as a white crystalline solid (87 g, 73%).

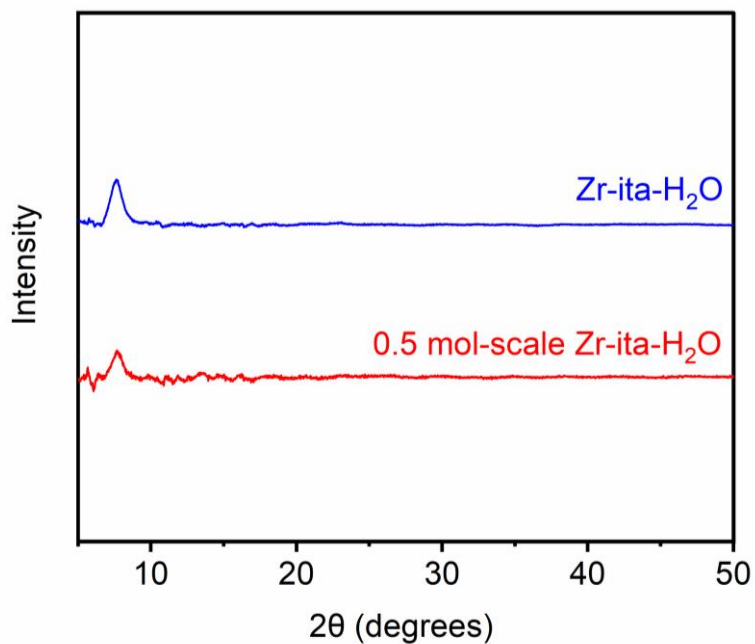


Figure S32. Powder X-ray diffraction patterns ($\lambda = 1.54 \text{ \AA}$) of ethanol-solvated Zr-ita-H₂O and Zr-ita-H₂O prepared on 0.5 mol scale.

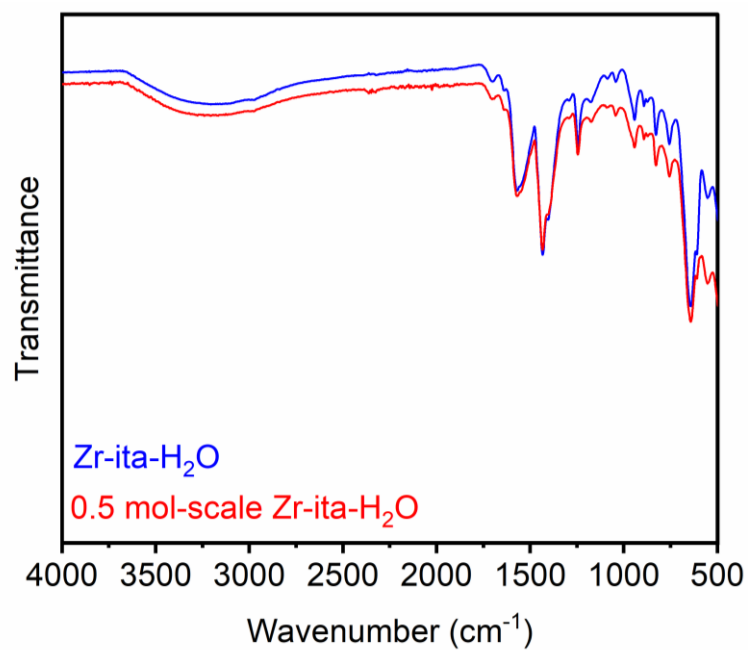


Figure S33. Infrared spectra of ethanol-solvated Zr-ita-H₂O and Zr-ita-H₂O prepared on 0.5 mol scale.

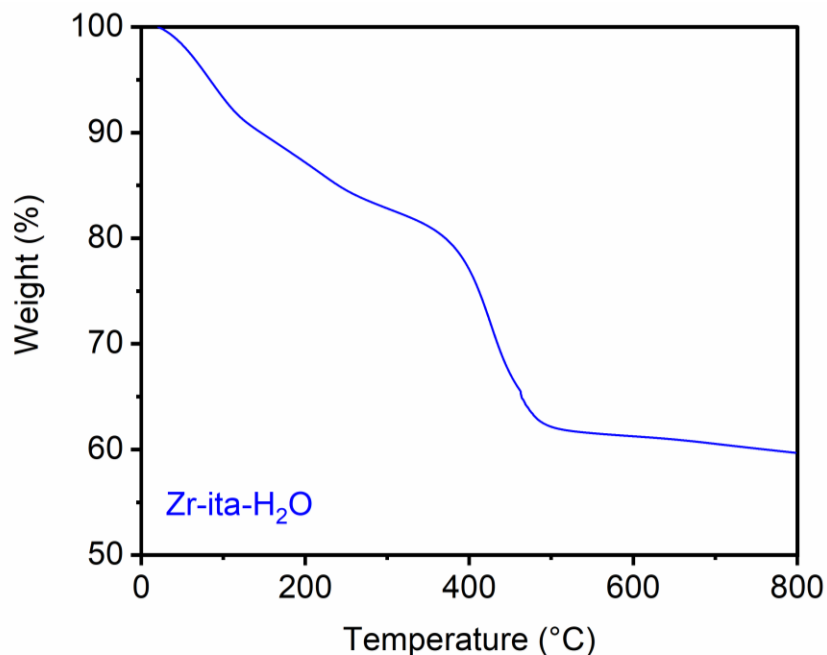


Figure S34. Decomposition profile (ramp rate = 5°C/min) of ethanol-solvated Zr-ita-H₂O.

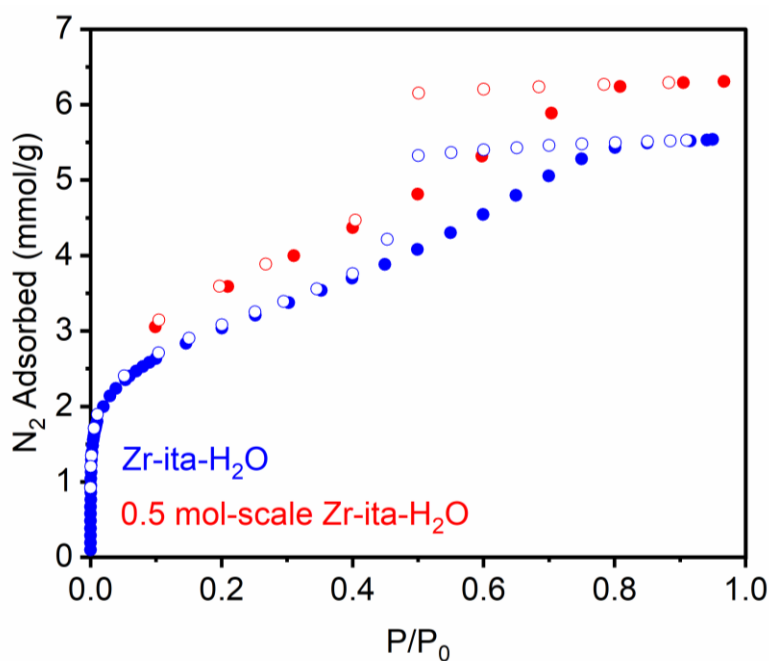


Figure S35. 77 K N₂ adsorption isotherms of activated Zr-ita-H₂O and Zr-ita-H₂O prepared on a 0.5 mol scale. Desorption data are represented as open circles. Fitting the data yielded a Brunauer-Emmett-Teller (BET) surface area of 235 ± 2 m²/g (Zr-ita-H₂O) and Langmuir surface areas of 487 ± 22 m²/g (Zr-ita-H₂O) and 855 m²/g (0.5 mol-scale Zr-ita-H₂O). The hysteresis observed upon desorption is likely due to the presence of mesoporous defects.

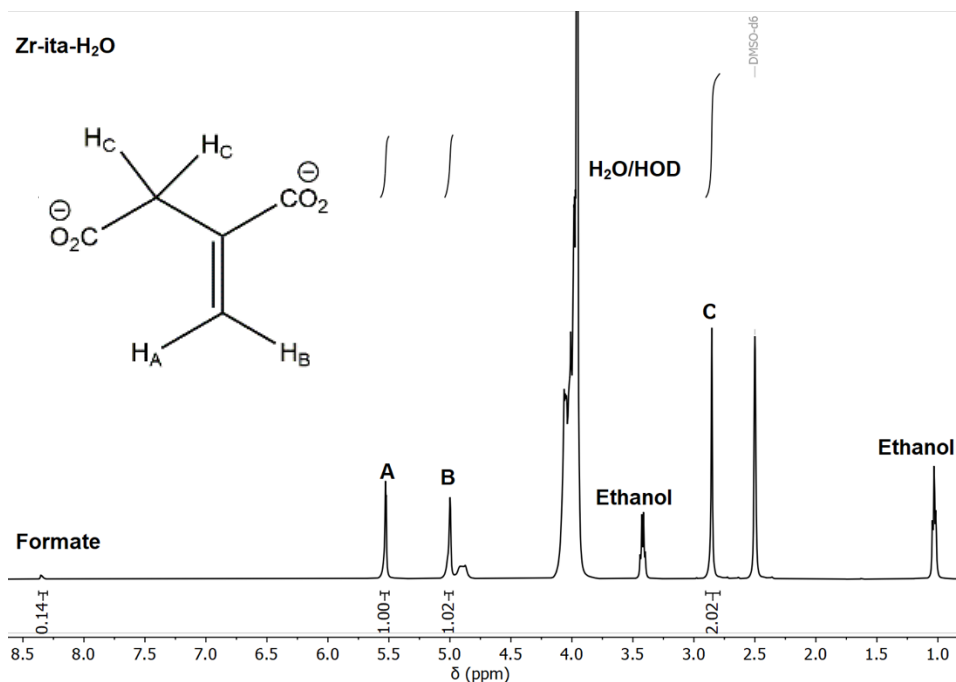


Figure S36. ¹H-NMR (500 MHz, DMSO-d₆) spectrum of ethanol-solvated Zr-ita-H₂O digested with a saturated solution of K₃PO₄ in D₂O. Peaks **A**, **B**, and **C** result from the itaconate linker. Note the lack of isomerization when this MOF is prepared in water as opposed to in DMF (Figure S31).

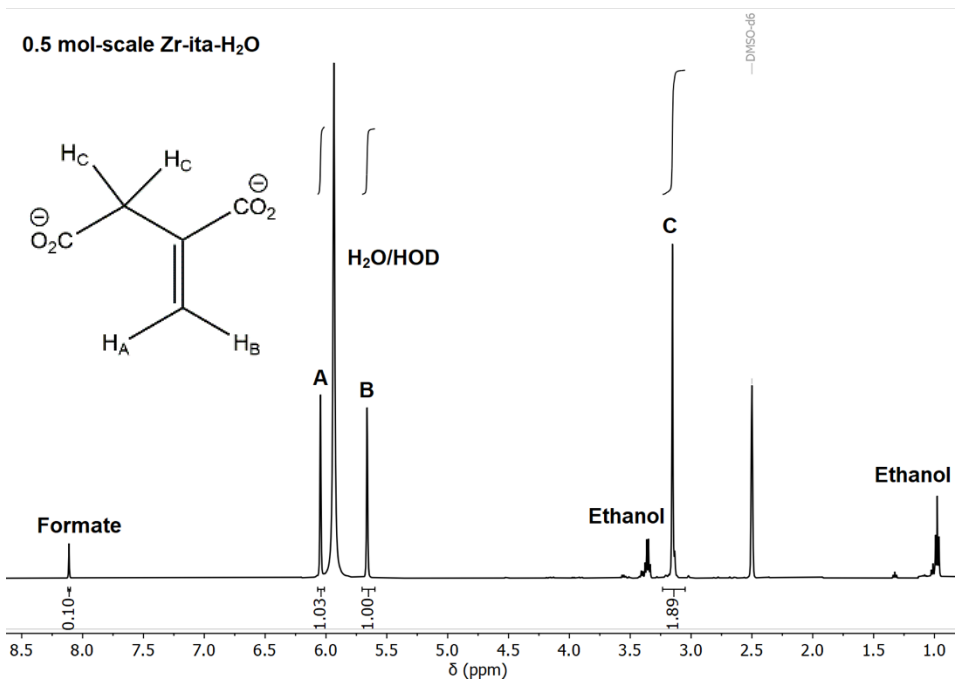


Figure S37. ¹H-NMR (500 MHz, DMSO-d₆) spectrum of ethanol-solvated 0.5 mol-scale Zr-ita-H₂O digested with a saturated solution of K₃PO₄ in D₂O. Peaks **A**, **B**, and **C** result from the itaconate linker.

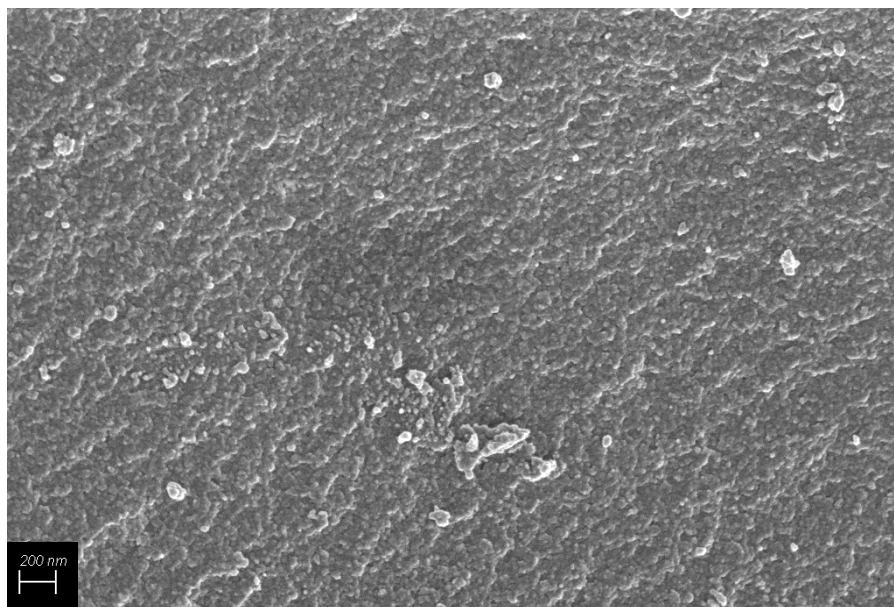


Figure S38. Scanning electron microscopy image (width = 5 μm) of Zr-ita-H₂O, confirming that this material is largely amorphous.

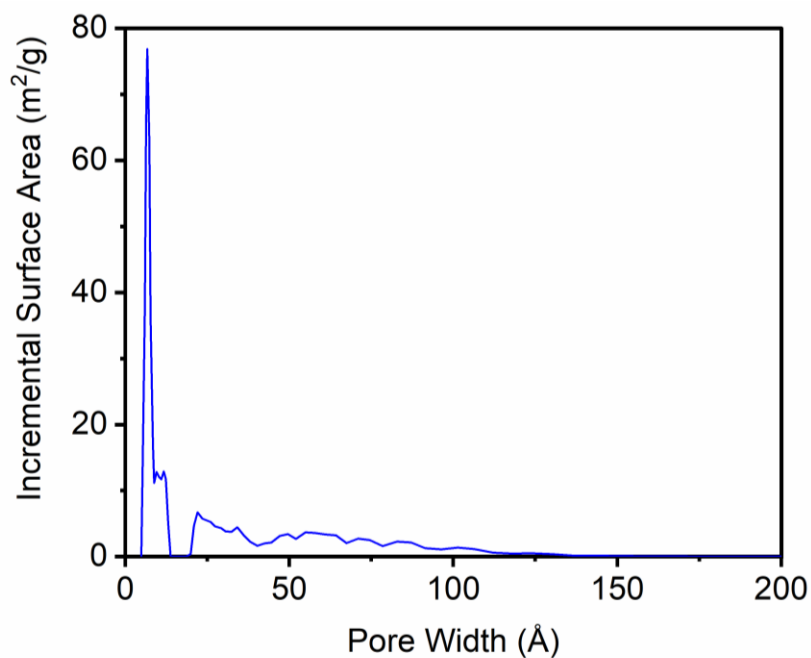


Figure S39. Pore size distribution plot for Zr-ita-H₂O using the adsorption data in Figure S35. The maximum occurs at a pore width of 6.6 Å. Consistent with the hysteresis observed upon desorption (Figure S35), mesoporous defects are observed ranging from 20 to 100 Å in size.

Table S1. BET and Langmuir surface areas calculated from the N₂ adsorption isotherms in the preceding sections.

MOF	BET surface area (m ² /g)	Langmuir surface area (m ² /g)
Zr-fum-DMF	988 ± 1	1322 ± 2
Zr-fum-H ₂ O	873 ± 2	1196 ± 9
Zr-mes-DMF	583 ± 1	663 ± 2
Zr-mes-H ₂ O	688 ± 1	830 ± 4
Zr-ita-DMF	33	81 ± 6
Zr-ita-H ₂ O	235 ± 2	487 ± 22

9. Water adsorption isotherms of MOFs prepared under aqueous conditions.

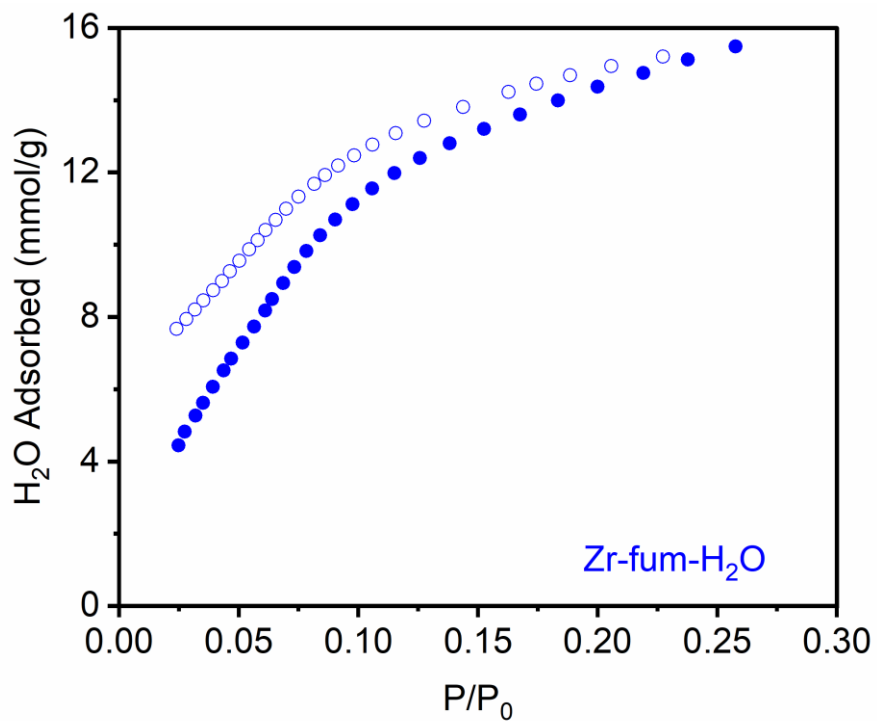


Figure S40. 35 °C water adsorption isotherm of activated Zr-fum-H₂O. Desorption data are represented as open circles and suggest that the binding of water to this MOF is only semi-reversible at this temperature.

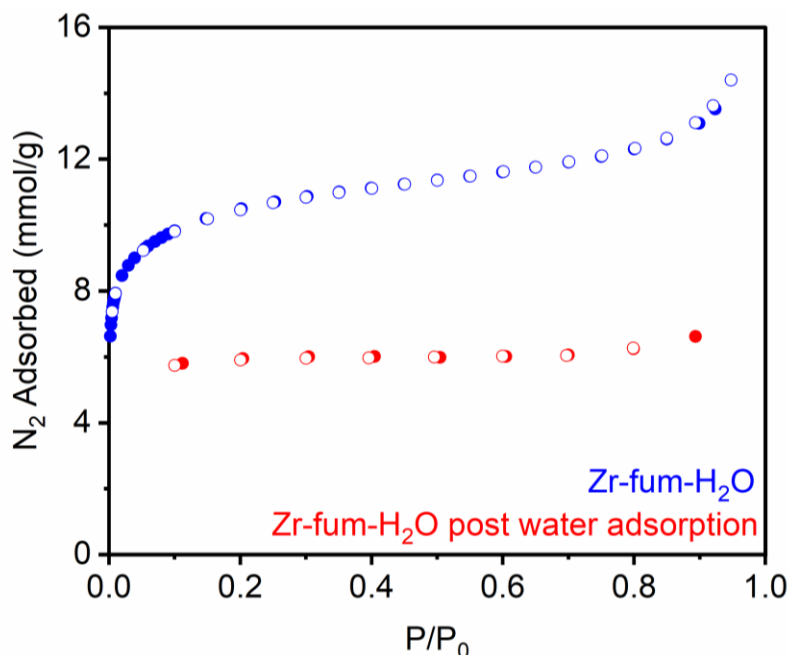


Figure S41. 77 K N_2 adsorption isotherms of Zr-fum- H_2O pre- and post- water adsorption isotherm (Figure S40). Desorption data are represented as open circles. Zr-fum- H_2O was regenerated after water adsorption at 100 °C for 48 h followed by reactivation at 125 °C for 48 h in an attempt to remove all adsorbed water. The measured Langmuir surface area after the water adsorption isotherm was $590 \pm 2 \text{ m}^2/\text{g}$ (originally $1196 \pm 9 \text{ m}^2/\text{g}$), indicating that water adsorption in this MOF is partially irreversible.

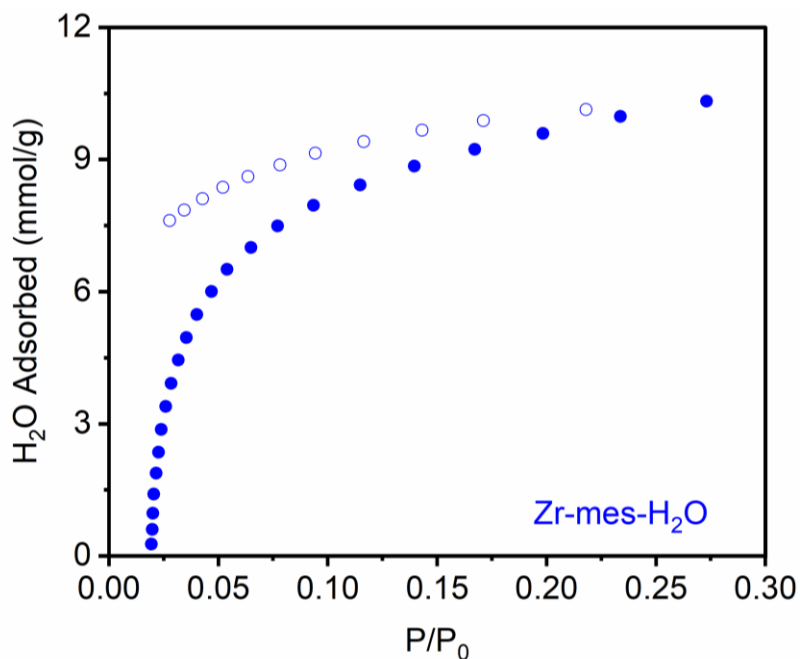


Figure S42. 35 °C water adsorption isotherms of activated Zr-mes- H_2O . Desorption data are represented as open circles and suggest that the binding of water to this MOF is only semi-reversible at this temperature.

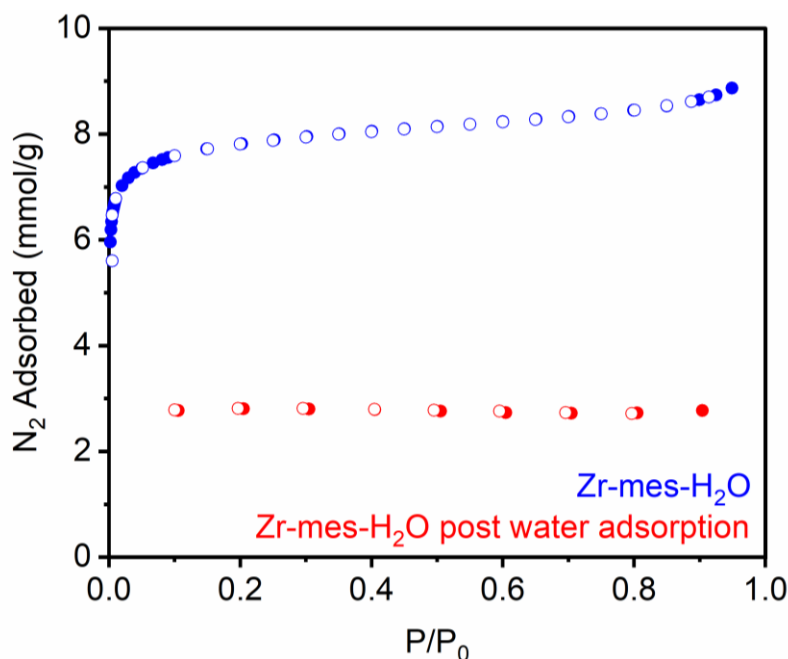


Figure S43. 77 K N_2 adsorption isotherms of Zr-mes- H_2O pre- and post- water adsorption isotherm (Figure S42). Desorption data are represented as open circles. Zr-mes- H_2O was regenerated after water adsorption at 100 °C for 48 h followed by reactivation at 125 °C for 48 h in an attempt to remove all adsorbed water. The measured Langmuir surface area after the water adsorption isotherm was $261 \pm 1 \text{ m}^2/\text{g}$ (originally $830 \pm 4 \text{ m}^2/\text{g}$), indicating that water adsorption in this MOF is partially irreversible.

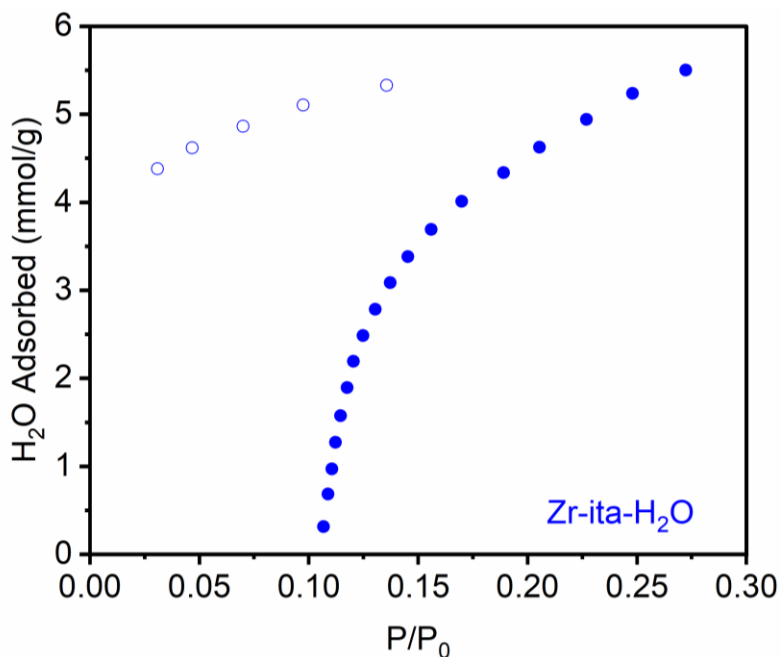


Figure S44. 35 °C water adsorption isotherms of activated Zr-ita- H_2O . Desorption data are represented as open circles and suggest that the binding of water to this MOF is only semi-reversible at this temperature.

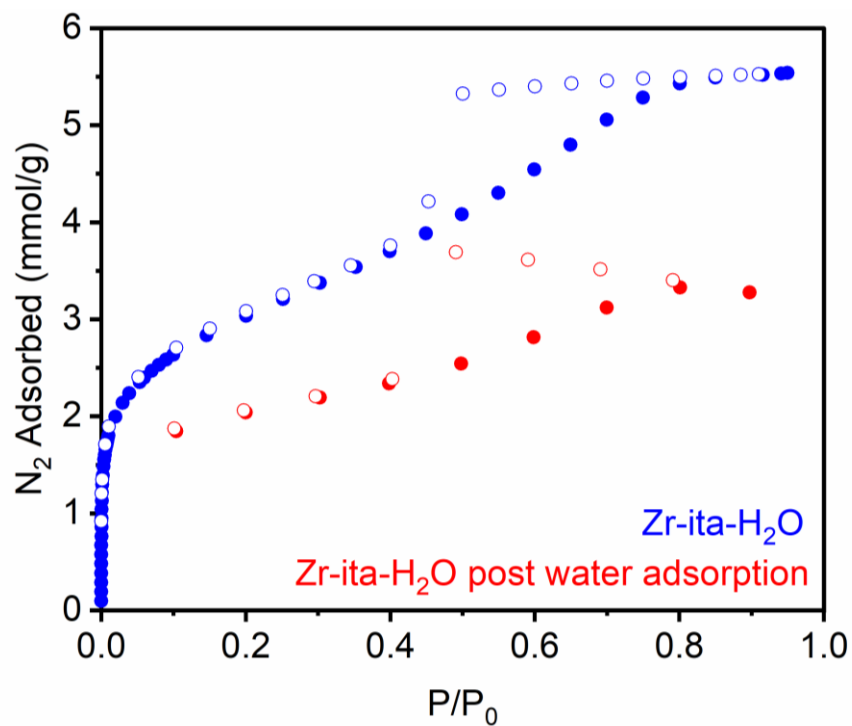


Figure S45. 77 K N₂ adsorption isotherms of Zr-ita-H₂O pre- and post- water adsorption isotherm (Figure S44). Desorption data are represented as open circles. Zr-ita-H₂O was regenerated after water adsorption at 100 °C for 48 h followed by reactivation at 125 °C for 48 h in an attempt to remove all adsorbed water. The measured Langmuir surface area after the water adsorption isotherm was 296 ± 19 m²/g (originally 487 ± 22 m²/g), indicating that water adsorption in this MOF is partially irreversible.

10. H₂S adsorption isotherms of MOFs prepared under aqueous conditions.

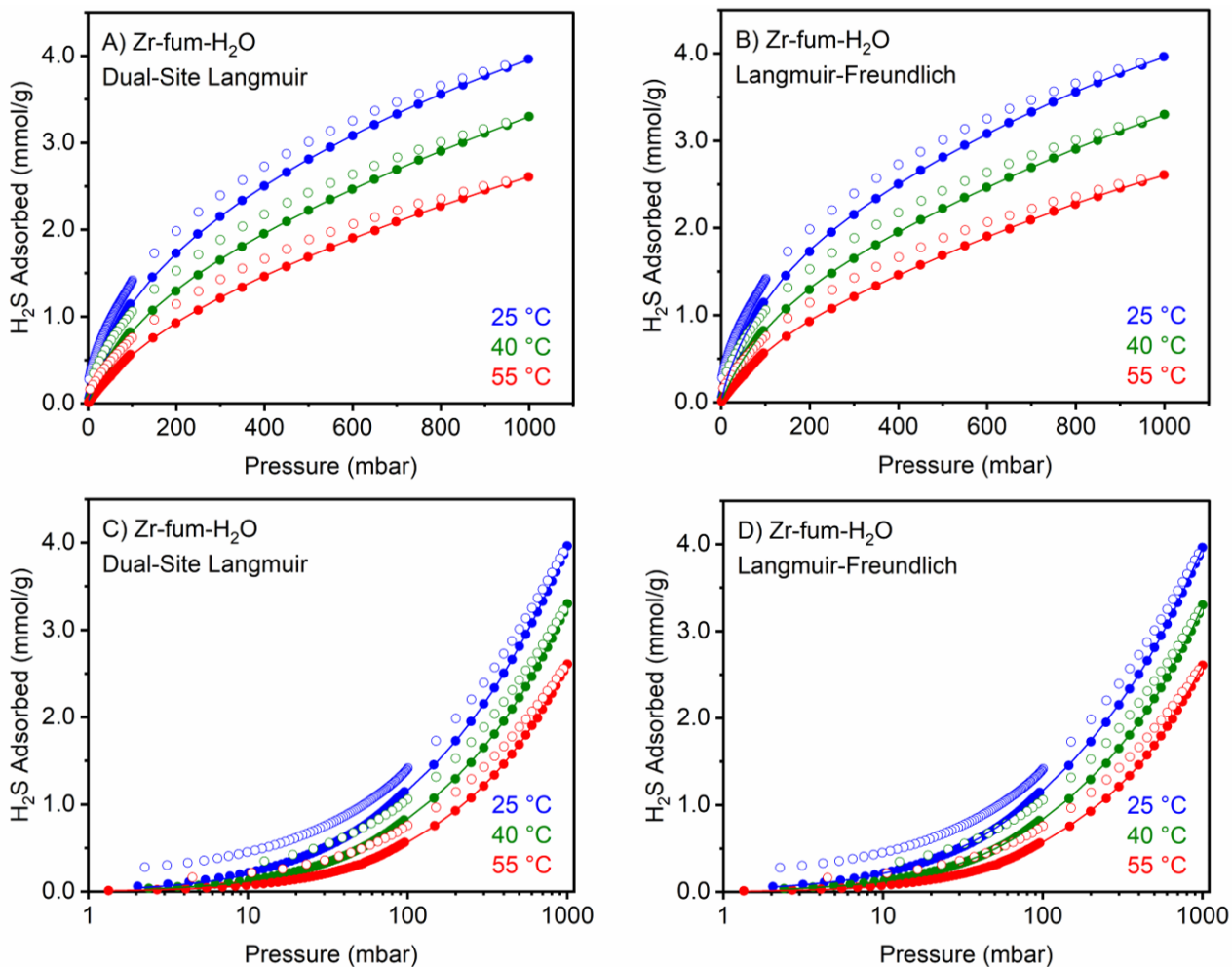


Figure S46. H₂S adsorption isotherms at 25 °C, 40 °C, and 55 °C of activated Zr-fum-H₂O. Solid lines represent fits to dual-site Langmuir (A, C) and Langmuir-Freundlich models (B, D). A data point was considered equilibrated after <0.01% pressure change occurred over a 45 s interval.

Table S2. Langmuir fit parameters determined from the fits in Figure S46.

Dual-Site Langmuir model			
Parameter	25 °C	40 °C	55 °C
Q _{sat1} (mmol/g)	1.20	8.66	7.41
S1 (in multiples of R)	0.152	1.05	1.19
E1 (kJ/mol)	7.04	2.34 x 10 ⁻³	0.425
V1	1.00	1.00	1.00
Q _{sat2} (mmol/g)	7.02	1.15	0.753
S2 (in multiples of R)	1.37	8.01 x 10 ⁻⁴	3.39 x 10 ⁻²
E2 (kJ/mol)	2.42	5.63	5.38
V2	1.00	1.00	1.00
R ²	0.99988	0.99992	0.99986
Langmuir-Freundlich Model			
Parameter	25 °C	40 °C	55 °C
Q _{sat1} (mmol/g)	4.20	9.30	2.32
S1 (in multiples of R)	0	1.50	0.154
E1 (kJ/mol)	2.46	2.34 x 10 ⁻³	0
V1	0.852	1.20	2.10
Q _{sat2} (mmol/g)	1.83	1.89	1.85
S2 (in multiples of R)	0.258	8.01 x 10 ⁻⁴	0
E2 (kJ/mol)	0.514	4.44	4.32
V2	2.37	0.967	1.05
R ²	0.99996	0.99994	0.99994

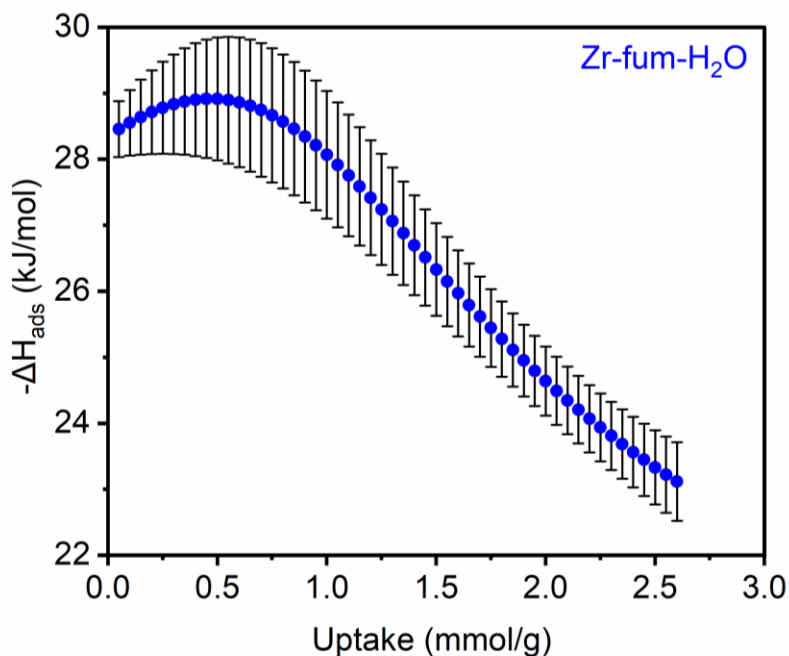


Figure S47. Heat of adsorption ($-\Delta H_{\text{ads}}$) for H_2S adsorption as a function of uptake for Zr-fum- H_2O , as determined using the Dual-Site Langmuir fits in Figure S46. The $-\Delta H_{\text{ads}}$ values obtained from the Langmuir-Freundlich fits are included in Figure 4 of the main text.

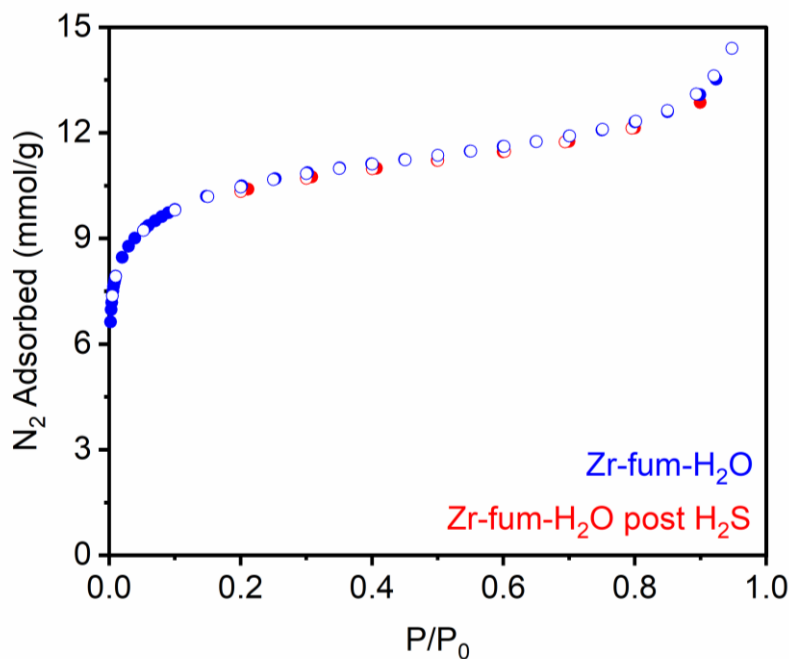


Figure S48. 77 K N_2 adsorption isotherms of Zr-fum- H_2O pre- and post- H_2S adsorption isotherm at 25 °C (Figure S46). Desorption data are represented as open circles. Zr-fum- H_2O was regenerated after H_2S adsorption at 100 °C for 48 h. The measured Langmuir surface area after the H_2S adsorption isotherm was $1183 \pm 15 \text{ m}^2/\text{g}$ (originally $1196 \pm 9 \text{ m}^2/\text{g}$), indicating that H_2S binds reversibly in this MOF.

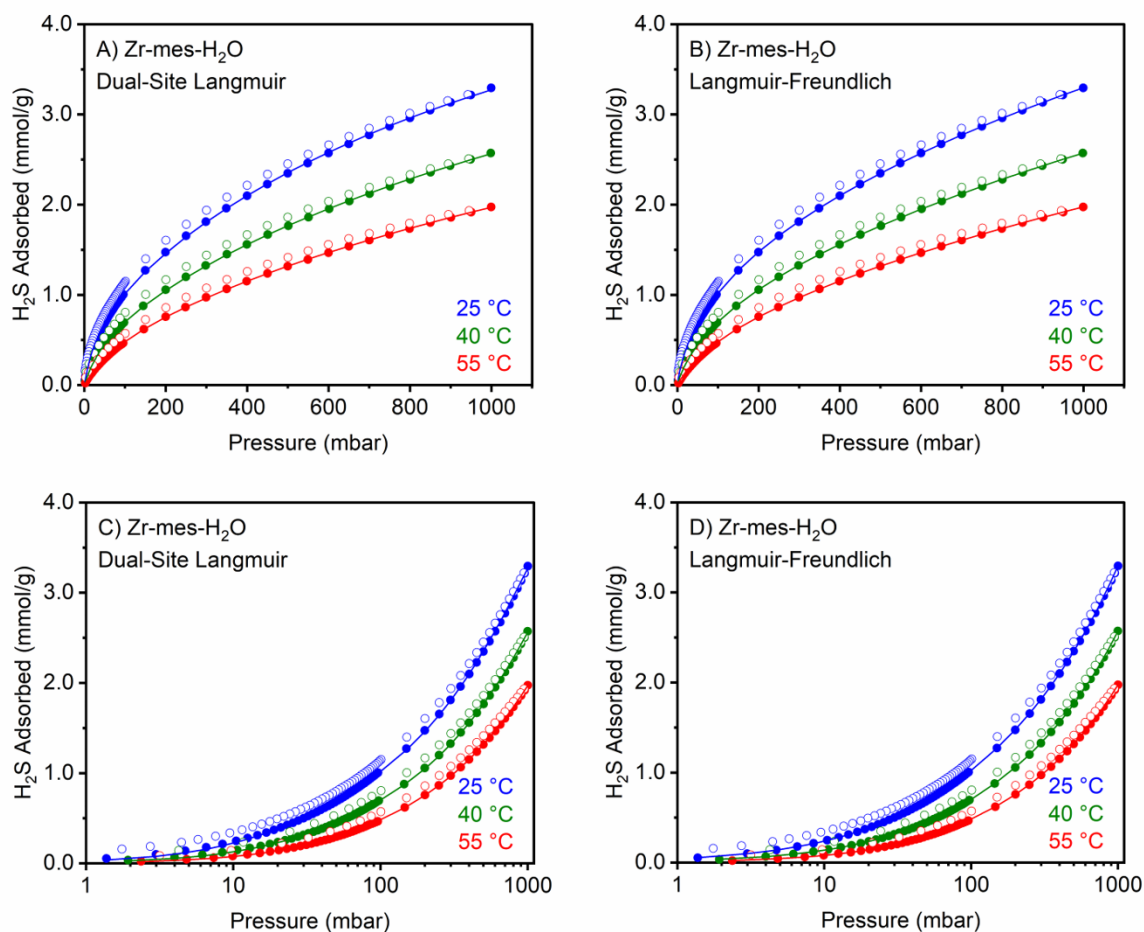


Figure S49. H₂S adsorption isotherms at 25 °C, 40 °C, and 55 °C of activated Zr-mes-H₂O. Solid lines represent fits to dual-site Langmuir (A, C) and Langmuir-Freundlich models (B, D). A data point was considered equilibrated after <0.01% pressure change occurred over a 45 s interval.

Table S3. Langmuir fit parameters determined from the fits in Figure S49.

Dual-Site Langmuir model			
Parameter	25 °C	40 °C	55 °C
Q _{sat1} (mmol/g)	0.823	5.56	0.503
S1 (in multiples of R)	0.150	0.620	3.03
E1 (kJ/mol)	8.66	2.34 x 10 ⁻³	15.1
V1	1.00	1.00	1.00
Q _{sat2} (mmol/g)	5.67	0.653	4.97
S2 (in multiples of R)	1.27	8.01 x 10 ⁻⁴	5.15
E2 (kJ/mol)	2.52	7.49	11.8
V2	1.00	1.00	1.00
R ²	0.99993	0.99997	0.99999
Langmuir-Freundlich Model			
Parameter	25 °C	40 °C	55 °C
Q _{sat1} (mmol/g)	1.73	6.77	0.649
S1 (in multiples of R)	9.61 x 10 ⁻²	1.32	0
E1 (kJ/mol)	4.10	2.29 x 10 ⁻³	5.08
V1	0.764	1.07	0.909
Q _{sat2} (mmol/g)	7.32	1.43	6.30
S2 (in multiples of R)	1.07	7.96 x 10 ⁻⁴	1.24
E2 (kJ/mol)	3.92 x 10 ⁻⁵	3.70	9.11 x 10 ⁻⁶
V2	0.996	0.817	0.957
R ²	0.99999	0.99999	0.99999

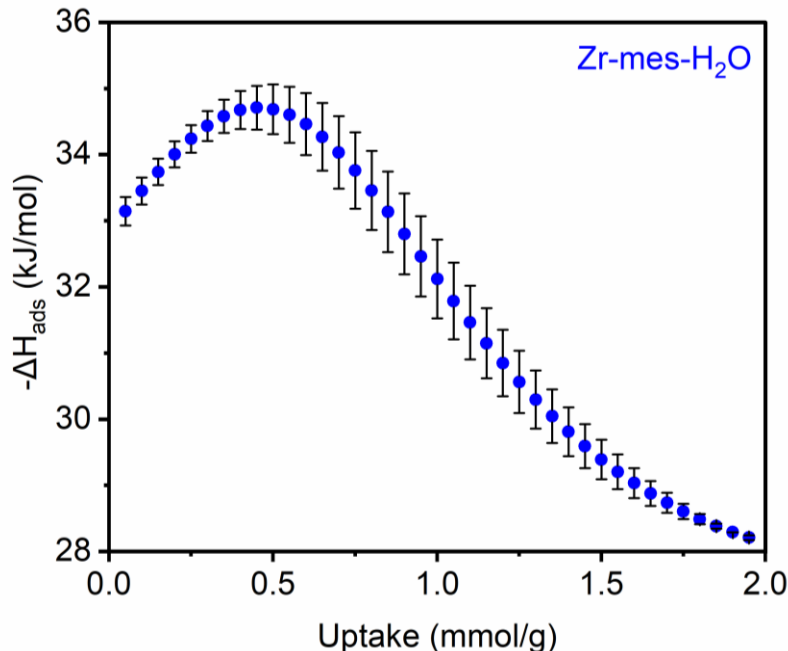


Figure S50. Heat of adsorption ($-\Delta H_{\text{ads}}$) for H_2S adsorption as a function of uptake for Zr-mes- H_2O , as determined using the Dual-Site Langmuir fits in Figure S49. The $-\Delta H_{\text{ads}}$ values obtained from the Langmuir-Freundlich fits are included in Figure 4 of the main text.

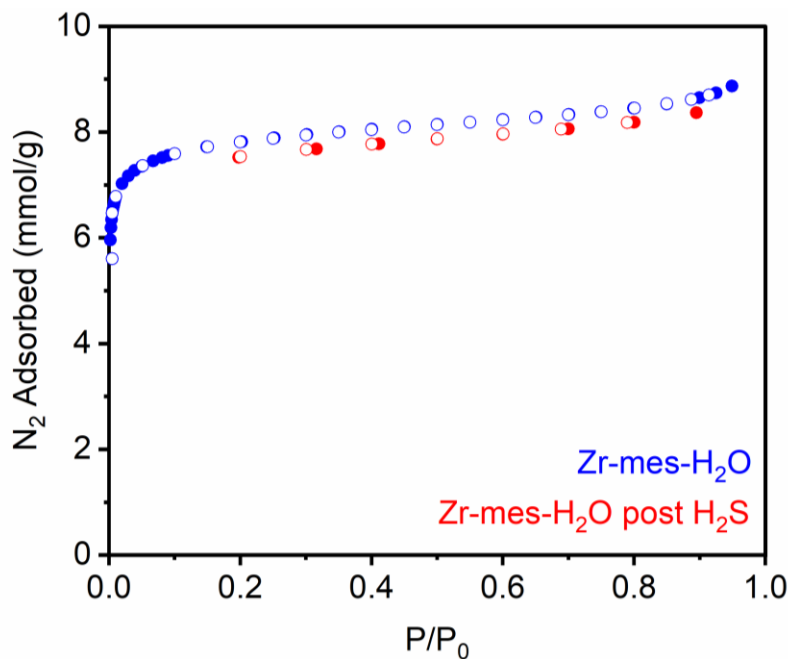


Figure S51. 77 K N_2 adsorption isotherms of Zr-mes- H_2O pre- and post- H_2S adsorption isotherm at 25 °C (Figure S49). Desorption data are represented as open circles. Zr-mes- H_2O was regenerated after H_2S adsorption at 100 °C for 48 h. The measured Langmuir surface area after the H_2S adsorption isotherm was $820 \pm 7 \text{ m}^2/\text{g}$ (originally $830 \pm 4 \text{ m}^2/\text{g}$), indicating that H_2S binds reversibly in this MOF.

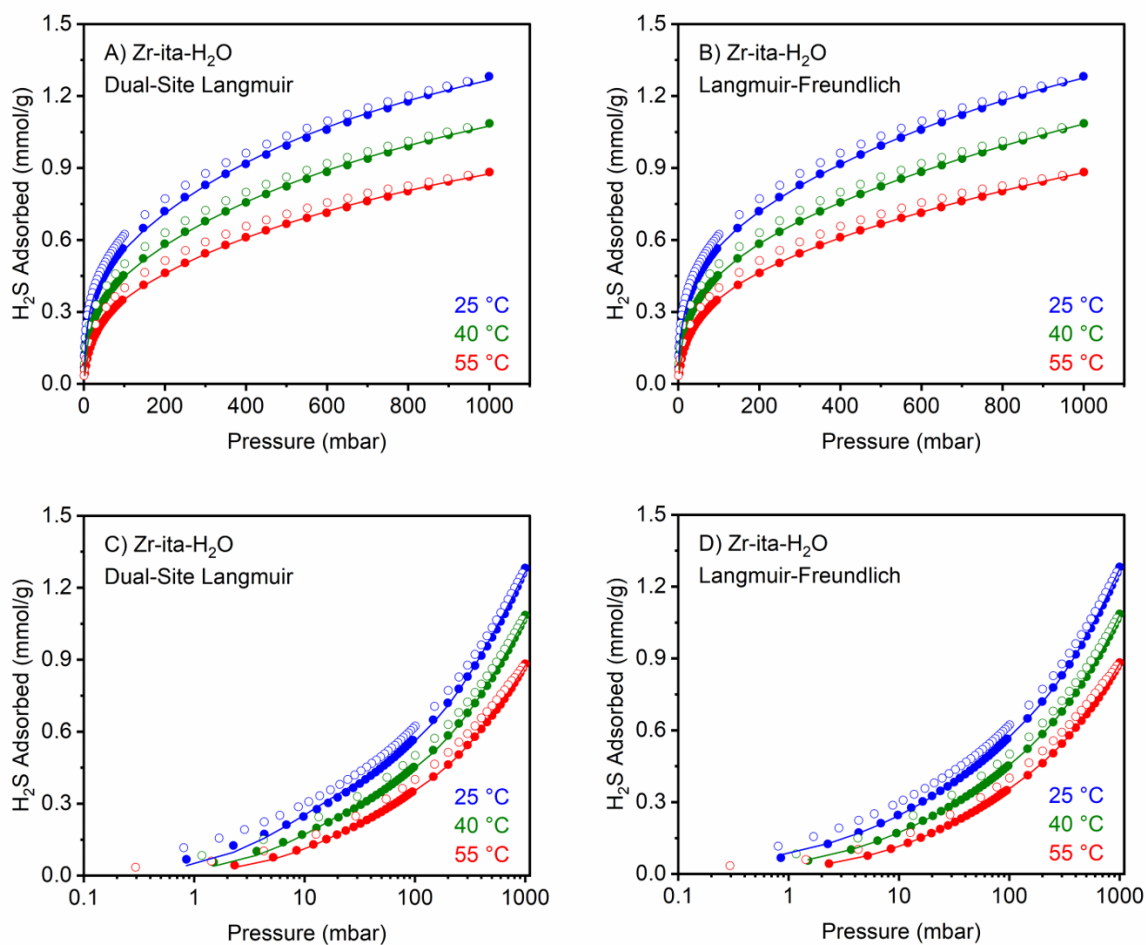


Figure S52. H₂S adsorption isotherms at 25 °C, 40 °C, and 55 °C of activated Zr-ita-H₂O. Solid lines represent fits to dual-site Langmuir (A, C) and Langmuir-Freundlich models (B, D). A data point was considered equilibrated after <0.01% pressure change occurred over a 45 s interval.

Table S4. Langmuir fit parameters determined from the fits in Figure S52.

Dual-Site Langmuir model			
Parameter	25 °C	40 °C	55 °C
Q_{sat1} (mmol/g)	0.424	1.46	0.308
S1 (in multiples of R)	0.147	3.31×10^{-2}	2.70
E1 (kJ/mol)	12.3	2.34×10^{-3}	18.0
V1	1.00	1.00	1.00
Q_{sat2} (mmol/g)	1.53	0.361	1.26
S2 (in multiples of R)	0.984	8.01×10^{-4}	4.64
E2 (kJ/mol)	2.97	11.3	12.2
V2	1.00	1.00	1.00
R^2	0.99983	0.99992	0.99997
Langmuir-Freundlich Model			
Parameter	25 °C	40 °C	55 °C
Q_{sat1} (mmol/g)	0.654	5.15	0.412
S1 (in multiples of R)	0.146	1.79	2.55×10^{-4}
E1 (kJ/mol)	5.53	7.50×10^{-11}	6.85
V1	0.589	0.668	0.775
Q_{sat2} (mmol/g)	2.43	0.372	1.66
S2 (in multiples of R)	0.908	7.59×10^{-4}	0.844
E2 (kJ/mol)	0	7.03	0
V2	0.854	0.709	0.940
R^2	0.99999	0.99999	0.99999

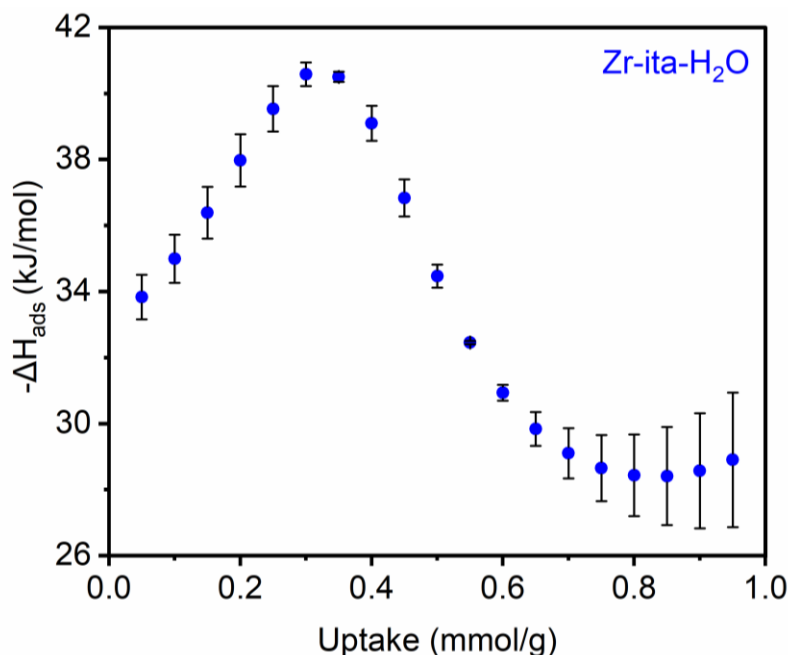


Figure S53. Heat of adsorption ($-\Delta H_{\text{ads}}$) for H_2S adsorption as a function of uptake for Zr-ita- H_2O , as determined using the Dual-Site Langmuir fits in Figure S52. The $-\Delta H_{\text{ads}}$ values obtained from the Langmuir-Freundlich fits are included in Figure 4 of the main text.

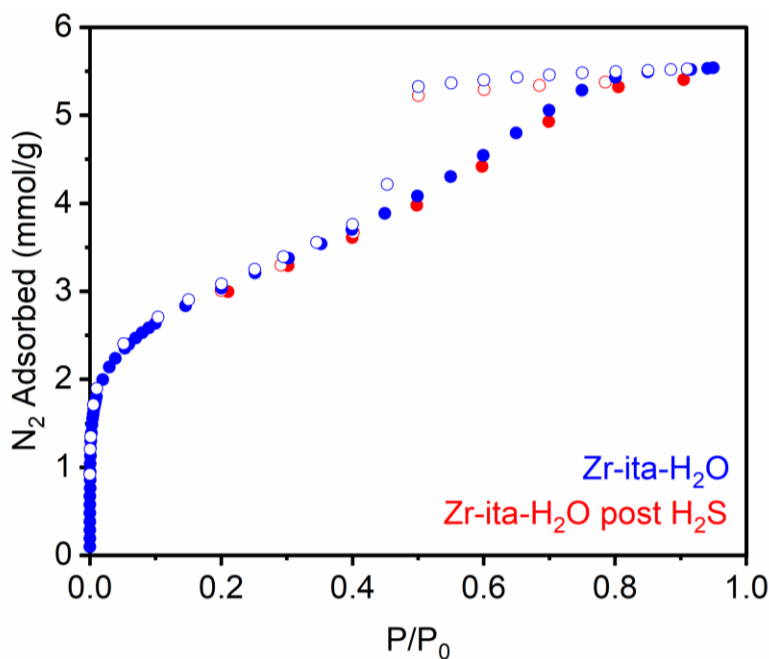


Figure S54. 77 K N_2 adsorption isotherms of Zr-ita- H_2O pre- and post- H_2S adsorption isotherm at 25 °C (Figure S52). Desorption data are represented as open circles. Zr-ita- H_2O was regenerated after H_2S adsorption at 100 °C for 48 h. The measured Langmuir surface area after the H_2S adsorption isotherm was $511 \pm 36 \text{ m}^2/\text{g}$ (originally $487 \pm 22 \text{ m}^2/\text{g}$), indicating that H_2S binds reversibly in this MOF.

11. Characterization of MOFs prepared under aqueous conditions exposed to H₂S solution.

General procedure. In a nitrogen-filled glovebox, a 15 mL screw cap reaction tube was loaded with desolvated MOF (~50 mg) and capped. The tube was removed from the glovebox and placed under a dry atmosphere of nitrogen. Next, H₂S in THF (0.8 M, 1.0 mL) was added *via* syringe under a constant stream of nitrogen. The cap was replaced with one that had not been punctured, and the tube was left to stand for 48 h at 50 °C. The MOFs were collected by filtration and washed with THF into a filter flask containing bleach to quench any remaining H₂S. The solids were then characterized.

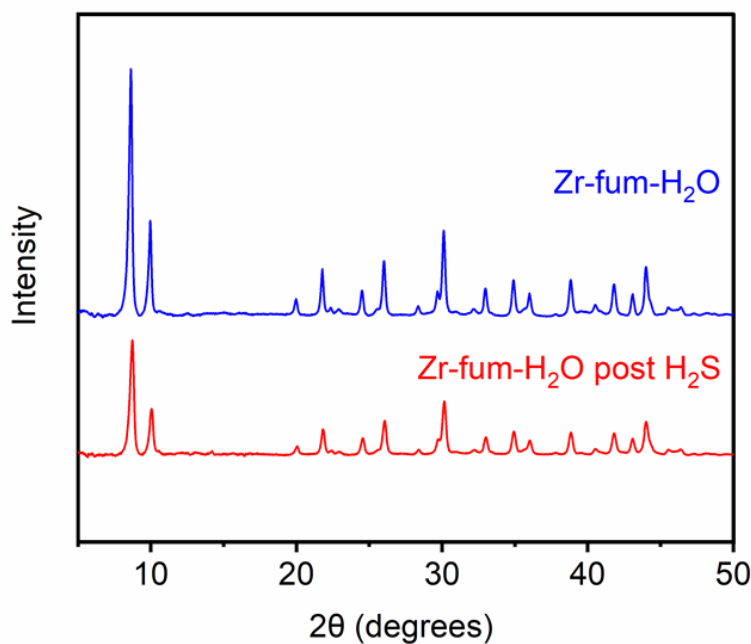


Figure S55. Powder X-ray diffraction patterns ($\lambda = 1.54 \text{ \AA}$) of Zr-fum-H₂O pre- and post-exposure to H₂S in THF.

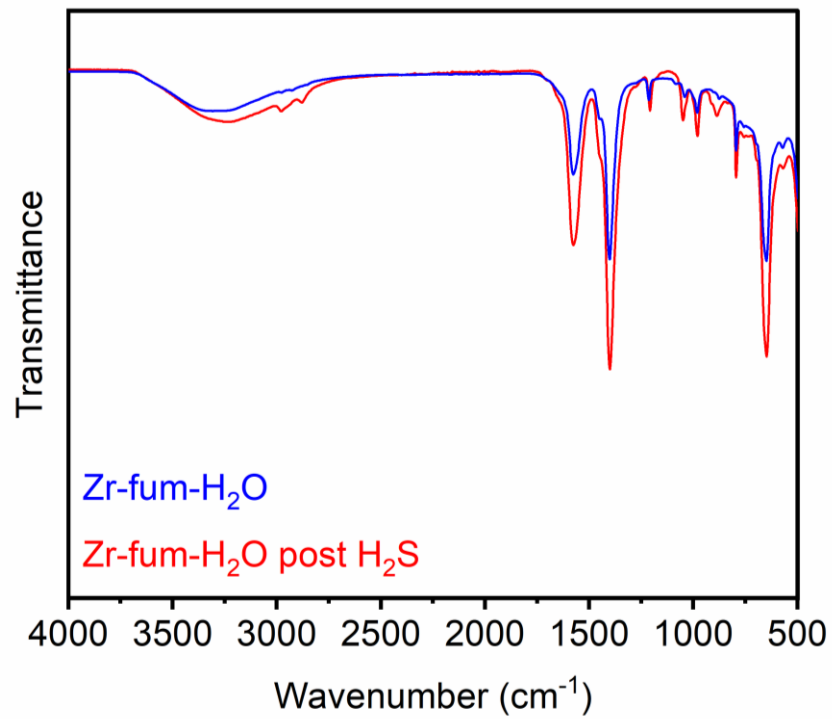


Figure S56. Infrared spectra of Zr-fum-H₂O pre- and post-exposure to H₂S in THF.

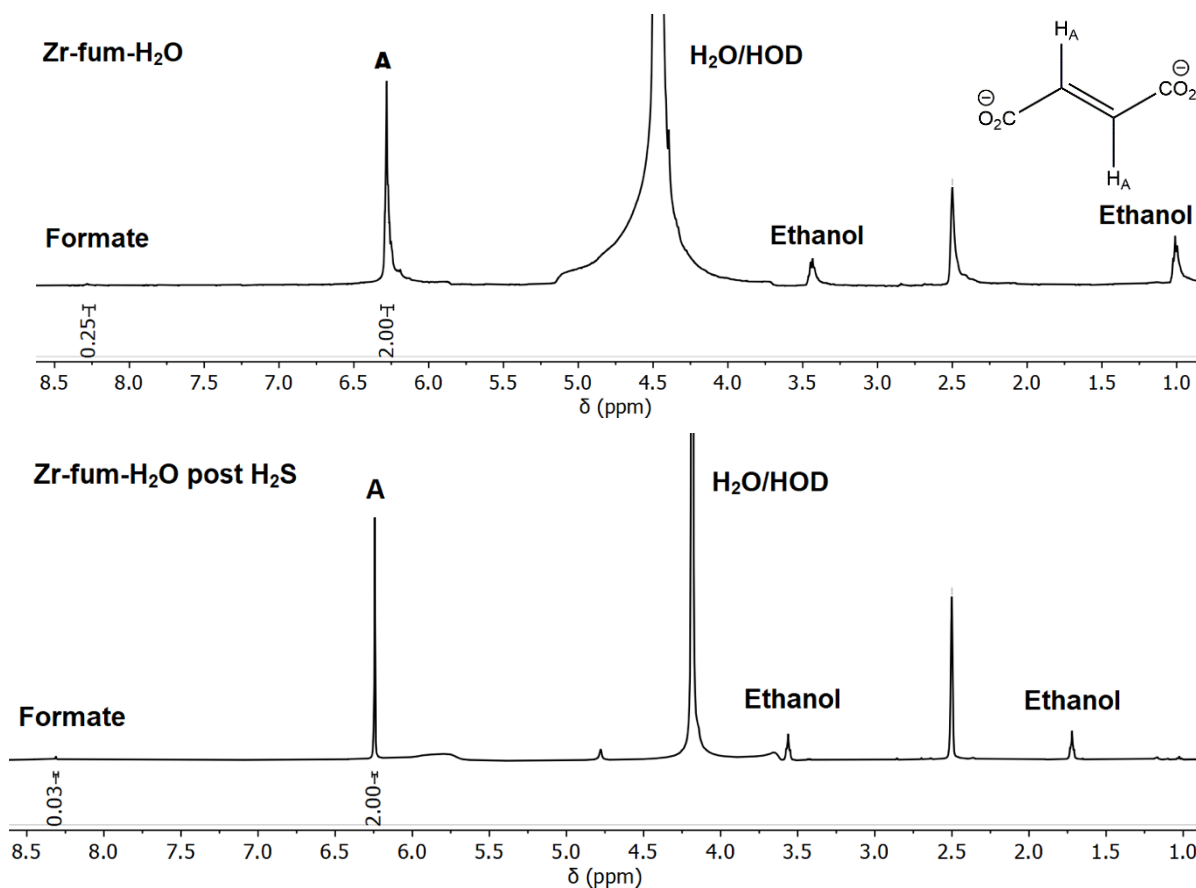


Figure S57. ¹H-NMR (500 MHz, DMSO-d₆) spectra of ethanol-solvated Zr-fum-H₂O pre- (top) and post-exposure (bottom) to H₂S in THF. Digested using a saturated solution of K₃PO₄ in D₂O. Peak A corresponds to the fumarate linker. No significant changes to the linker were observed.

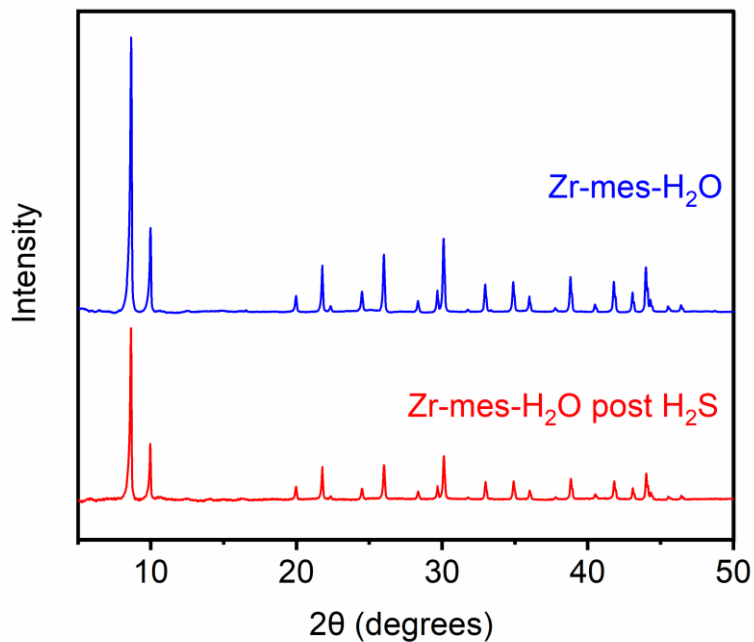


Figure S58. Powder X-ray diffraction patterns ($\lambda = 1.54 \text{ \AA}$) of Zr-mes-H₂O pre- and post-exposure to H₂S in THF.

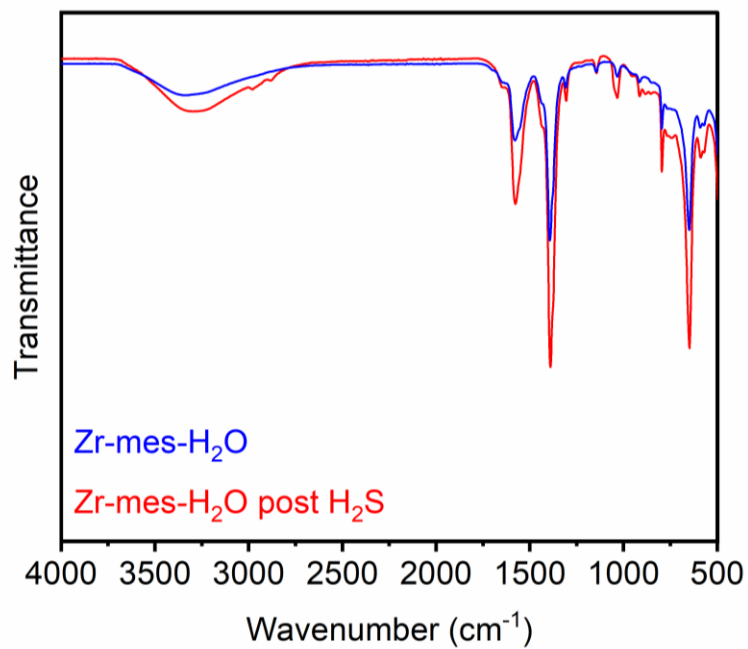


Figure S59. Infrared spectra of Zr-mes-H₂O pre- and post-exposure to H₂S in THF.

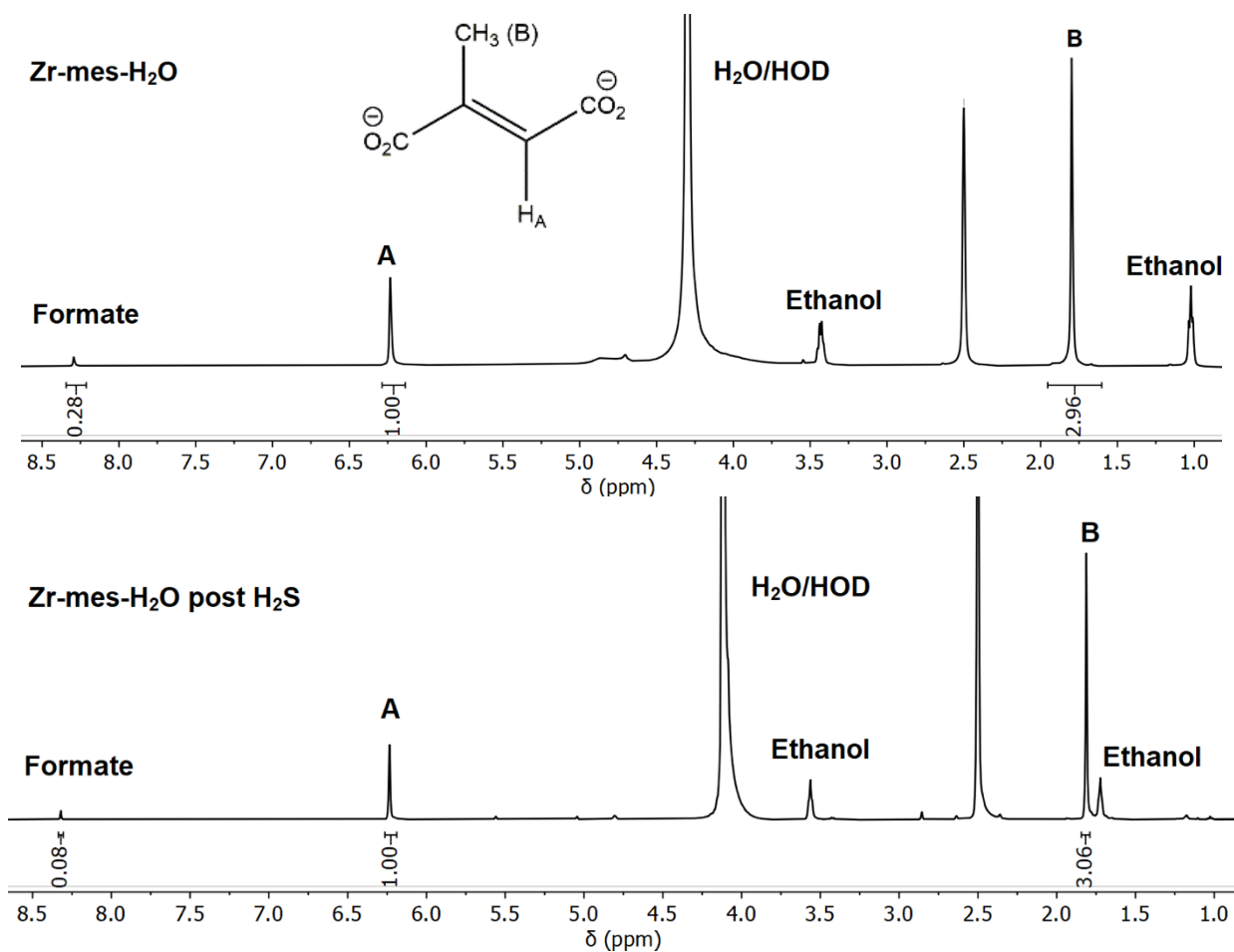


Figure S60. ¹H-NMR (500 MHz, DMSO-d₆) spectra of ethanol-solvated Zr-mes-H₂O pre- (top) and post-exposure (bottom) to H₂S in THF. Digested using a saturated solution of K₃PO₄ in D₂O. Peaks **A** and **B** correspond to the mesaconate linker. No significant changes to the linker were observed.

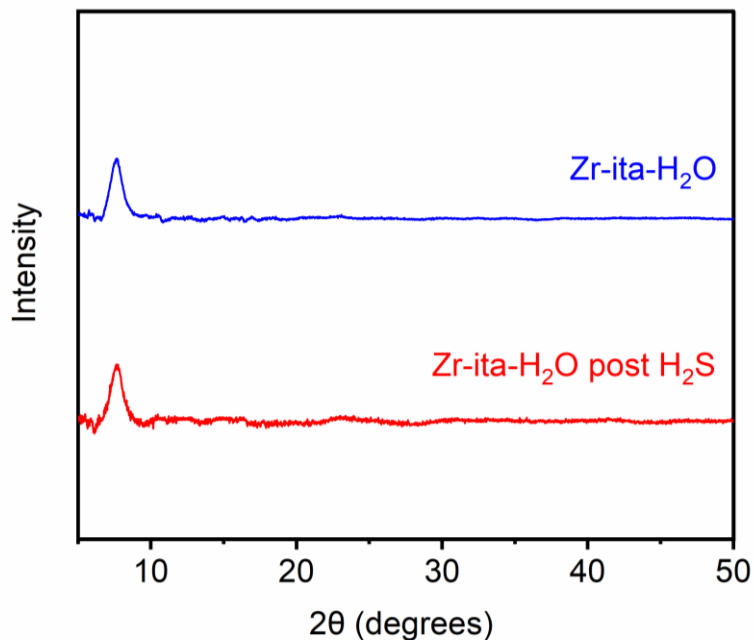


Figure S61. Powder X-ray diffraction patterns ($\lambda = 1.54 \text{ \AA}$) of Zr-ita-H₂O pre- and post-exposure to H₂S in THF.

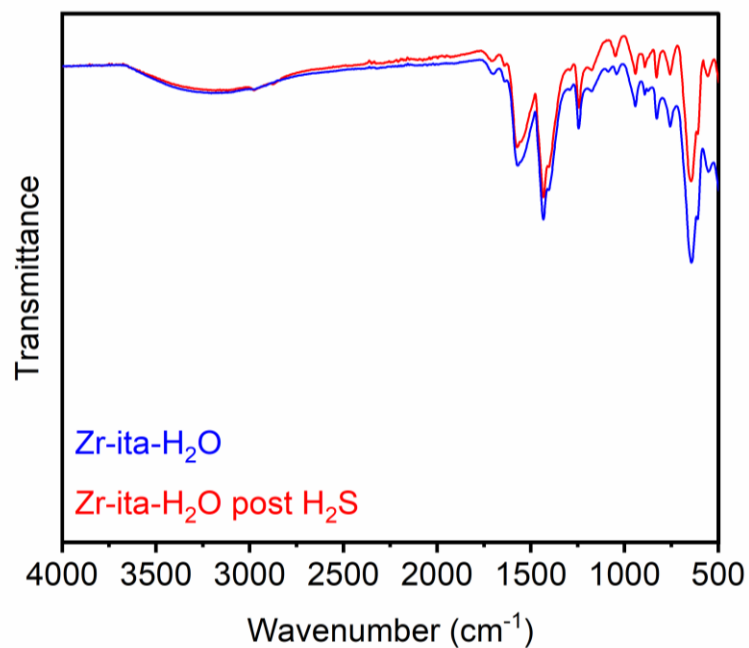


Figure S62. Infrared spectra of Zr-ita-H₂O pre- and post-exposure to H₂S in THF.

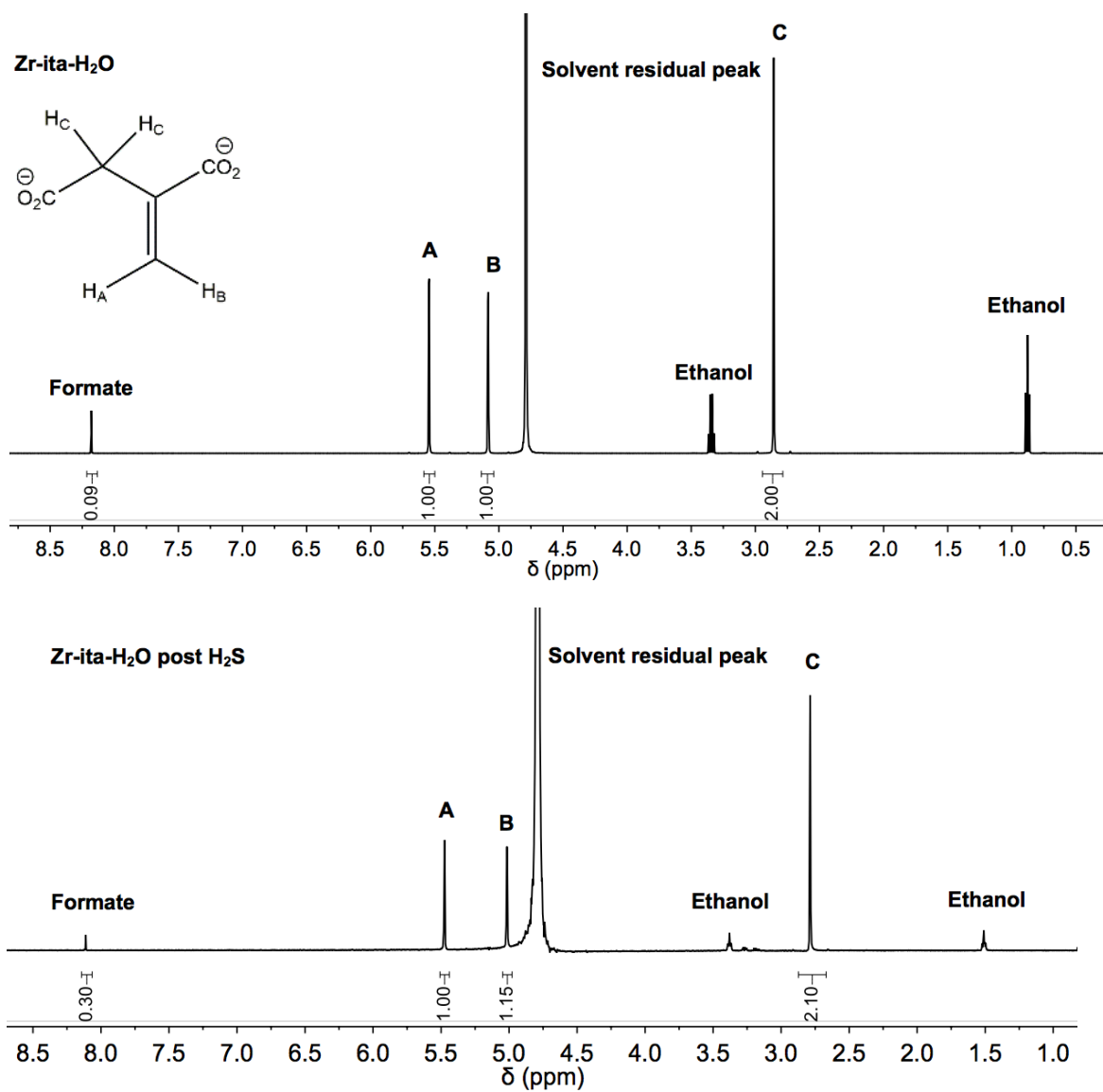


Figure S63. ¹H-NMR (500 MHz, D₂O) spectra of ethanol-solvated Zr-ita-H₂O pre- (top) and post-exposure (bottom) to H₂S in THF. Digested using a saturated solution of K₃PO₄ in D₂O. Peaks A, B, and C correspond to the itaconate linker. No significant changes to the linker were observed.

12. H₂S cycling of MOFs prepared under aqueous conditions.

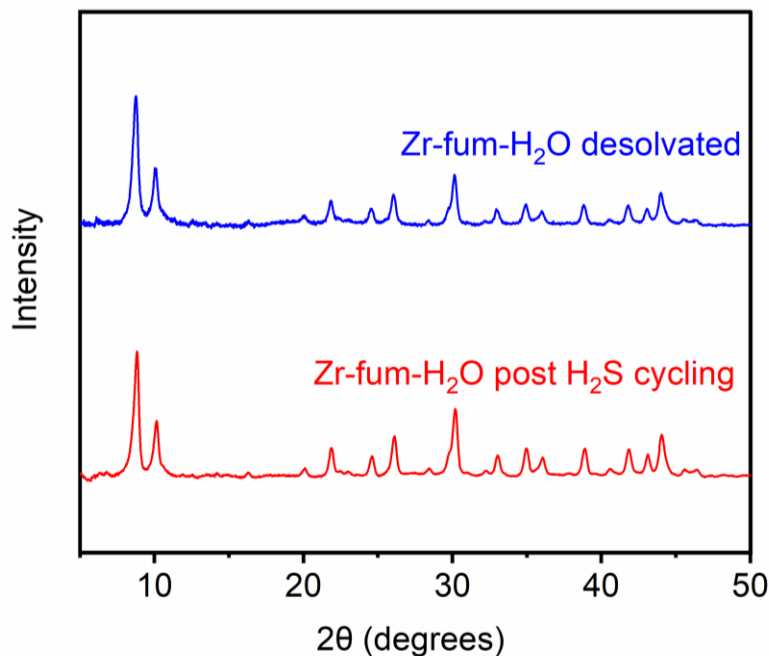


Figure S64. Powder X-ray diffraction patterns ($\lambda = 1.54 \text{ \AA}$) of desolvated Zr-fum-H₂O pre- and post-H₂S cycling. No significant reduction in crystallinity was observed after 10 H₂S adsorption/desorption cycles.

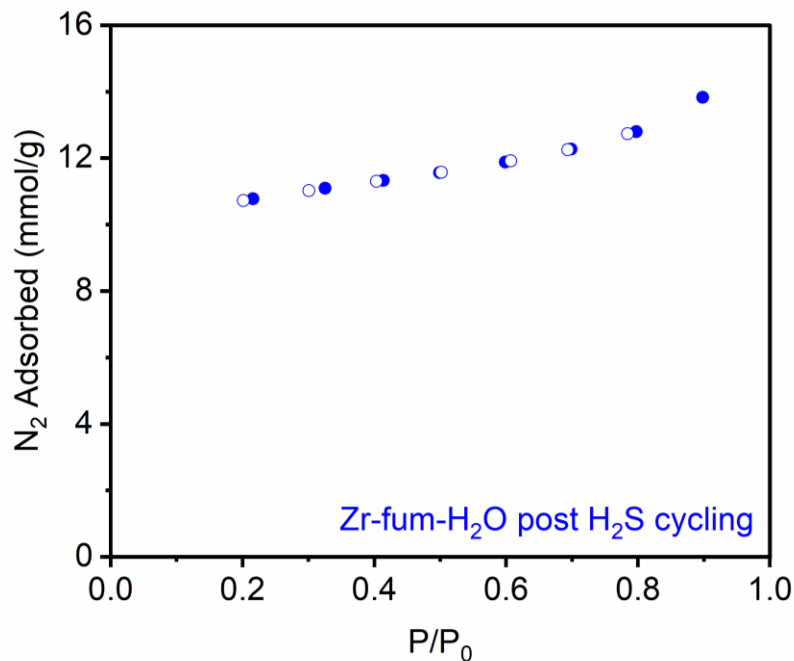


Figure S65. 77 K N₂ adsorption isotherm of Zr-fum-H₂O after 10 H₂S adsorption/desorption cycles at 30 °C. Desorption data are represented as open circles. Zr-fum-H₂O was regenerated after H₂S cycling at 100 °C for 24 h. The measured Langmuir surface area after H₂S cycling was $1229 \pm 23 \text{ m}^2/\text{g}$, indicating that this MOF retains porosity after H₂S adsorption/desorption cycling.

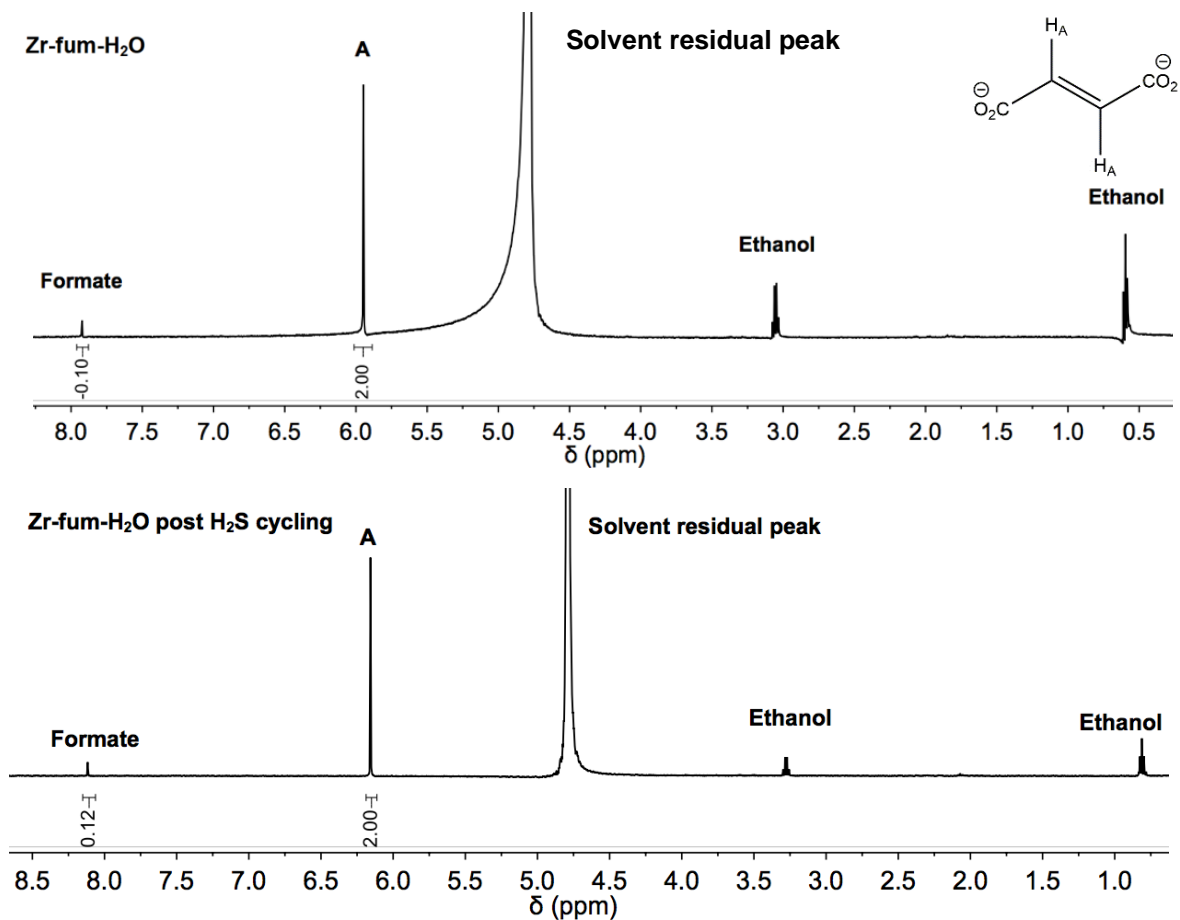


Figure S66. ¹H-NMR (500 MHz, D₂O) spectra of Zr-fum-H₂O pre- (top) and post- (bottom) H₂S cycling. Digested using a saturated solution of K₃PO₄ in D₂O. Peak A corresponds to the fumarate linker. No significant changes to the linker were observed upon cycling with H₂S.

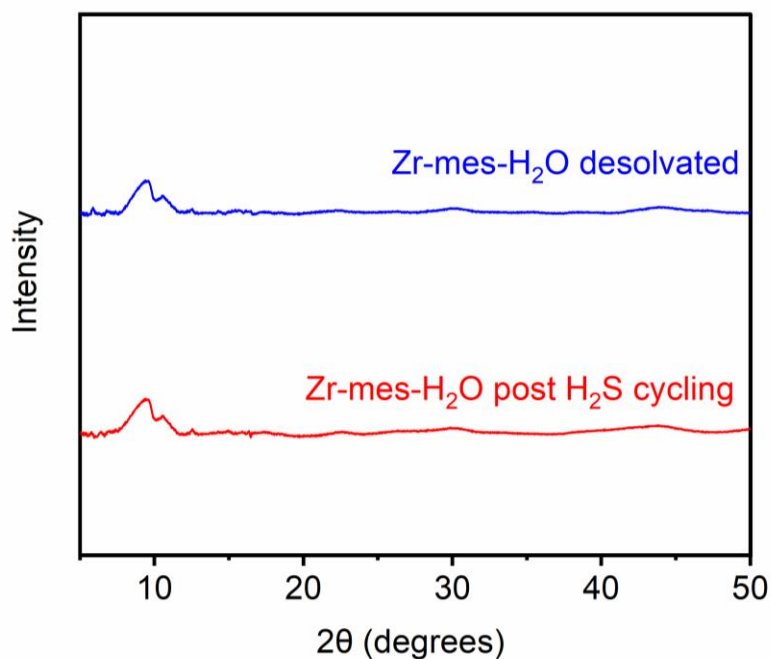


Figure S67. Powder X-ray diffraction patterns ($\lambda = 1.54 \text{ \AA}$) of desolvated Zr-mes-H₂O pre- and post- H₂S cycling.

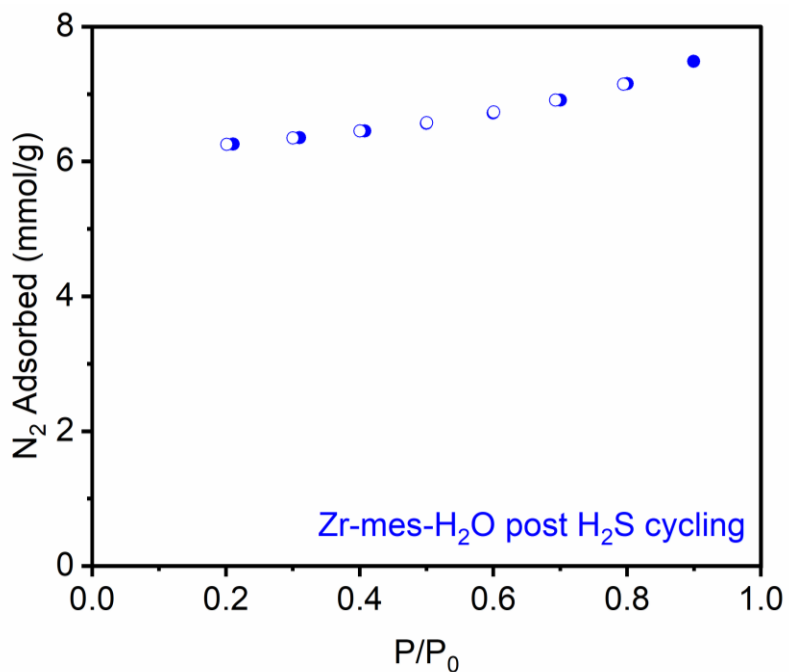


Figure S68. 77 K N₂ adsorption isotherm of Zr-mes-H₂O after 10 H₂S adsorption/desorption cycles at 30 °C. Desorption data are represented as open circles. Zr-mes-H₂O was regenerated after H₂S cycling at 100 °C for 24 h. The measured Langmuir surface area after H₂S cycling was $704 \pm 15 \text{ m}^2/\text{g}$, indicating that this MOF retains porosity after H₂S adsorption/desorption cycling.

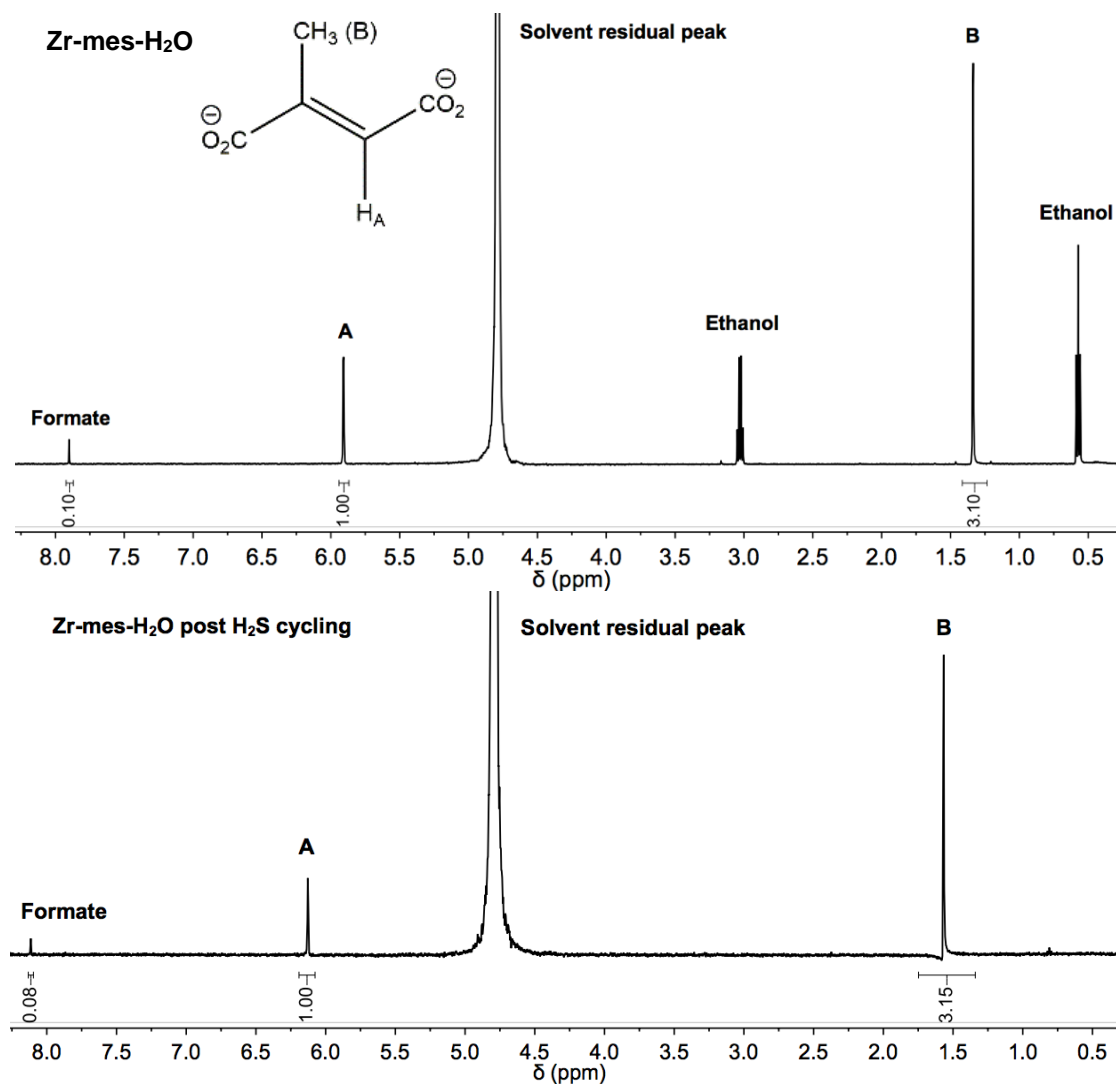


Figure S69. ¹H-NMR (500 MHz, D₂O) spectra of Zr-mes-H₂O pre- (top) and post- (bottom) H₂S cycling. Digested using a saturated solution of K₃PO₄ in D₂O. Peaks **A** and **B** correspond to the mesaconate linker. No significant changes to the linker were observed.

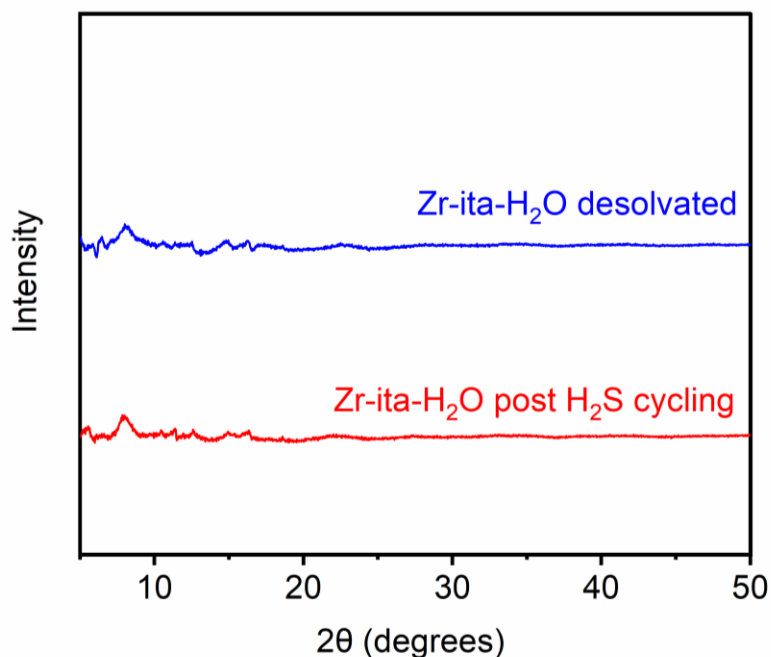


Figure S70. Powder X-ray diffraction patterns ($\lambda = 1.54 \text{ \AA}$) of desolvated Zr-ita-H₂O pre- and post- H₂S cycling.

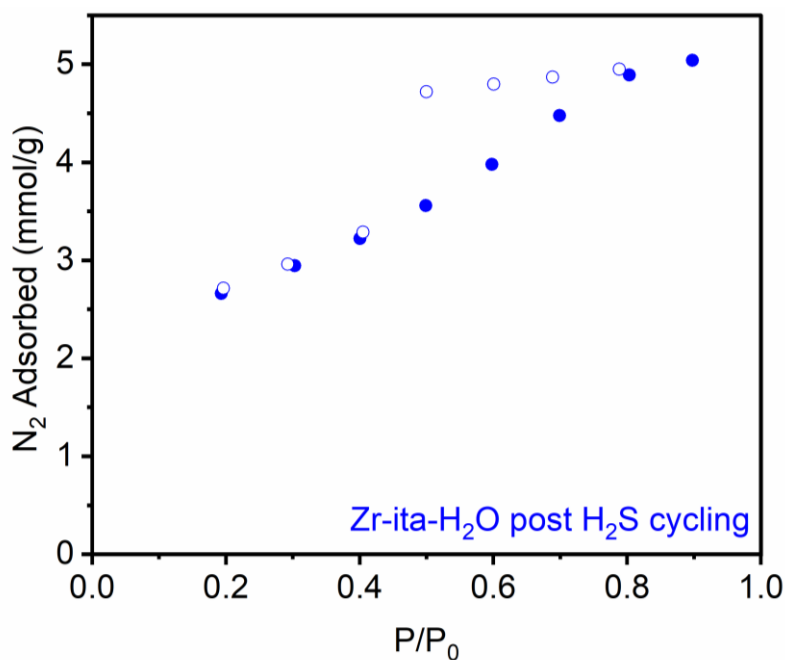


Figure S71. 77 K N₂ adsorption isotherm of Zr-ita-H₂O after 10 H₂S adsorption/desorption cycles at 30 °C. Desorption data are represented as open circles. Zr-ita-H₂O was regenerated after H₂S cycling at 100 °C for 24 h. The measured Langmuir surface area after H₂S cycling was $440 \pm 36 \text{ m}^2/\text{g}$, indicating that this MOF retains porosity after H₂S adsorption/desorption cycling.

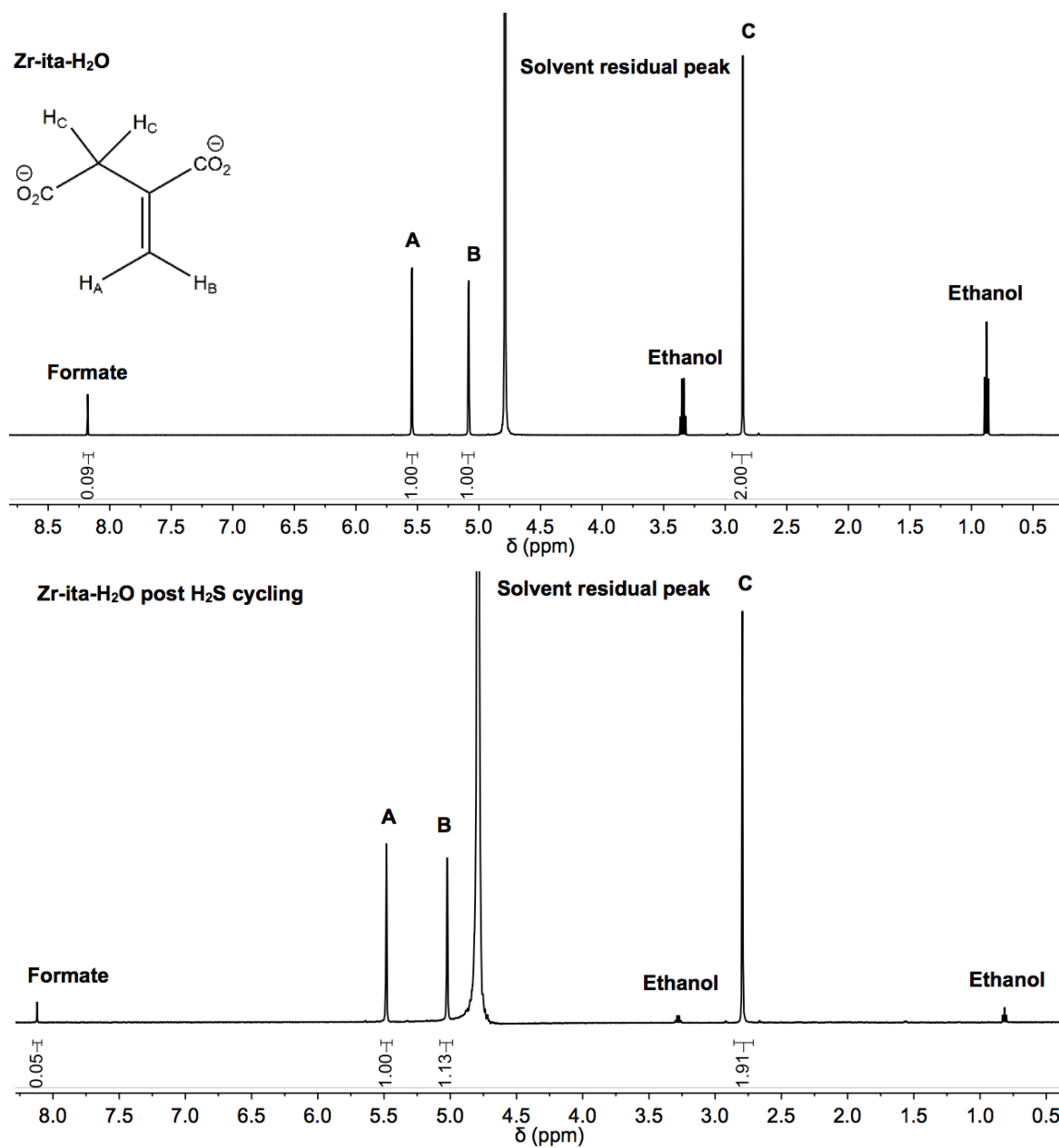


Figure S72. ¹H-NMR (500 MHz, D₂O) spectra of Zr-ita-H₂O pre- (top) and post- (bottom) H₂S cycling. Digested using a saturated solution of K₃PO₄ in D₂O. Peaks **A**, **B**, and **C** correspond to the itaconate linker. No significant changes to the linker were observed.

13. Delivery of H₂S under biologically relevant conditions.

Serum and DI water stabilities. A 5 mL scintillation vial was loaded with desolvated MOF (~50 mg) and either serum or DI water (3.0 mL) was added *via* syringe. The vial was capped, and the tube was left to stand for either 3 days (serum) or 10 days (DI water) at room temperature. The serum measurements were carried out using at Dulbecco's Modified Eagle's Medium (DMEM) supplemented with 10% fetal bovine serum (FBS), which is the standard medium used for all cell culture experiments in this work. The MOFs were collected by filtration and washed with deionized water. The solids were then characterized. Together, these results suggest that the MOFs would likely undergo slow degradation upon submersion in serum for extended periods of time, but they are stable enough for delivery of H₂S.

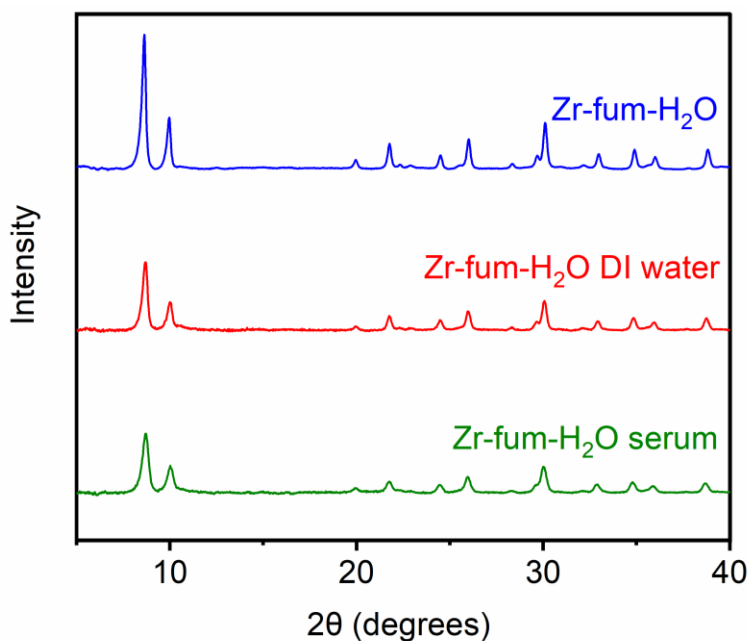


Figure S73. Powder X-ray diffraction patterns ($\lambda = 1.54 \text{ \AA}$) of Zr-fum-H₂O pre- and post-exposure to DI water (red) and serum (green, 10% FBS in DMEM). No significant loss in crystallinity was observed, although the peak broadening observed upon submersion in serum indicates partial dissolution of the MOF occurred under these conditions.

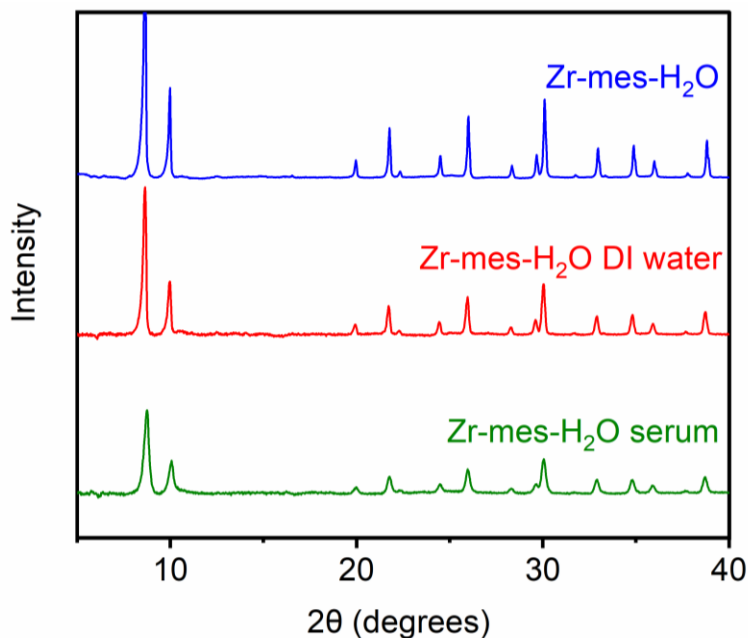


Figure S74. Powder X-ray diffraction patterns ($\lambda = 1.54 \text{ \AA}$) of Zr-mes-H₂O pre- and post-exposure to DI water (red) and serum (green, 10% FBS in DMEM). No significant loss in crystallinity was observed, although the peak broadening observed upon submersion in serum indicates partial dissolution of the MOF occurred under these conditions.

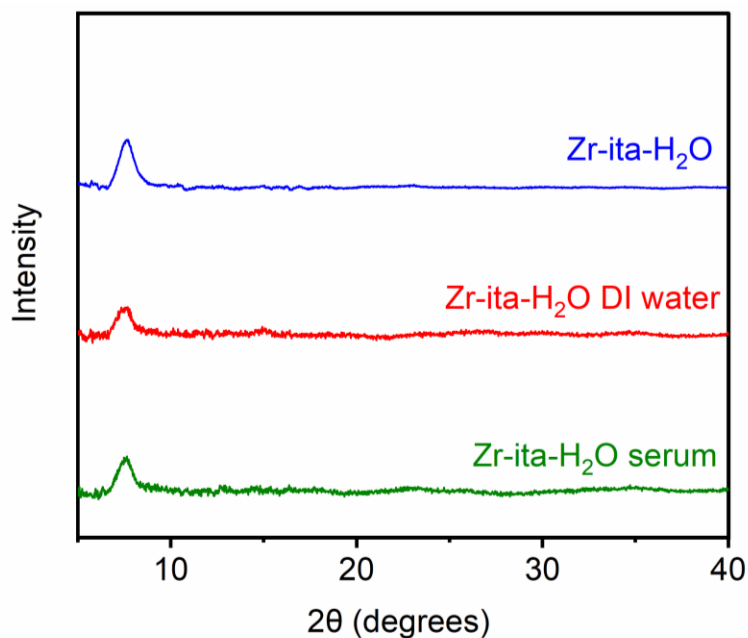
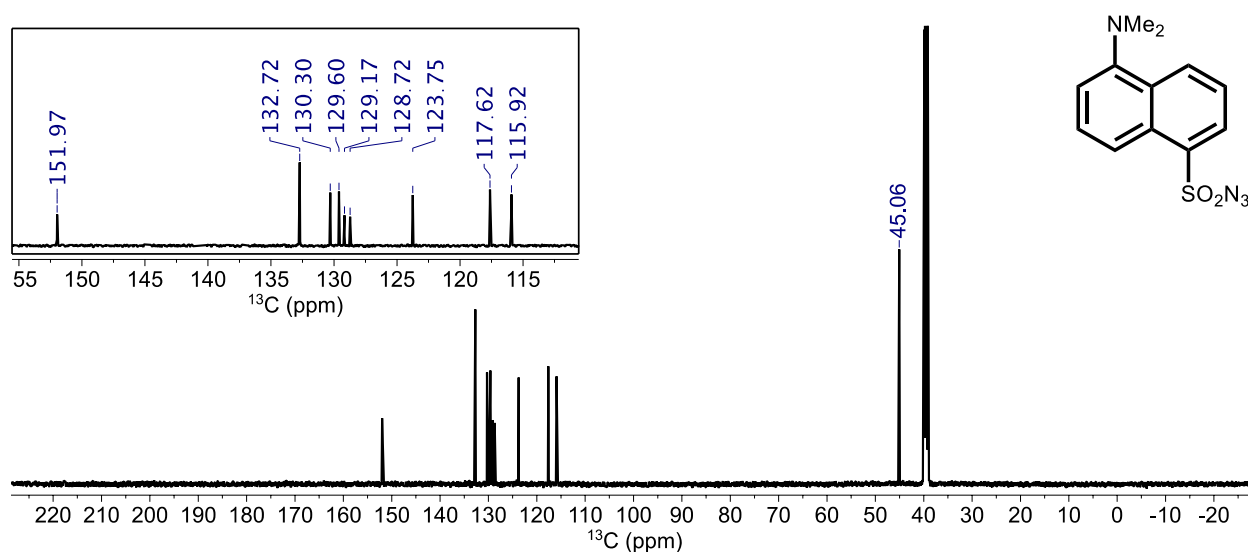
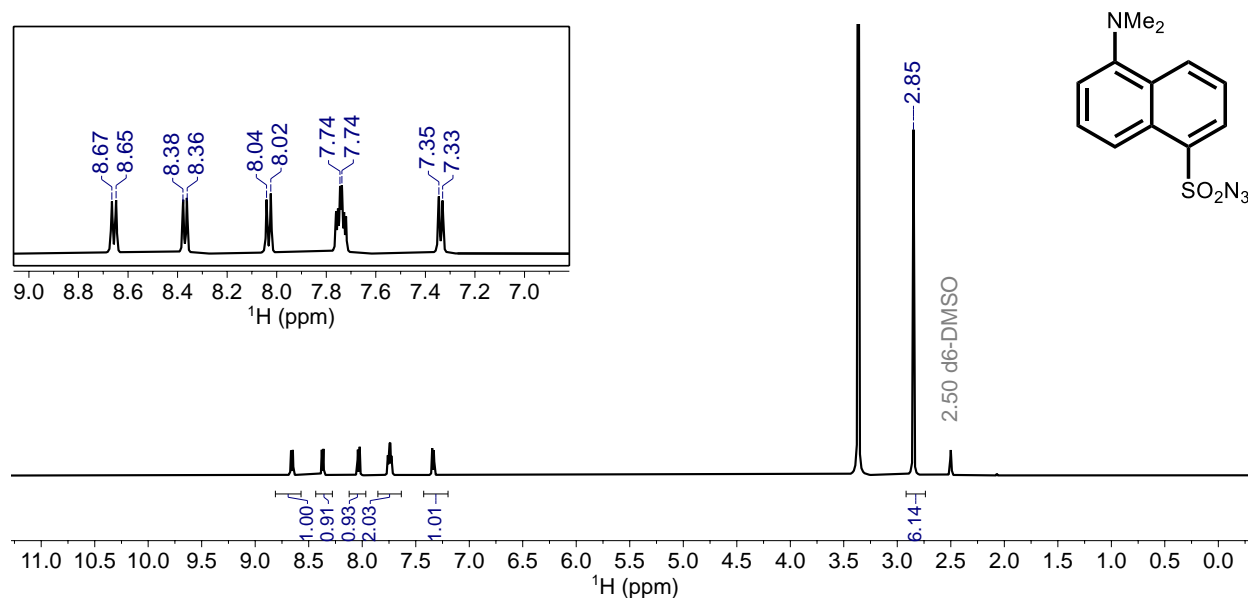


Figure S75. Powder X-ray diffraction patterns ($\lambda = 1.54 \text{ \AA}$) of Zr-ita-H₂O pre- and post-exposure to DI water (red) and serum (green, 10% FBS in DMEM). No significant loss in crystallinity was observed, although the peak broadening observed upon submersion in serum indicates partial dissolution of the MOF occurred under these conditions.

Synthesis of 1,5-dansyl azide (DNS-az). This compound was synthesized by a modified literature procedure.⁴ A solution of dansyl chloride (250 mg, 0.93 mmol) in ethanol (15 mL) was added dropwise to a rapidly stirred solution of sodium azide (100 mg, 1.54 mmol) in 50% aqueous ethanol (7 mL). The resulting yellow solution was stirred for 4 h, at which time the solvent was removed by rotary evaporation to yield the crude product as a yellow oil. The oil was purified by silica gel chromatography (2:1 hexanes/CH₂Cl₂). The pure fractions were pooled and evaporated to yield DNS-az as a bright yellow oil, which was dried under high vacuum overnight. Yield: 190 mg (73.9%). ¹H NMR (500 MHz, DMSO-*d*₆): δ 8.66 (d, *J* = 10 Hz, 1H), 8.37 (d, *J* = 10 Hz, 1H), 8.03 (d, *J* = 10 Hz, 1H), 7.74 (m, 2H), 7.34 (d, *J* = 10 Hz, 1H), 2.85 (s, 6H). ¹³C NMR (125 MHz, DMSO-*d*₆): δ 151.97, 132.72, 130.30, 129.60, 129.17, 128.72, 123.75, 117.62, 115.92, 45.06. These spectra are consistent with those reported in the literature.⁴

H₂S detection via fluorescence spectroscopy. The turn-on fluorescent probe 1,5-dansyl azide (DNS-az) was used to detect H₂S in solution. A known amount of desolvated Zr-ita-H₂O or Zr-fum-H₂O (50–100 mg) was weighed and activated for 48 h at 100 °C under vacuum (<10 μ bar). The MOF was then dosed with ~1 bar of H₂S at 30 °C and allowed to equilibrate until <0.01% change in the H₂S pressure occurred over a 45 s interval (approximately 3–4 h in each case). The exact amount of H₂S adsorbed was recorded. At the time of the experiment, the tube with MOF was purged with N₂ for 90 s to remove gaseous H₂S before the sample was poured into a stirred solution of phosphate buffered saline (PBS; pH 7.4) at a typical concentration of ~1 mg MOF/mL of PBS. Assuming a capacity of 4 mmol/g of H₂S in Zr-fum-H₂O, this corresponds to a maximum concentration of 4 mM for H₂S in the PBS solution, if all of the H₂S was released by the MOF into solution. A control experiment in which a tube lacking MOF was dosed with H₂S, purged with N₂ for 90 s, and then “poured” into PBS yielded no detectable amounts of H₂S in solution, confirming that this purging procedure is sufficient to remove gaseous H₂S from the tube. At 30 second intervals, 300 μ L aliquots of the suspension (corresponding to a maximum amount of 1.2 μ mol of H₂S) was removed (taking care not to remove any solids; a syringe filter was used in the case of Zr-fum-H₂O) and added to a freshly-prepared solution of DNS-az (25 μ mol) in CH₃CN (1 mL, final concentration of 25 mM). The large excess of DNS-az (25 μ mol) compared to H₂S (maximum of 1.2 μ mol for Zr-fum-H₂O) in the aliquot guarantees that the DNS-az probe should not be saturated during the experiment. The solution was allowed to incubate at 23 °C for 5 min before

the fluorescence of the probe was measured at 520 nm (with excitation at 340 nm). Due to unavoidable loss of gaseous H₂S to air, this assay cannot be used to reliably quantify the amount of H₂S released into solution. However, the kinetics of H₂S release were found to be relatively reproducible between samples.



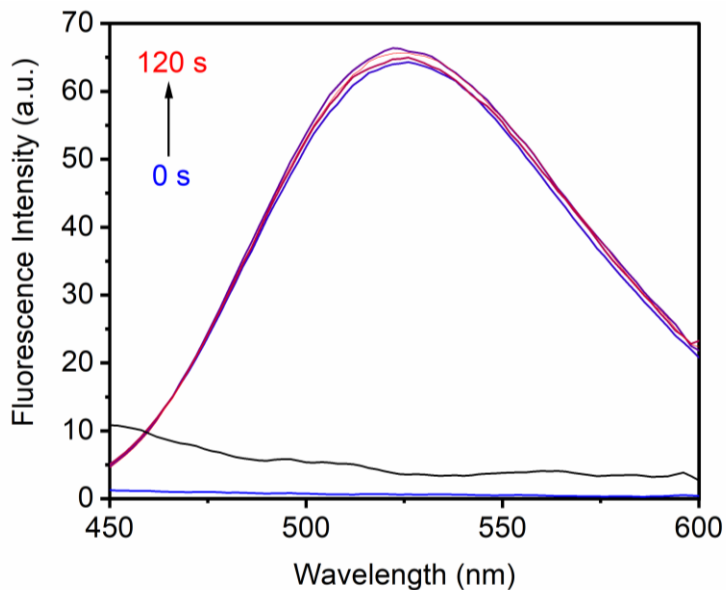
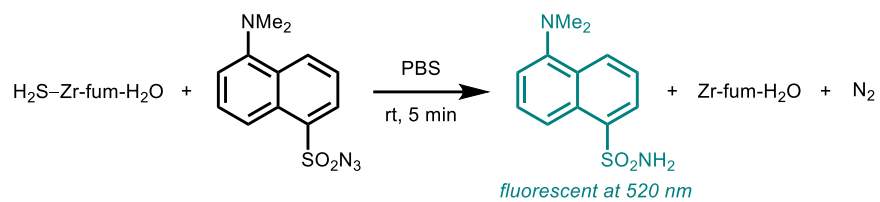


Figure S78. Fluorescence data of a second trial for H_2S release from $\text{Zr-fum-H}_2\text{O}$ in PBS at $23\text{ }^\circ\text{C}$ as detected by turn-on fluorescence upon reaction with 1,5-dansyl azide (DNS-az) to corroborate the results shown in Figure 9 of the main text. The fluorescence of the probe was measured at 520 nm (with excitation at 340 nm). The black line corresponds to a control experiment in which no MOF was added to the PBS. The data were smoothed by adjacent-averaging (15 points).

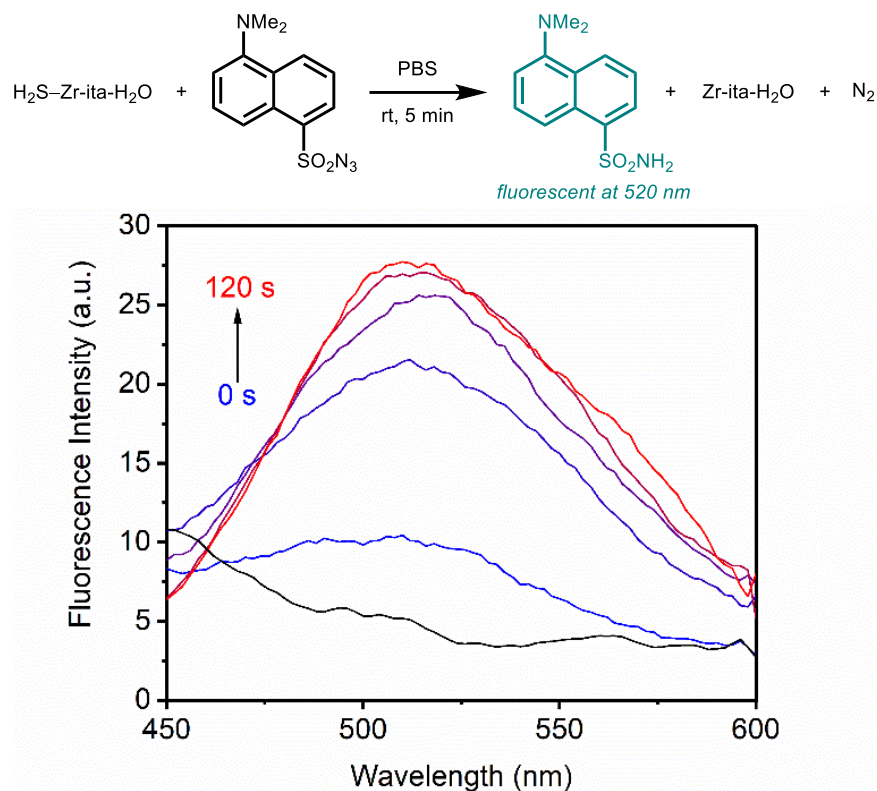


Figure S79. Fluorescence data of a second trial for H₂S release from Zr-ita-H₂O in PBS at 23 °C as detected by turn-on fluorescence upon reaction with 1,5-dansyl azide (DNS-az) to corroborate the results shown in Figure 9 of the main text. The fluorescence of the probe was measured at 520 nm (with excitation at 340 nm). The black line corresponds to a control experiment in which no MOF was added to the PBS. The data were smoothed by adjacent-averaging (15 points).

Cell lines and culture conditions. HeLa and H9c2 cells were obtained from American Type Culture Collection (ATCC, Washington D.C.) and cultured as adherent monolayers in a humidified 5% CO₂ atmosphere at 37 °C in DMEM supplemented with 10% FBS. Cells were checked for contamination monthly using the Plasmotest mycoplasma detection kit from InvivoGen (San Diego, CA).

Cytotoxicity assay. HeLa or H9c2 cells were seeded in 96-well plates with ~2000 cells/well and allowed to reattach overnight. The following day, the culture media was removed, and cells were treated with suspensions containing varying concentrations of the desired MOF in in DMEM supplemented with 10% FBS and incubated for 72 h at 37 °C. Following treatment, the cells were incubated in DMEM containing 1 mg/mL (4,5-dimethylthiazol-2-yl)-2,5-diophenyltetrazolium bromide (MTT) without FBS for 3 hours. Following incubation, the media was removed, and the purple formazan crystals were solubilized using 150 μL of an 8/1

DMSO/glycine buffer (pH 10) mixture. The absorbance at 570 nm of each well was measured using a BioTek Synergy HT plate reader. Results are reported as the average cell viability of 6 wells/concentration compared to untreated cells from three independent trials, with the standard deviation (SD) reported as the error (\pm SD).

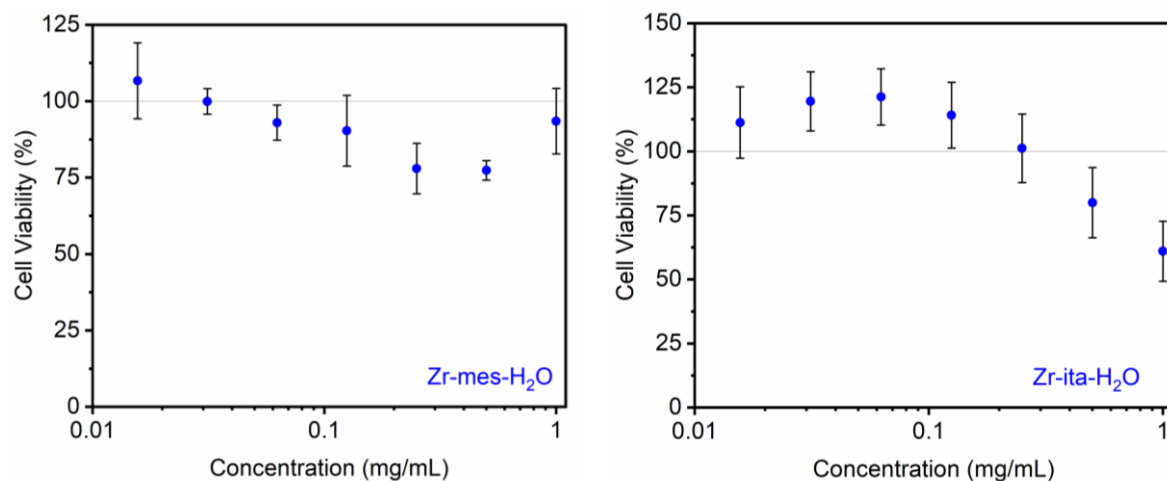


Figure S80. Viability of HeLa cells upon exposure to suspensions of activated Zr-mes-H₂O (left panel) and Zr-ita-H₂O (right panel) at a range of concentrations in DMEM supplemented with 10% FBS for 72 h at 37 °C. Viabilities were determined by the method described above.

Cellular hypoxia-reoxygenation model of ischemia-reperfusion injury. On the day before the experiment, H9c2 rat cardiomyoblast cells were seeded in a 96 well plate at a density of 8000 cells/well and incubated at 37 °C overnight. To initiate the experiment, the culture media was removed, and the cells were washed with 100 μ L of PBS. The assay was initiated by placing the cells in 200 μ L of modified Gey's balanced salt solution (GBSS) containing 120 mM NaCl, 5 mM KCl, 1.5 mM CaCl₂, 0.28 mM MgSO₄, 1 mM MgCl₂, 0.840 mM Na₂HPO₄, 0.220 mM KH₂PO₄, and 27 mM NaHCO₃. The plates were then placed in a hypoxia chamber and flushed with 5% CO₂ in N₂ for 10 minutes. The chamber was sealed, and the cells were incubated under hypoxic conditions for 2.5 h at 37 °C. Following hypoxia, the cells were incubated under normoxic conditions in DMEM containing 10 % FBS and the H₂S-loaded Zr-fum-H₂O at a concentration of 0.05 mg/mL for 24 h prior to measuring the viability using the MTT assay as described above. Viability is reported relative to control cells that were incubated under normal culture conditions throughout the experiment. Another set of control cells were incubated with the MOF without previous incubation under hypoxic conditions. Results are reported as the average viability from

12 wells of a 96 well plate from three independent trials, with the standard deviation (SD) reported as the error (\pm SD) (ns = not significant, *** $p < 0.005$).

H₂S Imaging in HeLa cells with WSP5. Approximately 1×10^5 HeLa cells were seeded in 35 mm glass-bottomed dishes (MatTek Life Sciences, Ashland, MA) and incubated overnight at 37 °C. The following day, the media was removed and the cells were treated with DMEM without FBS containing 1 mM cetyl trimethyl ammonium bromide (CTAB) and 15 μ M WSP5 (Cayman Chemicals, Ann Arbor, MI; WSP = Washington State Probe) and incubated for 30 min at 37 °C in the dark.⁵ The dye-containing media was removed, and the cell layer was washed with PBS (2×1 mL) before treatment with either 0.05 mg/mL of H₂S-loaded Zr-fum-H₂O or 200 μ M Na₂S in DMEM without FBS. The cells were then incubated for 1 h at 37 °C. At the time of imaging, the media was removed, and the cells were washed with 1 mL PBS. Fluorescence images were collected in PBS using a Zeiss LSM710 confocal fluorescence microscope fitted with a 10 \times water objective with an excitation wavelength of 514 nm and an emission window of 535–657 nm. Images were analyzed and quantified using ImageJ (NIH) and the corrected total cellular fluorescence (CTCF) was calculated using the following formula:

$$\text{CTCF} = \text{Integrated density} - (\text{area of cell} \times \text{mean fluorescence of the background})$$

The average of 8 individual cells was used to determine the average CTCF for each replicate. Results are reported as the average of three biological replicates.

Qualitative monitoring of H₂S release via lead test strips. The formation of lead sulfide on lead chloride-soaked filter paper was used to visually confirm H₂S release from Zr-mes-H₂O, Zr-fum-H₂O, and Zr-ita-H₂O under ambient conditions. Filter paper cut into thin strips was dipped into a 1 wt% aqueous lead (II) chloride solution and dried for ten minutes. Once dried, the strips were added to a 25 mL scintillation vial containing \sim 100 mg of H₂S-loaded MOF prepared under the same conditions as described above. Black or orange lead sulfide precipitation on the strips resulted immediately upon contact with the MOF and/or vial glass. The vials were capped, and the old strips removed and replaced once per day until they no longer turned black or orange. Images were taken of the vials each day. As a control, the same assay was used to monitor the release of H₂S from a similar amount of Na₂S \cdot 9H₂O and NaSH. Owing to the rapid hydrolysis of both salts (complete degradation/dissolution within 5 h), the lead strip was not changed through the duration of the assay.

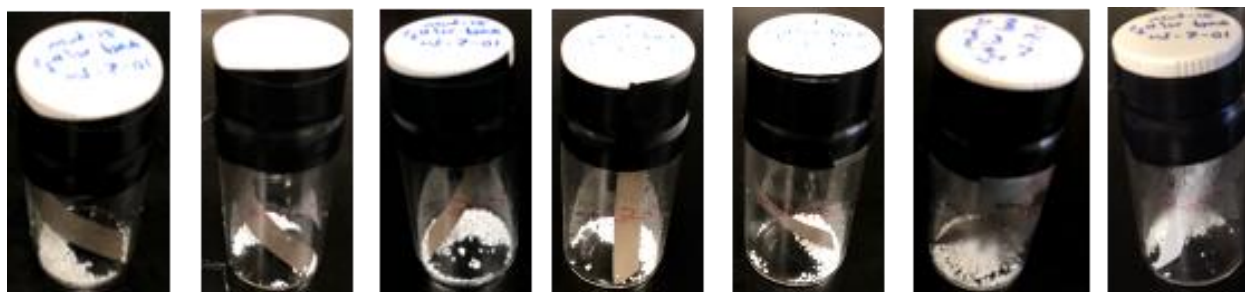


Figure S81. Progression of H_2S release into ambient air from H_2S -loaded Zr-fum- H_2O over the course of 7 days. Each image was taken after replacing the previous lead test strip with a new one at 24-hour intervals. The strip turned black for the first 6 days followed by no color change on the 7th day, confirming that this MOF releases H_2S slowly over the course of 6 days in air.



Figure S82. Progression of H_2S release into ambient air from H_2S -loaded Zr-mes- H_2O over the course of 5 days. Each image was taken after replacing the previous lead test strip with a new one at 24-hour intervals. The strip turned black for the first 4 days followed by no color change on the 5th day, confirming that this MOF releases H_2S slowly over the course of 4 days in air.



Figure S83. Progression of H_2S release into ambient air from H_2S -loaded Zr-ita- H_2O over the course of 6 days. Each image was taken after replacing the previous lead test strip with a new one at 24-hour intervals. The strip turned black for the first 5 days followed by no color change on the 6th day, confirming that this MOF releases H_2S slowly over the course of 5 days.



Figure S84. Progression of H₂S release into ambient air from Na₂S·9H₂O and NaSH over the course of 5 h. Each image was taken at 1 h intervals, and the lead strip was not changed throughout the duration of the assay. The rapid hydrolysis of both salts in humid air (neither solid remained after 5 h) demonstrates their instability compared to H₂S-loaded Zr-fum, Zr-mes, and Zr-ita.

14. Computational and structural details.

To elucidate the H₂O and H₂S adsorption mechanisms, we performed first-principles density functional theory (DFT) calculations using a plane-wave basis and projector augmented-wave (PAW)^{6,7} pseudopotentials with the Vienna ab-initio Simulation Package (VASP) code.⁸⁻¹¹ To include the effect of the van der Waals (vdW) dispersive interactions on binding energies, we performed structural relaxations with Grimme's D3 correction as implemented in VASP.¹² For all calculations, we used (i) a Γ -point sampling of the Brillouin zone and (ii) a 600 eV plane-wave cutoff energy. We explicitly treated twelve valence electrons for Zr ($4s^2 4p^6 4d^2 5s^2$), six for S ($3s^2 3p^4$), six for O ($2s^2 2p^4$), four for C ($2s^2 2p^2$), and one for H ($1s^1$). All structural relaxations were performed with a Gaussian smearing of 0.05 eV.^{13,14} The ions were relaxed until the Hellmann-Feynman forces were less than $0.01 \text{ eV}\text{\AA}^{-1}$. Using above input parameters, we relaxed both internal coordinates and volumes.

To compute the H₂O and H₂S binding energies, we optimized MOFs prior to H₂O and H₂S adsorptions (E_{MOF}), interacting with H₂O and H₂S in the gas phase ($E_{\text{H}_2\text{O}|\text{H}_2\text{S}}$) within a $20 \text{ \AA} \times 20 \text{ \AA} \times 20 \text{ \AA}$ cubic supercell, and MOF with adsorbed H₂O and H₂S molecules ($E_{\text{H}_2\text{O}|\text{H}_2\text{S}-\text{MOF}}$) using a rigid MOF. The binding energies (E_{B}) were obtained via the difference

$$E_{\text{B}} = E_{\text{H}_2\text{O}|\text{H}_2\text{S}-\text{MOF}} - (E_{\text{MOF}} + E_{\text{H}_2\text{O}|\text{H}_2\text{S}}).$$

The idealized Zr₆O₄(OH)₄(RCO₂)₆ clusters of Zr-fum, Zr-mes, and Zr-ita contain a mixture of four OH⁻ and four O²⁻ sites to achieve charge neutrality. Initially, we computationally generated these structures without explicitly treating the protons on the Zr₆O₈ clusters for simplicity. The computationally-generated structures of Zr-fum, Zr-mes, and Zr-ita in this manner are included in Figure S91. The calculated structure of Zr-fum shows excellent agreement with the previously reported single-crystal X-ray diffraction structure of MOF-801 (Figure S86).

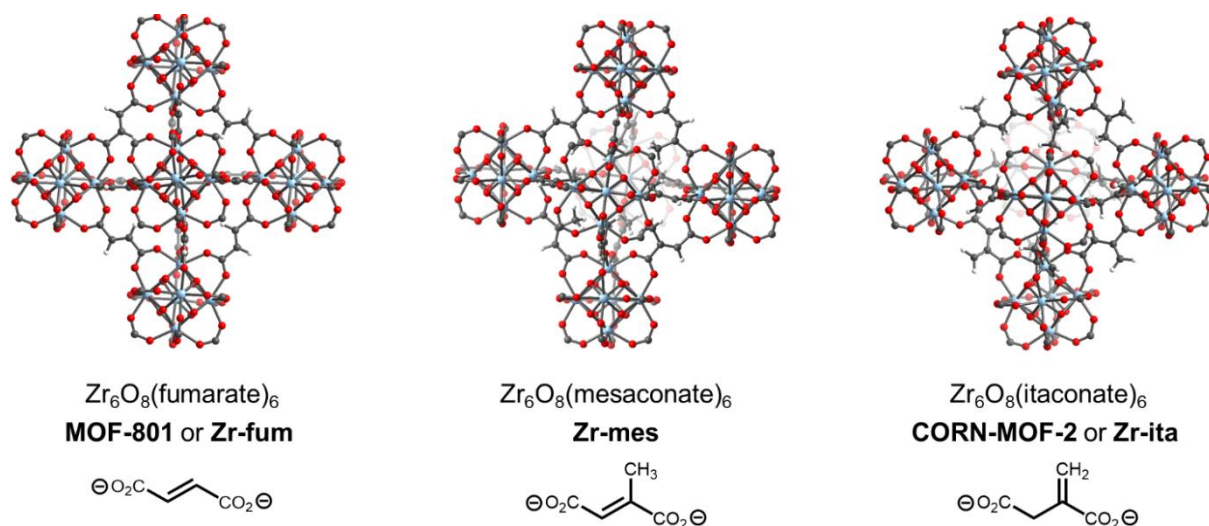


Figure S85. DFT-calculated structures of Zr-fum, Zr-mes, and Zr-ita generated by not explicitly including protons on the Zr_6O_8 clusters. Gray, white, red, and pale blue correspond to carbon, hydrogen, oxygen, and zirconium, respectively.

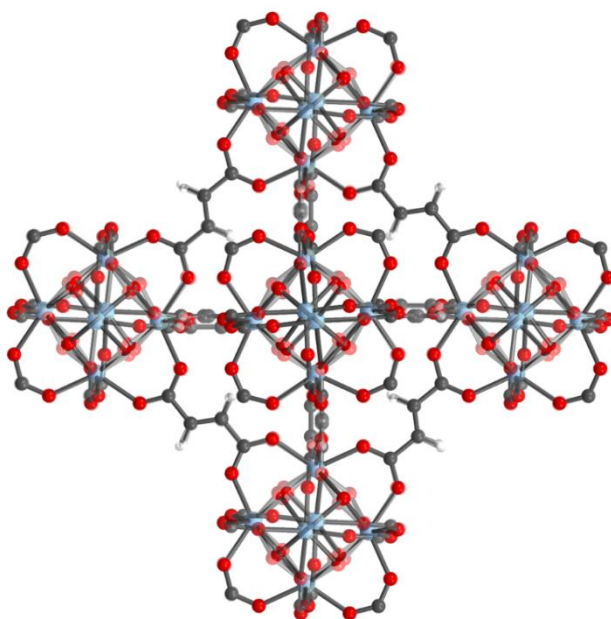


Figure S86. Overlay of the DFT-calculated structure of $\text{Zr}_6\text{O}_4(\text{OH})_4(\text{fumarate})_6$ and the previously reported single-crystal X-ray diffraction structure of MOF-801,¹ confirming the excellent overlap of these two structures. Gray, white, red, and pale blue correspond to carbon, hydrogen, oxygen, and zirconium, respectively.

These structures were then utilized to predict the preferred binding orientation of H₂O within these three MOFs (Figure S87). These computational structures show good agreement with those presented in the main text for structures in which the protons on the Zr₆O₄(OH)₄ clusters were explicitly treated (Figure 7). In addition, the structure of H₂O bound within the tetrahedral cavities of Zr-fum is in agreement with the neutron diffraction structure reported in the literature.¹

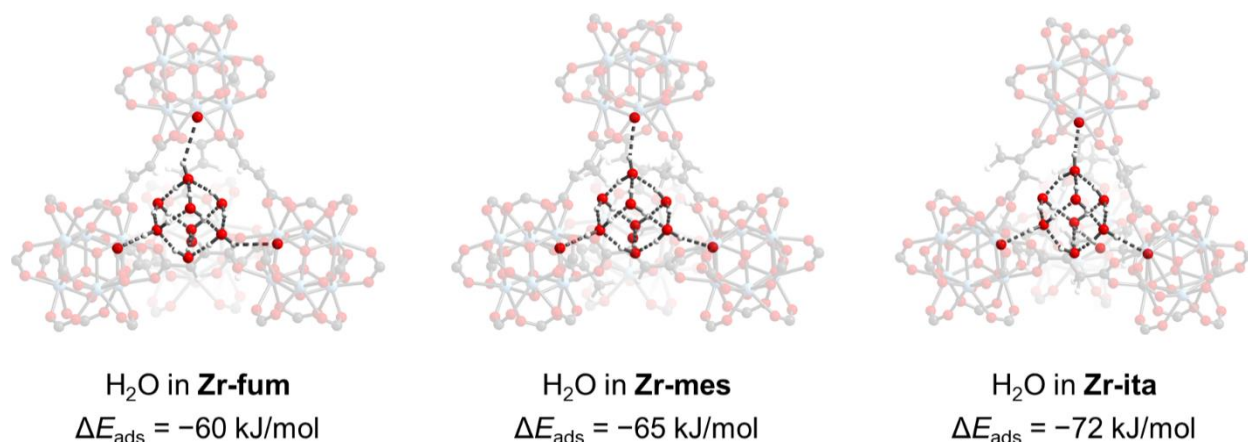


Figure S87. DFT-calculated structures of water bound within Zr-fum, Zr-mes, and Zr-ita generated by not explicitly including protons on the Zr₆O₈ clusters. Gray, white, red, and pale blue correspond to carbon, hydrogen, oxygen, and zirconium, respectively.

Although these simplified structures were sufficient to provide insight into the structures of these three MOFs, we encountered computational challenges when attempting to predict the preferred binding mode of H₂S within these MOFs. Specifically, S–S bond formation and loss of H₂ was found to be preferable given the presence of uncompensated negative charges on the Zr₆O₈ clusters. Therefore, the computational analysis was repeated while explicitly treating these protons on the Zr₆O₄(OH)₄ clusters. We include this discussion to highlight the importance of explicitly treating these protons to achieve charge neutrality on the MOF nodes, which can have a significant impact on computational outcomes.

The optimized structures of Zr-fum, Zr-mes, and Zr-ita with appropriately substituted Zr₆ clusters are included in Figure 1 of the main text. Space-filling models of these structures are included in Figure S88 for comparison.

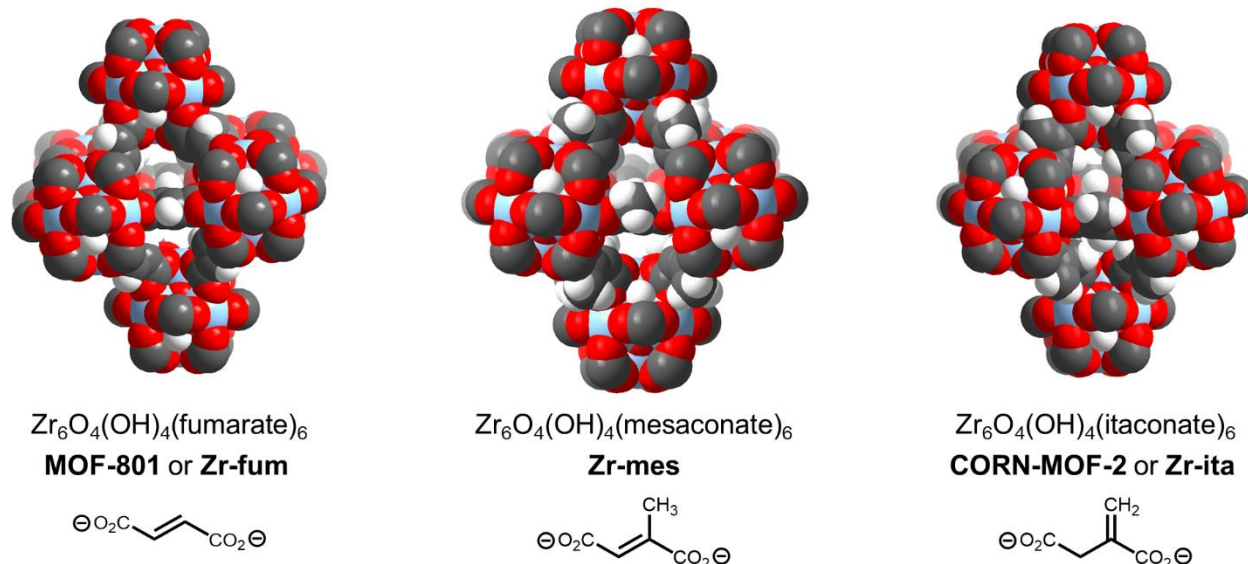


Figure S88. DFT-calculated space-filling models of Zr-fum, Zr-mes, and Zr-ita generated by explicitly including protons on the $\text{Zr}_6\text{O}_4(\text{OH})_4$ clusters. Gray, white, red, and pale blue correspond to carbon, hydrogen, oxygen, and zirconium, respectively.

The DFT-calculated structures for H_2O and H_2S adsorption in Zr-fum, Zr-mes, and Zr-ita are included in Figure 7 of the main text. Space-filling models of these structures are included in Figures S89–S90 for comparison.

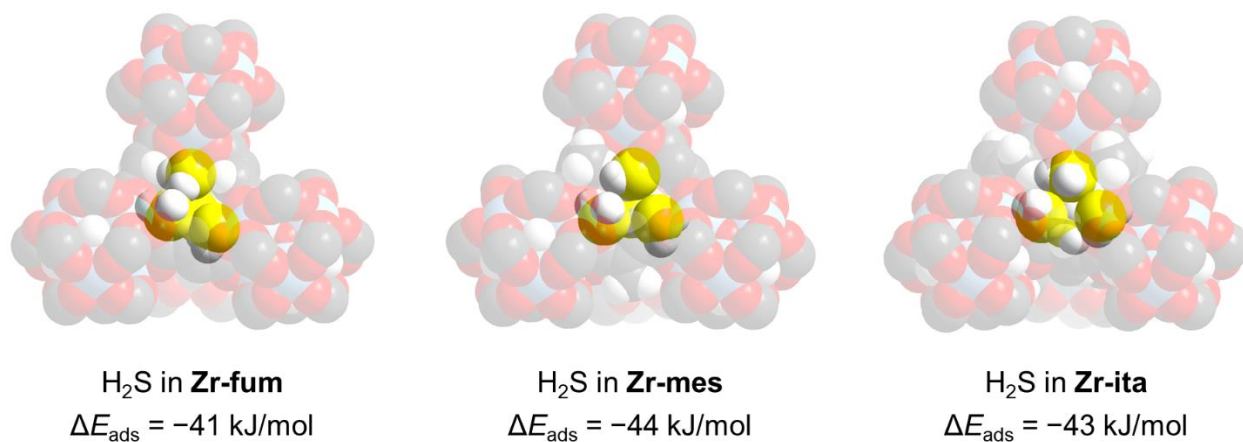


Figure S89. DFT-calculated space-filling models of hydrogen sulfide adsorbed in Zr-fum, Zr-mes, and Zr-ita. Gray, white, red, and pale blue correspond to carbon, hydrogen, oxygen, and zirconium, respectively.

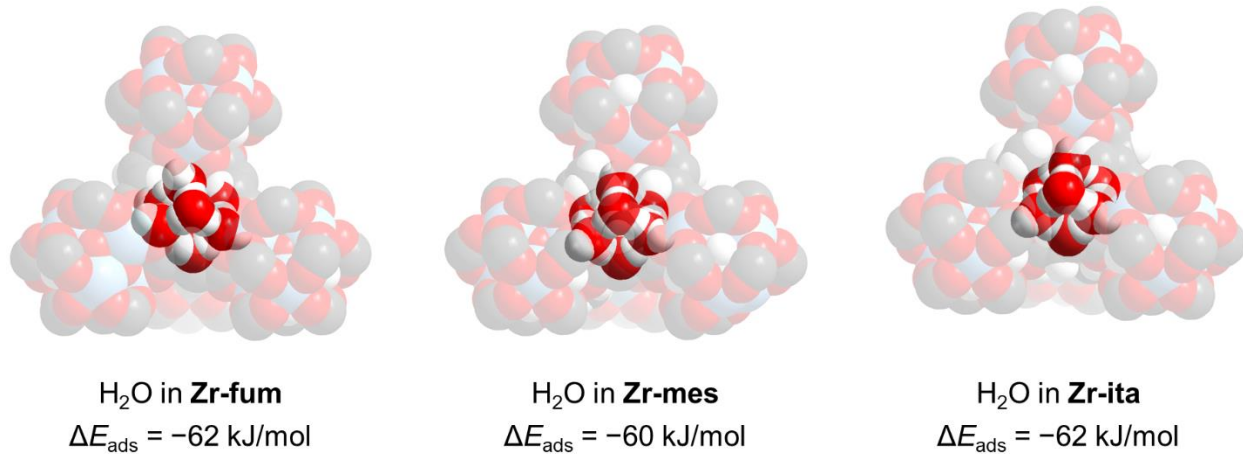


Figure S90. DFT-calculated space-filling models of water adsorbed in Zr-fum, Zr-mes, and Zr-ita. Gray, white, red, and pale blue correspond to carbon, hydrogen, oxygen, and zirconium, respectively.

15. H₂S and aqueous stability studies with Zn-MOF-74.

Preparation of Zn-MOF-74. This procedure is adapted from the literature.¹⁵ A 350 mL screw-cap high pressure reaction vessel equipped with a stir bar was charged with Zn(NO₃)₂·6H₂O (2.23 g, 7.50 mmol, 3.00 eq.), H₄dobdc (495 mg, 2.50 mmol, 1.00 eq.), fresh DMF (125 mL), and ethanol (125 mL). The mixture was sonicated until all of the solids dissolved. The reaction mixture was vigorously sparged with N₂ for 1 h. The reaction vessel was sealed, and the reaction mixture was allowed to stir slowly at 120 °C for 14 h, resulting in precipitation of a yellow powder from solution. The reaction mixture was cooled to room temperature and filtered. The collected solid was quickly transferred to a 500 mL Pyrex jar filled with DMF (250 mL). The jar was placed in an oven that had been pre-heated to 120 °C and left to stand for 24 h, after which time the non-homogeneous mixture was filtered. The collected solid was returned to the jar with fresh DMF (250 mL) and returned to an oven that had been pre-heated to 120 °C. This soaking process was repeated two more times. The mixture was then filtered and transferred to a 500 mL Pyrex jar filled with methanol (250 mL), and the jar was placed in an oven that had been pre-heated to 60 °C and left to stand 24 h, after which time the non-homogeneous mixture was filtered. The collected solid was returned to the jar with fresh methanol (250 mL) and returned to an oven that had been pre-heated to 60 °C. This soaking process was repeated two more times. The mixture was filtered a final time, and the collected solid was quickly transferred to a Schlenk flask under N₂. The material was activated under flowing N₂ at 180 °C for 24 h, and then by heating under high vacuum at 180 °C for 24 h.

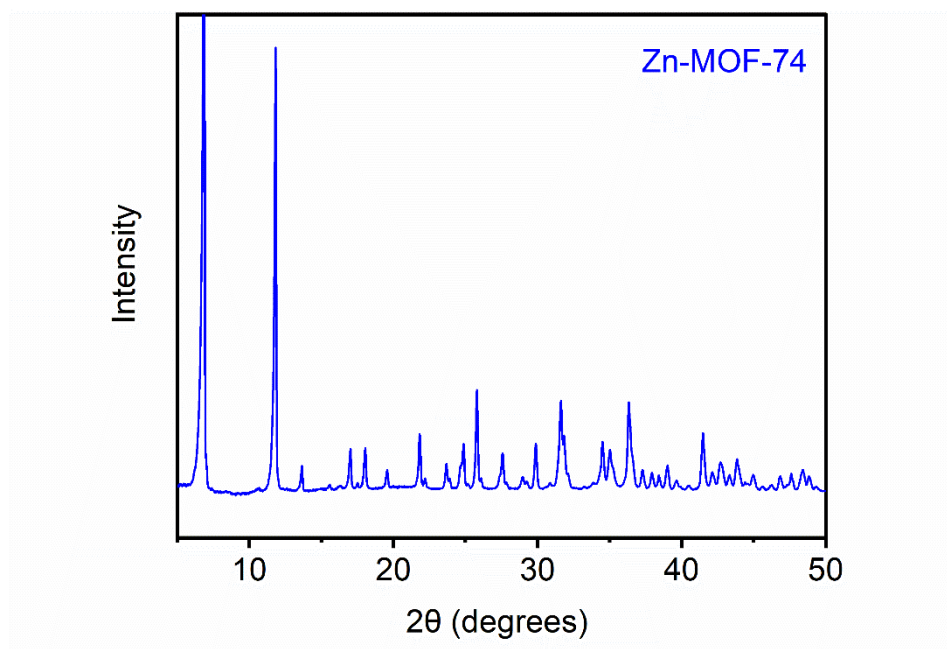


Figure S91. Powder X-ray diffraction pattern ($\lambda = 1.54 \text{ \AA}$) of desolvated Zn-MOF-74.

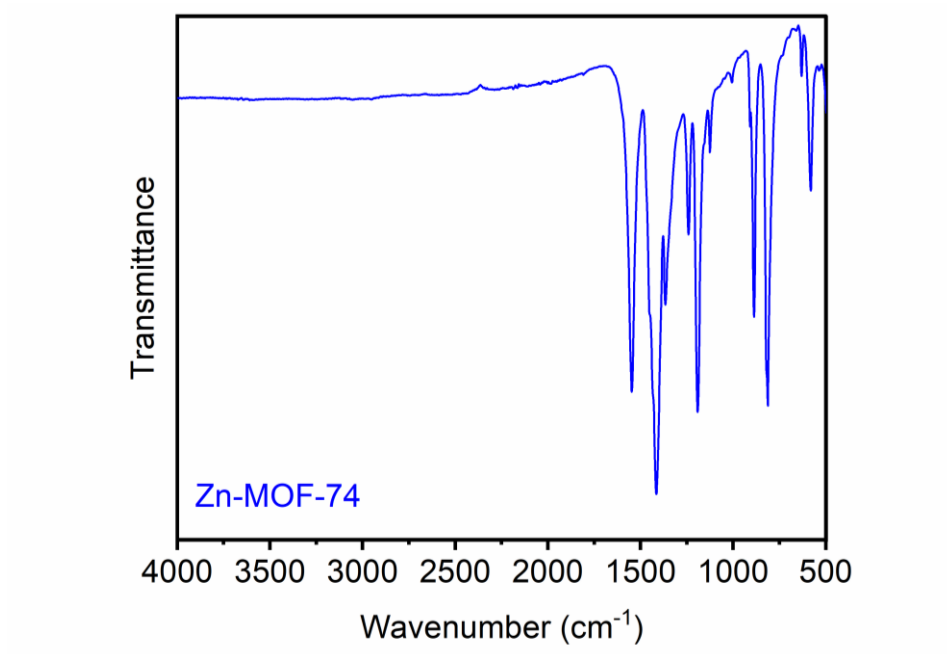


Figure S92. Infrared spectrum of Zn-MOF-74.

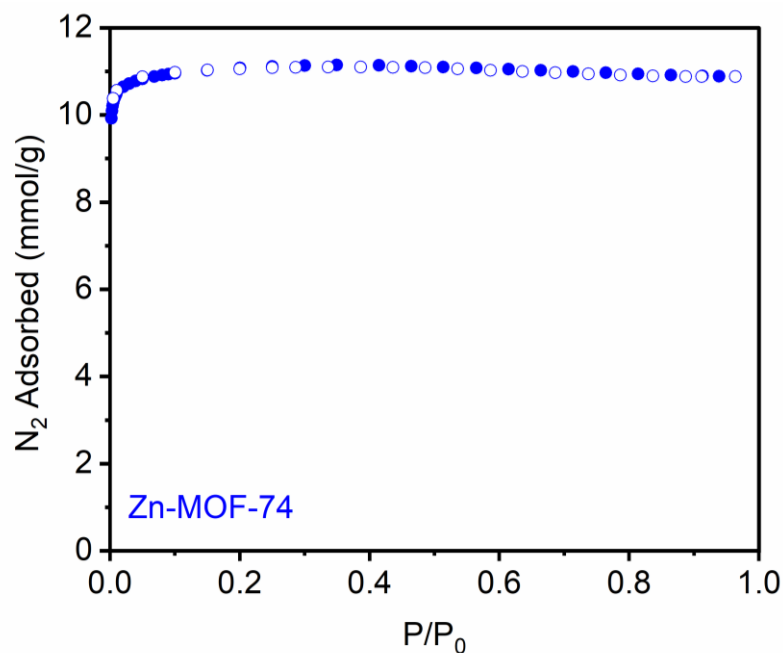


Figure S93. 77 K N_2 adsorption isotherm of activated Zn-MOF-74. Desorption data are represented as open circles. Fitting the data yielded a Brunauer-Emmett-Teller (BET) surface area of $971 \text{ m}^2/\text{g}$ (previously reported BET surface area of $1000 \text{ m}^2/\text{g}$).¹⁶

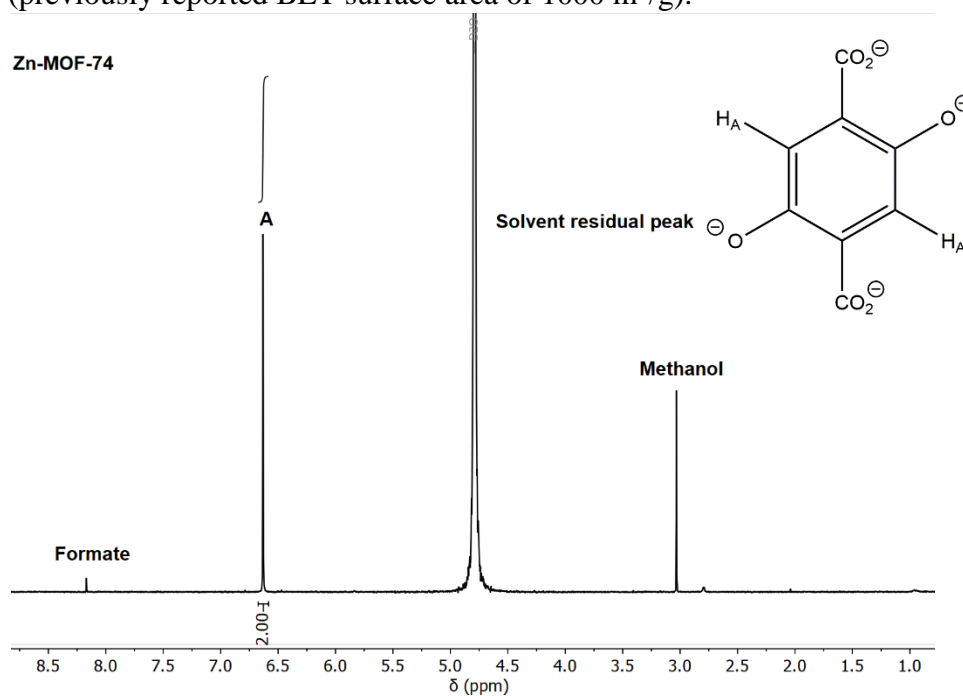


Figure S94. $^1\text{H-NMR}$ (500 MHz, D_2O) spectrum of methanol-solvated Zn-MOF-74 digested with a saturated solution of K_3PO_4 in D_2O . Peak A corresponds to the 2,5-dihydroxyterephthalate linker.

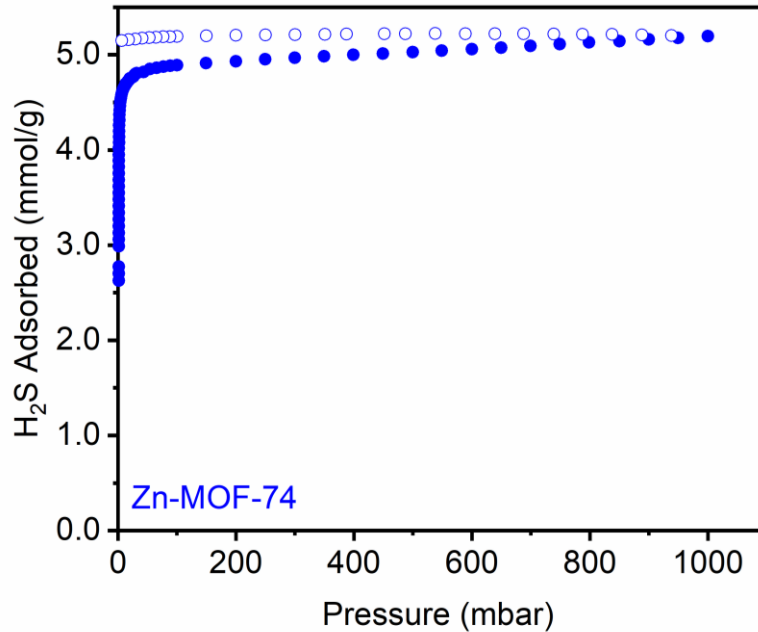


Figure S95. H₂S adsorption isotherm at 25 °C of activated Zn-MOF-74. The constant-value desorption data (open circles) suggest that H₂S binding in this framework is irreversible.

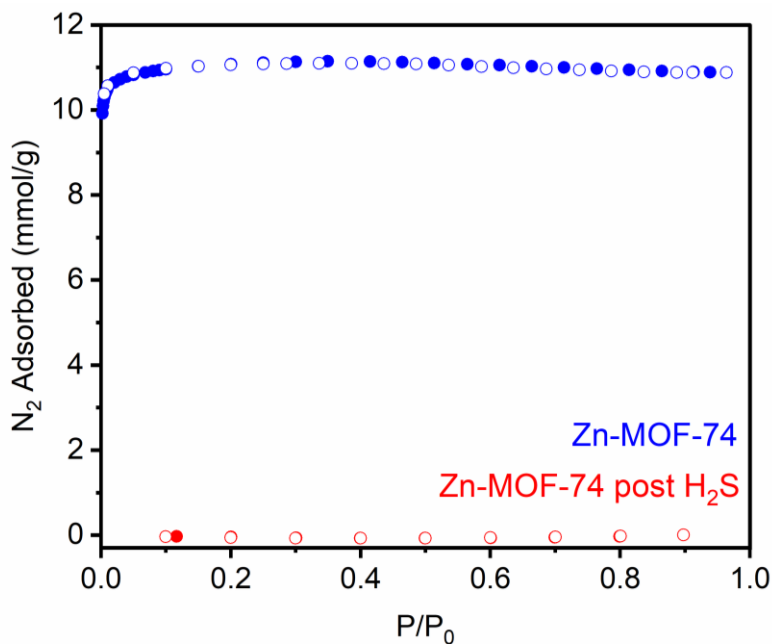


Figure S96. 77 K N₂ adsorption isotherms of Zn-MOF-74 pre- and post- H₂S adsorption isotherm at 25 °C (Figure S95). Desorption data are represented as open circles. Zn-MOF-74 was regenerated after H₂S adsorption at 180 °C for 24 h. The non-porous nature of Zn-MOF-74 after exposure to H₂S confirms that this gas binds irreversibly in the framework.

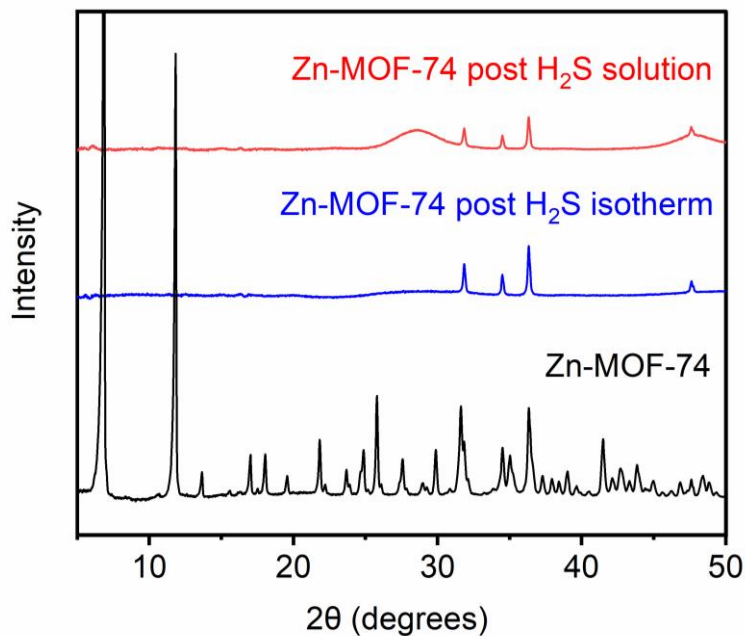


Figure S97. Powder X-ray diffraction patterns ($\lambda = 1.54 \text{ \AA}$) of Zn-MOF-74 pre- and post-exposure to gaseous H₂S (blue) and H₂S in THF (red, see Section 11 for procedure). In both cases amorphization of the framework was observed.

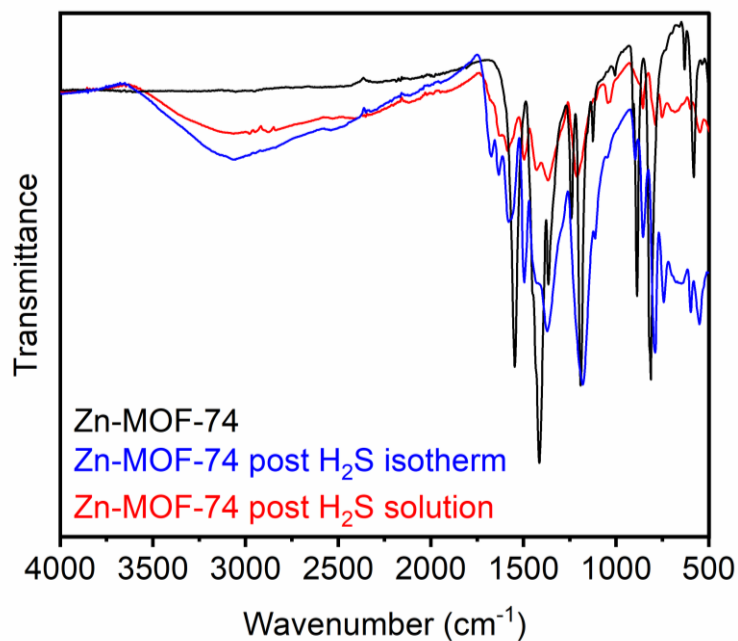


Figure S98. Infrared spectra of Zn-MOF-74 pre- and post-exposure to gaseous H₂S (blue) and H₂S in THF (red).

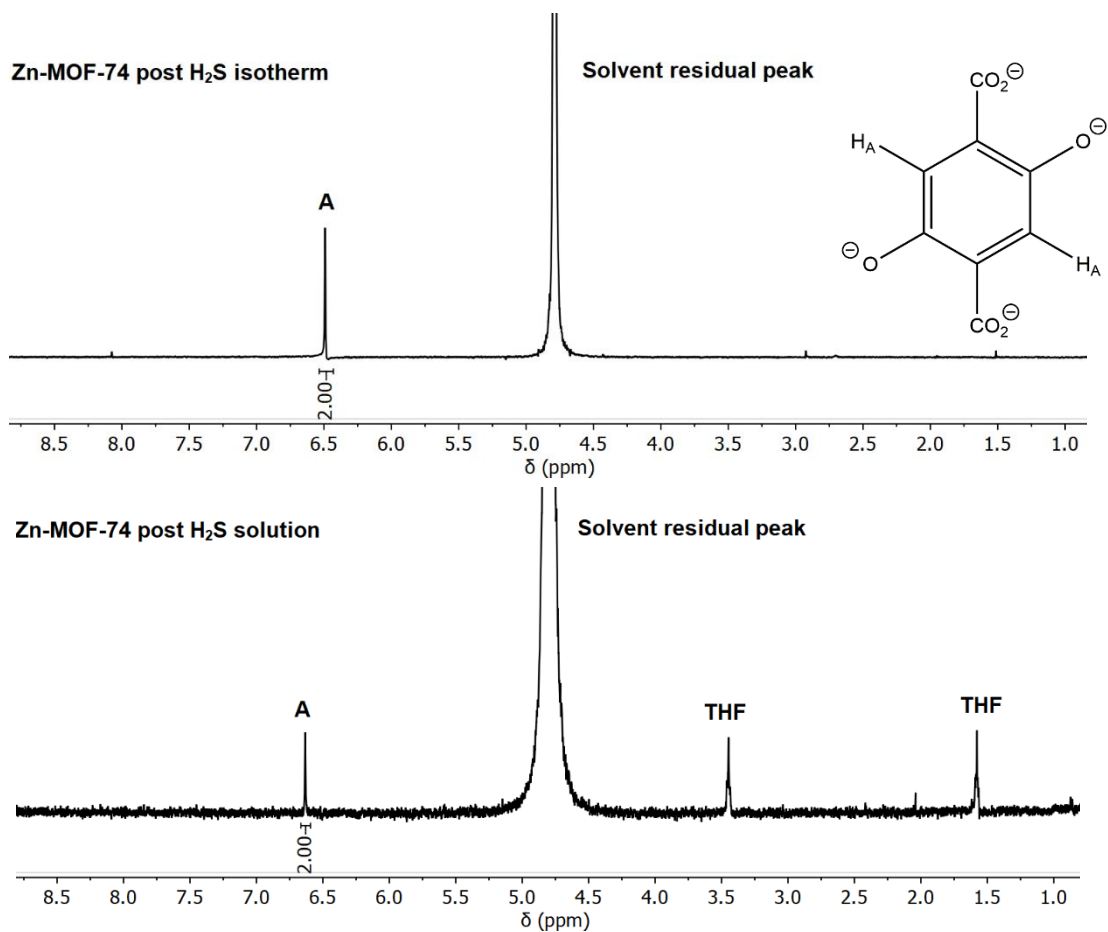


Figure S99. ¹H-NMR (500 MHz, D₂O) spectrum of Zn-MOF-74 post-exposure to gaseous H₂S (top) and H₂S in THF (bottom) digested with a saturated solution of K₃PO₄ in D₂O. Peak **A** corresponds to the 2,5-dihydroxyterephthalate linker.

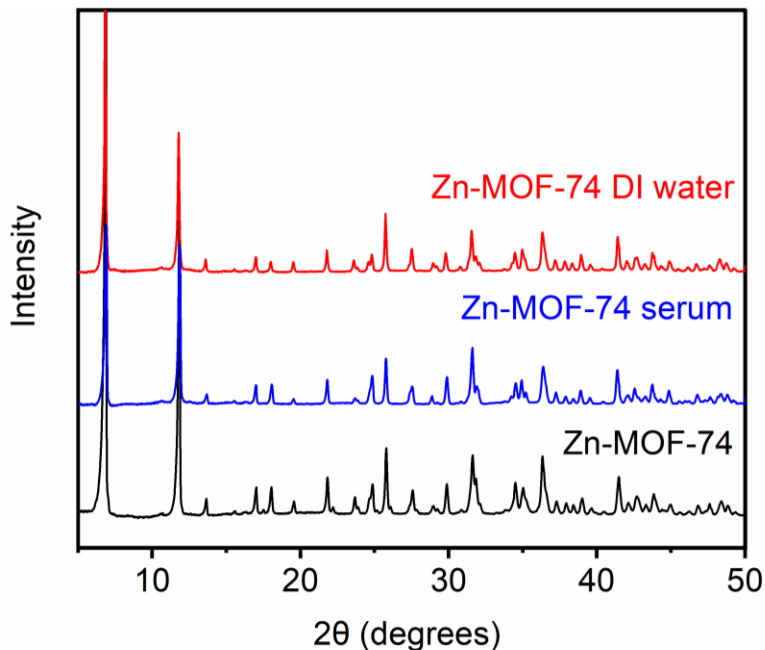


Figure S100. Powder X-ray diffraction patterns ($\lambda = 1.54 \text{ \AA}$) of Zn-MOF-74 pre- and post-exposure to DI water (red) and serum (blue, 10% FBS in DMEM) as described in Section 13. Zn-MOF-74 retained crystallinity when exposed to both DI water and serum.

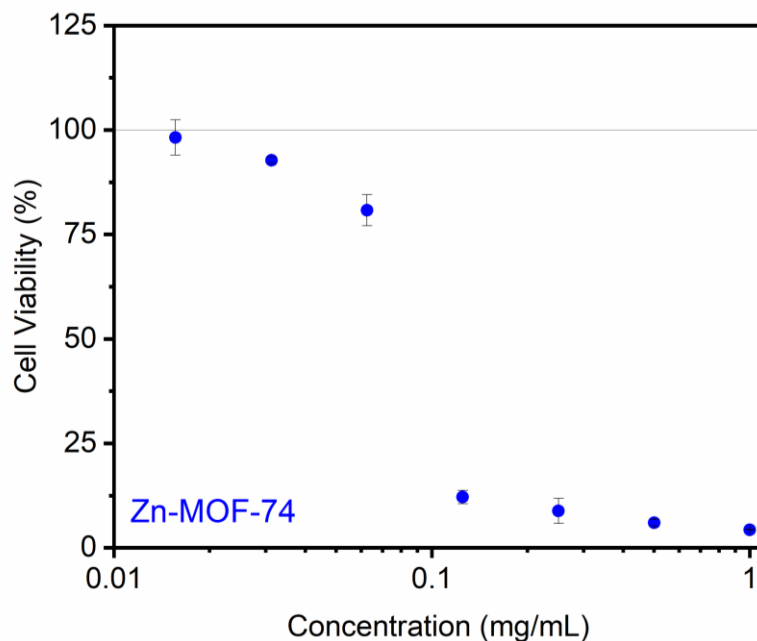


Figure S101. Viability of HeLa cells upon exposure to suspensions of activated Zn-MOF-74 at a range of concentrations in DMEM supplemented with 10% FBS for 72 h at $37 \text{ }^\circ\text{C}$. Viabilities were determined by the method described in Section 13. Unlike Zr-fum, Zr-mes, and Zr-ita, this framework is significantly more toxic at concentrations greater than 0.1 mg/mL.

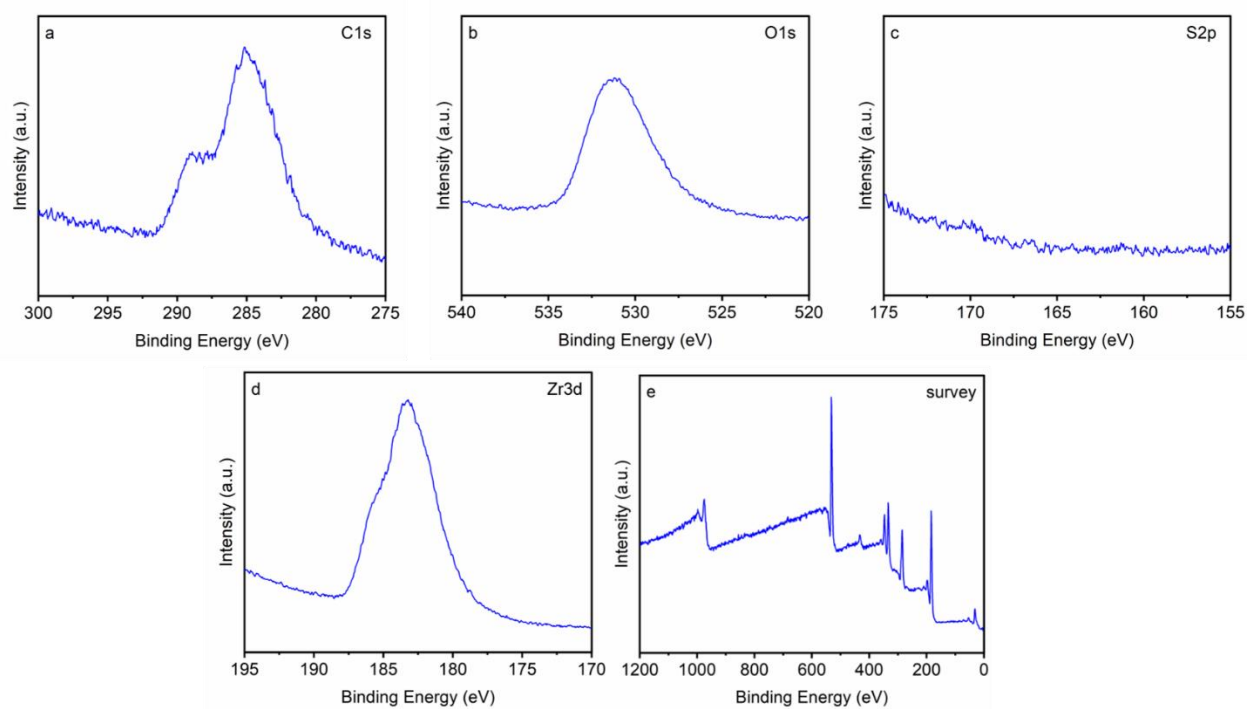


Figure S102. XPS spectral scans of (a) C1s, (b) O1s, (c) S2p, (d) Zr3d, and (e) survey of an activated sample of Zr-fum-H₂O.

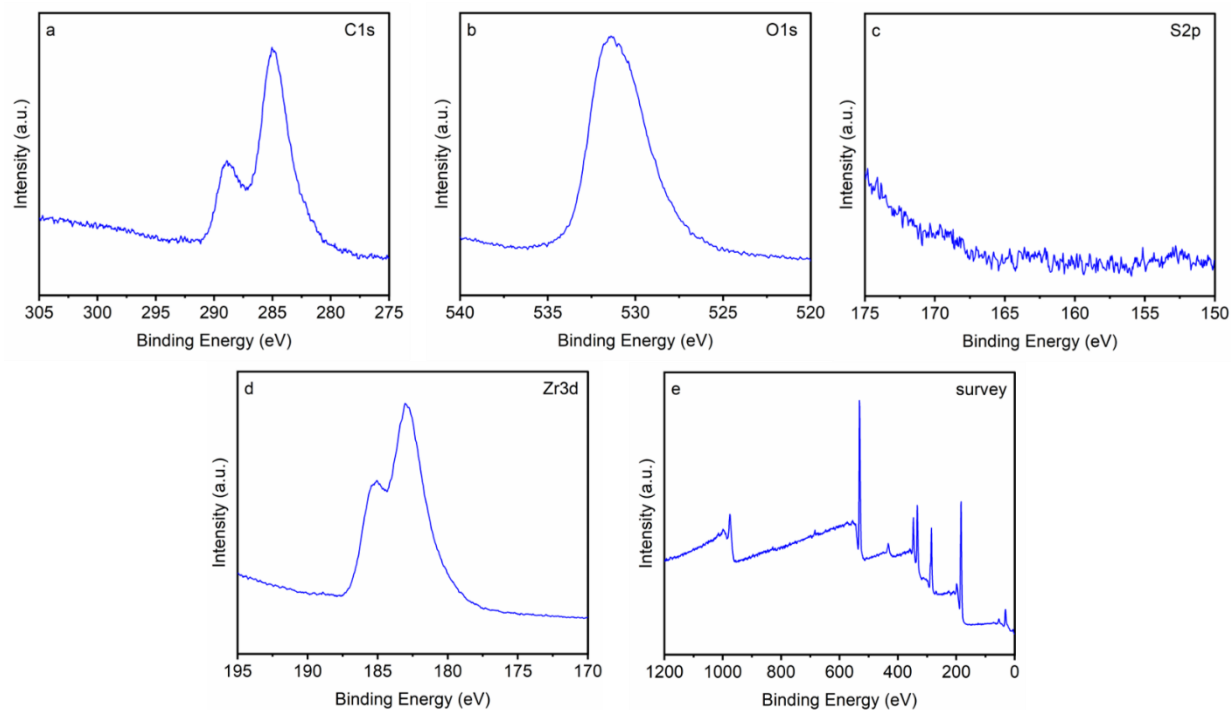


Figure S103. XPS spectral scans of (a) C1s, (b) O1s, (c) S2p, (d) Zr3d, and (e) survey of an activated sample of Zr-fum-H₂O exposed to gaseous H₂S followed by re-activation under vacuum. The absence of sulfur in the re-activated sample confirms the non-destructive reversible binding of H₂S in this framework.

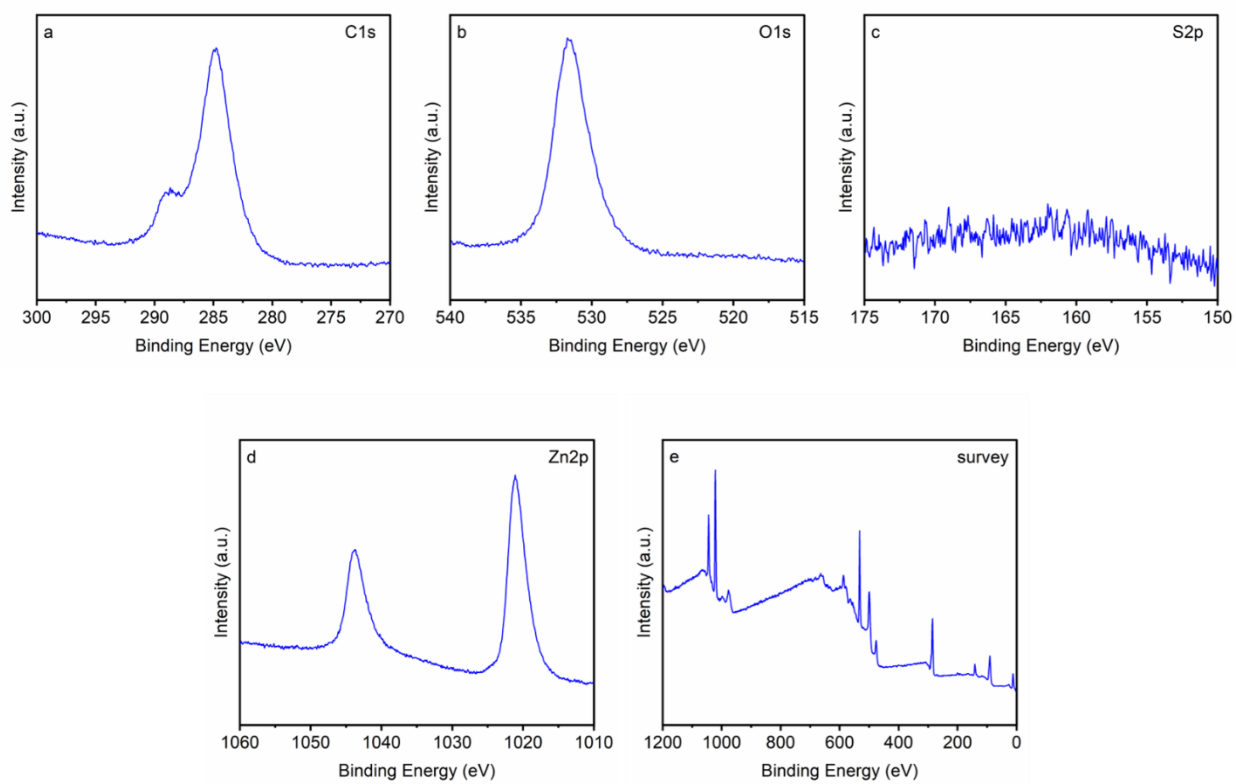


Figure S104. XPS spectral scans of (a) C1s, (b) O1s, (c) S2p, (d) Zn2p, and (e) survey of an activated sample of Zn-MOF-74.

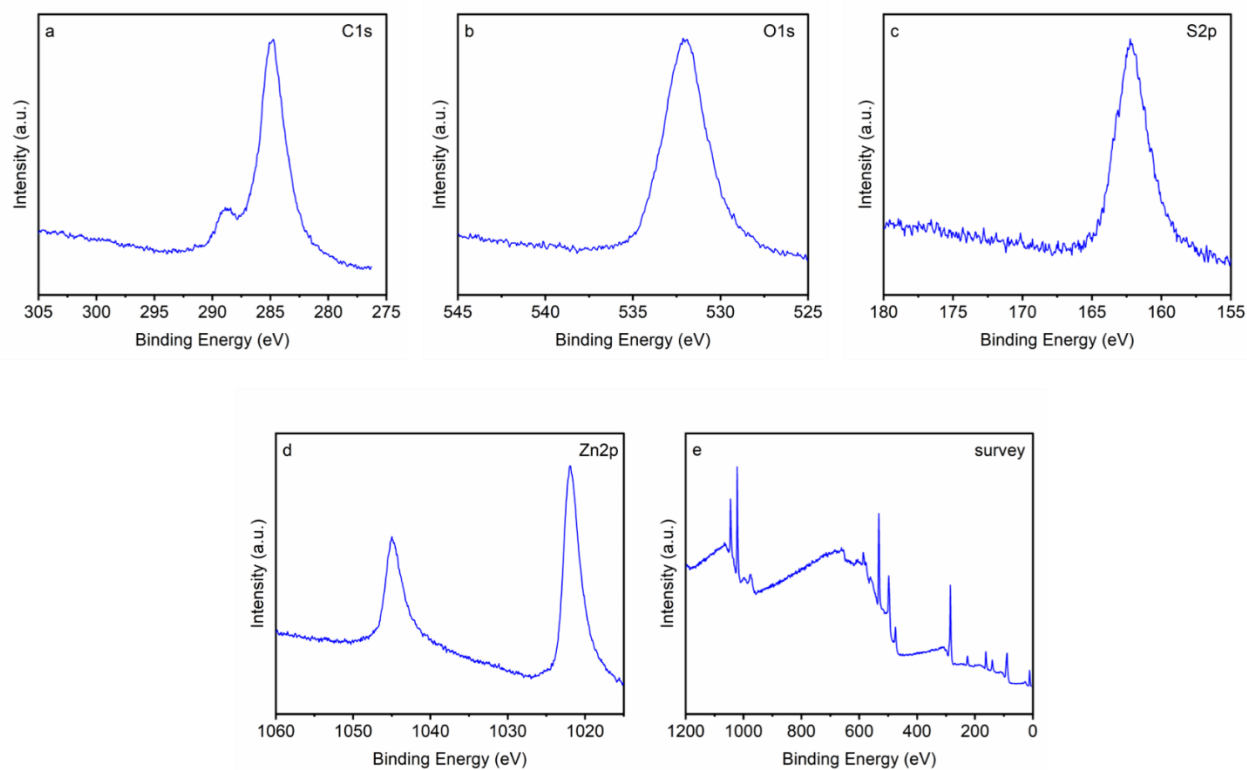


Figure S105. XPS spectral scans of (a) C1s, (b) O1s, (c) S2p, (d) Zn2p, and (e) survey of an activated sample of Zn-MOF-74 exposed to gaseous H₂S followed by re-activation under vacuum. The presence of an inorganic sulfide species as well as concomitant amorphization (Figure S97) following exposure to H₂S confirms the irreversible degradation of this framework by H₂S.

16. DRIFTS measurements.

To measure the DRIFTS spectrum of free H₂S gas, the sample cup of the Harrick low temperature reaction chamber was filled with KBr and evacuated to <10 mTorr before dosing with H₂S (400 mbar). To measure the DRIFTS spectrum of Zr-fum-H₂O and H₂S-dosed Zr-fum-H₂O, the sample cup of the Harrick low temperature reaction chamber was filled with a 1:5 mixture of Zr-fum-H₂O and KBr. The mixture was then activated at 100 °C for 18 hours using a Harrick ATK-024-3 temperature controller under high vacuum (<10 mTorr). The reaction chamber was subsequently pulsed with H₂S until desired pressures of 500, 750 and 1000 mbar were reached before immediately closing the chamber and measuring IR spectra.

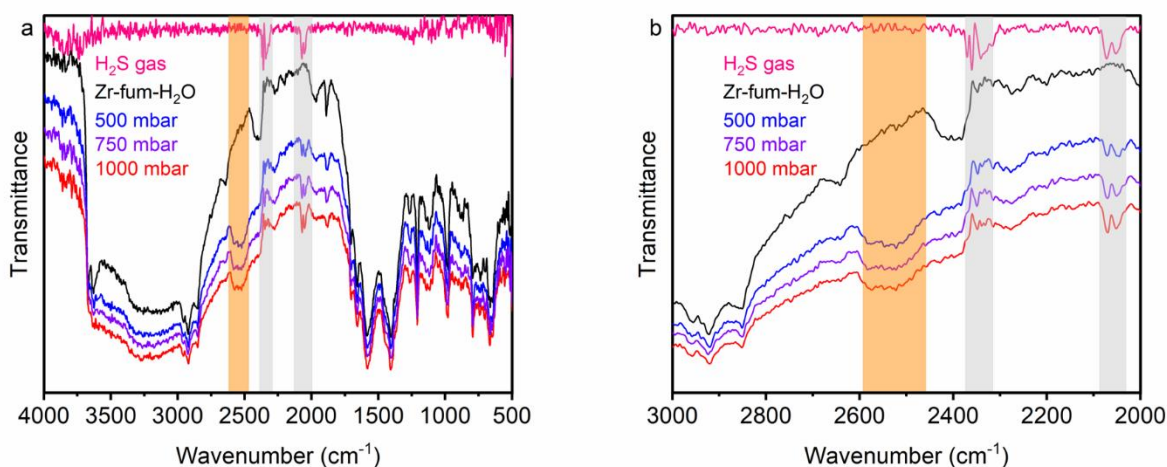


Figure S106. DRIFTS spectra of free H₂S gas (pink), activated Zr-fum-H₂O (black), and activated Zr-fum-H₂O dosed with 500 mbar of H₂S (blue), 750 mbar of H₂S (purple), and 1000 mbar of H₂S (red). Highlighted in gray boxes are the characteristic stretches of free H₂S gas between 2500 and 2000 cm⁻¹. As expected, these stretches increase in intensity with increasing pressure of H₂S. Highlighted in orange is a broad spectral feature at 2500–2600 cm⁻¹ attributed to H₂S bound inside the MOF via hydrogen-bonding interactions. (a) Full spectra and (b) 2000–3000 cm⁻¹ range.



Figure S107. DRIFTS experimental setup for dosing Zr-fum-H₂O with known pressures of H₂S gas using a Micromeritics 3-Flex gas sorption analyzer.

17. References.

- (1) Furukawa, H.; Gándara, F.; Zhang, Y.; Jiang, J.; Queen, W. L.; Hudson, M. R.; Yaghi, O. M. Water Adsorption in Porous Metal-Organic Frameworks and Related Materials. *J. Am. Chem. Soc.* **2014**, *136* (11), 4369–4381. <https://doi.org/10.1021/ja500330a>.
- (2) SK, M.; Bhowal, S.; Biswas, S. Synthesis, Characterization, Stability, and Gas Adsorption Characteristics of a Highly Stable Zirconium Mesaconate Framework Material. *EurJIC.* **2015**, *2015* (20), 3317–3322. <https://doi.org/10.1002/ejic.201500374>.
- (3) Reinsch, H.; Waitschat, S.; Chavan, S. M.; Lillerud, K. P.; Stock, N. A Facile “Green” Route for Scalable Bath Production and Continuous Synthesis of Zirconium MOFs. *EurJIC.* **2016**, *2016* (27), 4490–4498. <https://doi.org/10.1002/ejic.201600295>.
- (4) Peng, H.; Cheng, Y.; Dai, C.; King, A. L.; Predmore, B. L.; Lefer, D. J.; Wang, B. A Fluorescent Probe for Fast and Quantitative Detection of Hydrogen Sulfide in Blood. *Angew. Chem. Int. Ed.* **2011**, *50* (41), 9672–9675. <https://doi.org/10.1002/anie.201104236>.
- (5) Peng, B.; Chen, W.; Liu, C.; Rosser, E. W.; Pacheco, A.; Zhao, Y.; Aguilar, H. C.; Xian, M. Fluorescent Probes Based on Nucleophilic Substitution-Cyclization for Hydrogen Sulfide Detection and Bioimaging. *Chem. Eur. J.* **2014**, *20* (4), 1010–1016. <https://doi.org/10.1002/chem.201303757>.
- (6) Blöchl, P. E. Projector Augmented-Wave Method. *Phys. Rev. B* **1994**, *50* (24), 17953–17979. <https://doi.org/10.1103/PhysRevB.50.17953>.
- (7) Kresse, G. and Joubert, D. From Ultrasoft Pseudopotentials to the Projector Augmented-Wave Method. *Phys. Rev. B* **1999**, *59* (3), 1758–1775. <https://doi.org/10.1103/PhysRevB.59.1758>.
- (8) Kresse, G. and Hafner, J. Ab Initio Molecular Dynamics for Liquid Metals. *Phys. Rev. B* **1993**, *47* (1), 558–561. <https://doi.org/10.1103/PhysRevB.47.558>.
- (9) Kresse, G. and Furthmüller, J. Efficient Iterative Schemes for Ab Initio Total-Energy Calculations Using a Plane-Wave Basis Set. *Phys. Rev. B* **1996**, *54* (16), 11169–11186. <https://doi.org/10.1103/PhysRevB.54.11169>.
- (10) Kresse, G. and Furthmüller, J. Efficiency of Ab-Initio Total Energy Calculations for Metals and Semiconductors Using a Plane-Wave Basis Set. *Comput. Mater. Sci.* **1996**, *6* (1), 15–50. [https://doi.org/10.1016/0927-0256\(96\)00008-0](https://doi.org/10.1016/0927-0256(96)00008-0).
- (11) Kresse, G. and Hafner, J. Ab Initio Molecular-Dynamics Simulation of the Liquid-Metal-Amorphous-Semiconductor Transition in Germanium. *Phys. Rev. B* **1994**, *49* (20), 14251–14269. <https://doi.org/10.1103/PhysRevB.49.14251>.
- (12) Grimme, S.; Ehrlich, S.; Goerigk, L. Effect of the Damping Function in Dispersion Corrected Density Functional Theory. *J. Comput. Chem.* **2011**, *32* (7), 1456–1465. <https://doi.org/10.1002/jcc.21759>.
- (13) Nilsson, F.; Sakuma, R.; Aryasetiawan, F. Ab Initio Calculations of the Hubbard U for the Early Lanthanides Using the Constrained Random-Phase Approximation. *Phys. Rev. B* **2013**, *88* (12), 125123. <https://doi.org/10.1103/PhysRevB.88.125123>.
- (14) Elsässer, C.; Fähnle, M.; Chan, C. T.; Ho, K. M. Density-Functional Energies and Forces with Gaussian-Broadened Fractional Occupations. *Phys. Rev. B Condens. Matter* **1994**, *49* (19), 13975–13978. <https://doi.org/10.1103/physrevb.49.13975>.
- (15) Zick, M. E.; Lee, J.-H.; Gonzalez, M. I.; Velasquez, E. O.; Uliana, A. A.; Kim, J.; Long, J. R.; Milner, P. J. Fluoroarene Separations in Metal–Organic Frameworks with Two

- Proximal Mg^{2+} Coordination Sites. *J. Am. Chem. Soc.* **2021**, *143*, 1948–1958. <https://doi.org/10.1021/jacs.0c11530>.
- (16) Srinivas, G.; Krungleviciute, V.; Guo, Z.; Yildirim, T. Exceptional CO_2 Capture in a Hierarchically Porous Carbon with Simultaneous High Surface Area and Pore Volume. *Energy Environ. Sci.* **2014**, *7* (1), 335–342. <https://doi.org/10.1039/C3EE42918K>.